Acoustofluidic Devices in Manipulation from Cell-Level to Tissue-Level for Precision Biomedicine

Xiaoyan Zhang

A Thesis Submitted for the Degree of Doctor of Philosophy

Cardiff University

May 2025

Abstract

Acoustofluidic devices, which utilize acoustic energy to manipulate microparticles and fluids, have been widely used in biomedical studies due to their high biocompatibility (do not measurably compromise cell viability, morphology, or function). Based on the acoustic waves employed, these devices are generally divided into surface acoustic wave (SAW)-based and bulk acoustic wave (BAW)-based technologies. SAW-based devices can provide higher manipulation precision by using higher frequencies, while BAW-based devices can achieve manipulation with easier setup requirements. In this thesis, we first fabricate the Multi-View Acoustofluidic Rotation Cytometry (MARC) device for cell-level manipulation. MARC can pattern cells into two traces and rotate them *in-situ* simultaneously within the microchannel. By enabling single-cell observation from multiple angles during the rotation process, MARC exhibits better sensitivity for cell morphology differentiation. Using MARC, we identify the nuclear-to-cytoplasm (N/C) ratio as the most sensitive cytomorphological parameter during rotation, and show that rotation-based N/C analysis more clearly (i) distinguishes cancer cells from healthy cells and (ii) distinguishes different cancer cell types. We then build the Acoustic Droplets Activated Permeation (ADAP) device for tissue-level manipulation-perturb skin tissue and enhance transdermal drug delivery. By dispensing intensive droplets onto the skin surface, ADAP induces opening of the stratum corneum (SC) layer to facilitate transdermal permeation. Testing with various drug molecules shows that ADAP significantly improves delivery efficiency compared with passive diffusion. Then *in-vivo* hypoglycemic mouse models demonstrate that ADAP can achieve effective transdermal delivery of glucose solution for blood-glucose recovery in a non-invasive manner. Finally, we summarise our achievements based on the two research works and outline future directions for advancing these studies and developing improved acoustofluidic manipulation technologies.

Acknowledgement

It has been a journey of thousands of days and nights to reach the end of my PhD. During this period, I would like to thank the many people who supported me in finishing this thesis.

First and foremost, I would like to thank my PhD supervisor, Dr Xin (Chris) Yang, for his support, guidance, inspiration, and trust. Chris has not only trained me in how to do research but has also been a life-mentor, correcting and guiding me on how to solve issues, stay optimistic, and keep moving forward in life. The years under his supervision will be an invaluable fortune throughout my life.

Secondly, I would like to express my gratitude to Prof. Zhiqiang Dong and Prof. Yongqing (Richard) Fu for their support of my research projects, their guidance, and their co-supervision in completing this thesis. I also thank Prof. Aled Clayton, Dr You Zhou, and Dr Xianfang Sun for their support and help in finishing my projects. I would like to thank Dr Jin Li and Dr Hanlin Wang for their guidance, suggestions for my future career.

I would also like to thank the MUSL lab colleagues Dr Roman Mikhaylov, Dr Povilas Dumčius, Dr Mercedes Stringer, Dr Sun Chao and Ziming Zeng for their support and help. Especially, I would like to express my thanks to Roman and Povilas. Their support, inspiration, trust, and friendship have made my PhD life much easier and more colourful.

I would also like to thank my parents and my friends for their understanding, support, and encouragement throughout my PhD.

Finally, I would like to express my great gratitude to my fiancée Hang Qian. I consider myself lucky enough to have her in my life. Thank you for your unreserved input and support, and for keeping me sane at the toughest moments.

Xiaoyan Zhang

Queen’s Building,

April 2025

Contents

List of Publications

First-author research articles:

1. X. Zhang, P. Dumčius, R. Mikhaylov, et al. Surface Acoustic Wave-Enhanced Multi-View Acoustofluidic Rotation Cytometry (MARC) for Pre-Cytopathological Screening. *Advanced Science*, 2024, 11, 2403574.

2. X. Zhang, Y. Li, P. Dumčius, et al. Acoustofluidics Powered Transdermal Drug Delivery for Ultrafast Non-Invasive Disease Therapy. *(Submitted)*

Co-author publications:

3. M. Stringer, P. Dumčius, X. Zhang, et al. Multidirectionally Patterned Interdigital Transducers for Enhancing Acoustofluidic Streaming with Flexible Printed Circuit Board. *Advanced Functional Materials*, 2025, 2421308.

4. C. Sun, R. Mikhaylov, X. Yang, X. Zhang, et al. Enhanced integrated acoustofluidics with printed circuit board electrodes attached to piezoelectric film coated substrate. *Ultrasonics*, 2025, 147, 107531.

5. P. Dumčius, R. Mikhaylov, X. Zhang, et al. Dual-Wave Acoustofluidic Centrifuge for Ultrafast Concentration of Nanoparticles and Extracellular Vesicles. *Small*, 2023,19, 2300390.

6. M. Stringer, Z. Zeng, X. Zhang, et al. Methodologies, Technologies, and Strategies for Acoustic Streaming-Based Acoustofluidics. *Applied Physics Reviews*, 2023, 10, 011315.

7. H. Wang, J. Boardman, X. Zhang, et al. An Enhanced Tilted-Angle Acoustic Tweezer for Mechanical Phenotyping of Cancer Cells. *Analytica Chimica Acta*, 2023, 1255, 341120.

8. R. Mikhaylov, M. S. Martin, P. Dumcius, H. Wang, F. Wu, X. Zhang, et al. A reconfigurable and portable acoustofluidic system based on flexible printed circuit board for the manipulation of microspheres. *Journal of Micromechanics and Microengineering*, 2021, 31, 074003.

Conference participation:

1. X. Zhang. Acoustofluidic Devices in Manipulation from Cell-Level to Tissue-Level for Precision Biomedicine, Microacoustics and Microsensors Symposium 2025. Dyson Institute of Engineering and Technology, Malmesbury, UK. June, 2025. [Oral Presentation]

2. X. Zhang, Y. Li, P. Dumčius, et al. Acoustic-Enhanced Non-Invasive Transdermal Delivery for Hypoglycemia Therapy: An Alternative to Intravenous Injection. *UK Acoustofluidics SIG Meeting*. University of Cambridge, UK. November, 2024. [Poster]

3. X. Zhang. Acoustofluidic Devices for Perturbation from Cell-Level to Tissue-Level, *UK Acoustofluidics SIG Meeting*. Dyson Institute of Engineering and Technology, Malmesbury, UK. June, 2024. [Oral Presentation]

List of Figures

List of Tables

List of Abbreviations

AN	Pressure antinode
ANOVA	Analysis of the variance
ARF	Acoustic radiation force
BAW	Bulk acoustic wave
DI	Deionised
FEM	Finite element method
FITC	Fluorescein isothiocyanate
GFP	Green fluorescent protein
HE	Haematoxylin and eosin
IDT	Interdigital transducer
$LiNbO_3$	Lithium niobate
NaF	Sodium fluoride
N/C	Nuclear-to-cytoplasmic ratio
NS	Not significant
OCT	Optimal cutting temperature
PBS	Phosphate buffered saline
PCA	Principal component analysis
PCB	Printed circuit board
PDMS	Polydimethylsiloxane
PIV	Particle image velocimetry
PN	Pressure node
PZT	Lead zirconate titanate
RF	Radio frequency

ROI	Region of interest
SAW	Surface acoustic wave
SC	Stratum corneum
SSAW	Standing surface acoustic wave
TDD	Transdermal drug delivery
Vpp	Peak-to-peak voltage

Chapter 1: Manipulation in Biomedicine

1.1 Introduction

Techniques that allow precise manipulation of single particles, cells, and organisms are invaluable to advances in biology, chemistry, engineering, and physics.[1] Driven by rapid micro- and nano-manufacturing developments, a diverse array of microscale manipulation methods has emerged in recent decades.[2] Based on the underlying physical forces, these approaches are generally classified into five categories: optical, electrical, magnetic, hydrodynamic, and acoustic. Each method offers unique advantages and presents specific limitations, so the ideal choice depends on the requirements of the application.

In this chapter, we first introduce the key manipulation strategies using various physical fields, detailing their operating principles and their enabled biomedical applications at various scales. Next, we evaluate the relative strengths and weaknesses of these techniques in a comparative analysis. Finally, we highlight several representative acoustofluidic manipulation applications in biomedicine, illustrating their effectiveness at both the cell and tissue levels.

1.2 Current Manipulation Technologies

1.2.1 Optical Field Approaches

Arthur Ashkin, the father of optical tweezers, first observed in 1970 that laser radiation pressure could trap dielectric spheres.[3, 4] In 2018, the Nobel Prize in Physics was awarded to Arthur Ashkin for the invention of optical tweezers (OTs), underscoring the significance and scientific impact of this technology.[5]

Optical-field methods usually rely on a highly focused laser beam that acts as an optical trap, applying trapping forces and torques to particles of interest. The stiffness and magnitude of the forces applied by OTs vary with the laser intensity, enabling label-free manipulation of captured micron-sized dielectric particles. As shown in Fig. 1.1, intensity gradients in the converging beam draw small objects, such as a colloidal particle, toward the focus, whereas the radiation pressure of the beam tends to push them along the optical axis. When the gradient force dominates, a particle can be trapped in three dimensions near the focal point.[6]

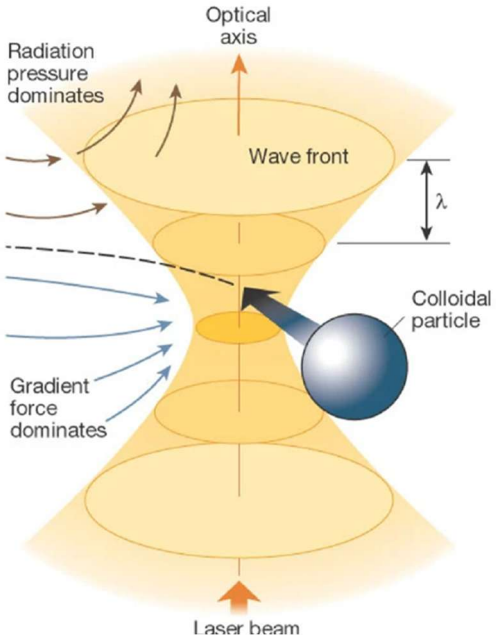

Figure 1.1. Optical field manipulation mechanism illustration.[6]

Optical fields provide the highest spatial resolution in micromanipulation, enabling nanometre-scale positioning and piconewton-scale force measurement for individual micro- and nano-objects, and are therefore widely used in biomedical studies at the molecular, subcellular, and single-cell levels. At the molecular level, optical fields have contributed significantly to understanding the structures of proteins and nucleic acids. For example, OTs have been used to drive single molecules of green fluorescent protein (GFP) into folding and unfolding intermediate states while simultaneously probing single-molecule fluorescence from each state. These experiments showed that GFP fluorescence requires complete structural integrity: none of the unfolding or refolding intermediates fluoresced, but fluorescence was recovered upon complete refolding, enabling reversible, mechanical switching of GFP between on and off states.[7] OTs have also been used to study interactions between telomerase and its substrate DNA during the translocation process. As shown in Fig. 1.2a, the connection between the two beads is formed by the association of telomerase with its substrate DNA. When a low constant force (4.0-4.5 pN) is applied to the tether, substrate elongation by telomerase is measured as an increase in the distance between the beads. Based on these measurements, the authors demonstrate that stable binding of the substrate DNA at an anchor site within telomerase enables processive synthesis of telomeric repeats, meaning that telomerase can add multiple repeat units in sequence during a single binding event without dissociating from the DNA.[8] At the

subcellular level, optical fields have been used to study membranes, stiffness, and cellular interactions. As illustrated in Fig. 1.2b, when OTs pull latex beads away from a cell, the cell actively contracts and interacts with the surrounding extracellular matrix. Using this method, it was shown that cell contractility induces large stresses that generate a substantial stiffness gradient over an extended region in 3D matrices of collagen, fibrin, and Matrigel.[9] Finally, optical fields are also applied to cell-level manipulations such as cell transportation,[10] cell rotation,[11] and cell elastic deformation.[12] As shown in Fig. 1.2c, dual-beam OTs can move two trapped particles apart to exert a stretching force on a central cell. Under constant-force stretching, the deformability of the P. falciparum infected red-blood-cell (*Pf*-S-pRBC, schizont stage) is significantly reduced compared with healthy RBC (H-RBC).[12]

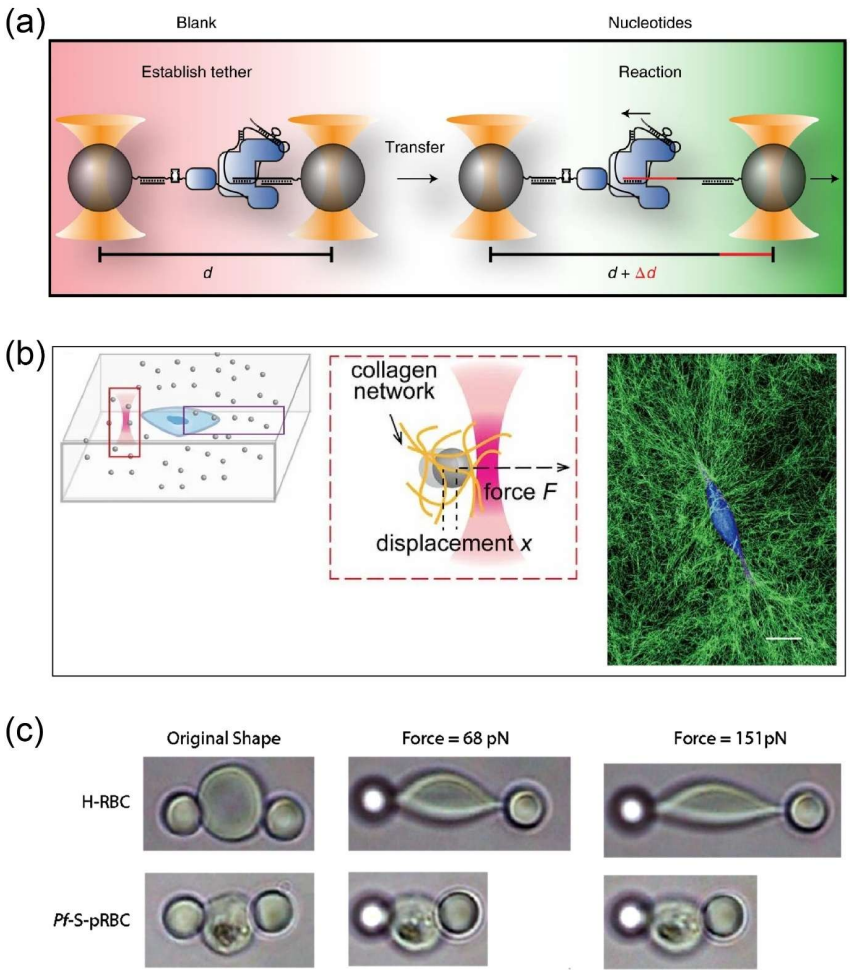

Figure 1.2. Optical fields applied in biomedical applications. (a) Molecular-level: Illustration of experimental design to measure processive telomerase catalysis.[8] (b) Subcellular-level: Schematic of force-displacement measurement between 3D extracellular matrix and MDA-MB-231 cell contraction.[9] (c) Cell-level: Optical images

of H-RBC, *Pf*-S-pRBC deformability prior and after tensile stretching by optical tweezers.[12]

1.2.2 Electrical Field Approaches

The use of the electric field in manipulation was first reported and defined by Herbert A. Pohl in 1951. He described the phenomena of particles motion induced by the non-uniform electric field and defined it as “dielectrophoresis”. And he applied this effect to remove suspended solid particles from polymer solutions.[13]

Electrical forces can be classified into electrophoresis (EP) or dielectrophoresis (DEP) depending on whether they act on a particle's fixed or induced charge, respectively. As shown in Fig. 1.3a, consider charged and neutral particles in a uniform electric field: the charged particle (left) experiences an EP force, whereas the dipole induced in the uncharged particle (right) results in no net force ($F- = F+$). EP arises from the interaction between a particle’s charge and an electric field, whereas DEP (in its simplest form) results from the interaction between a particle’s dipole and the spatial gradient of the electric field. In Fig. 1.3b, a neutral particle is placed in a nonuniform electric field; it experiences a net force toward the field maximum because the field magnitude differs at the two ends of the particle ($F- > F+$). These principles enable a variety of forces can be created to translate, rotate, stretch, or otherwise manipulate particles.[14]

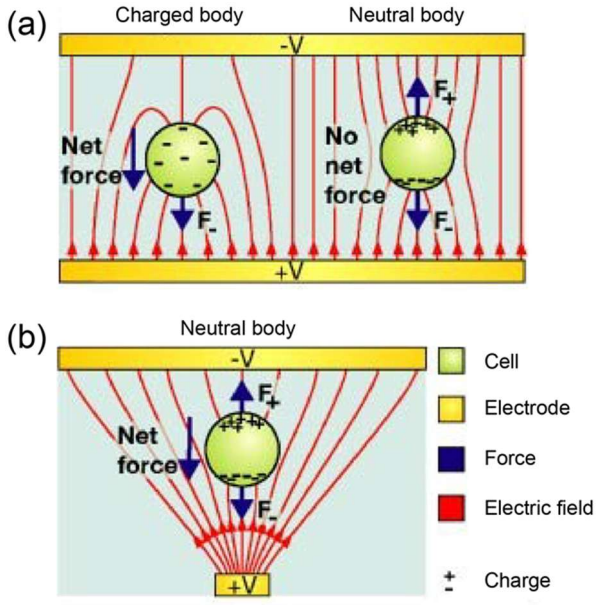

Figure 1.3. Electrical field brief working principle illustration.[14]

Due to their non-invasive manipulation capability and low setup cost, electrical fields have become a powerful tool for biomedical studies at the molecular and cell levels. At the molecular level, electrical fields have induced cell-specific drug delivery via nanowire vehicles,[15] and trapping of DNA and proteins.[16] As the illustration displays in Fig. 1.4a, a DEP nanotweezer has been developed, comprising two individually addressable nanoelectrodes separated by an ~10-20 nm insulating septum. This minimally invasive nanotweezer can be positioned at a chosen region of a living cell to extract biomolecular samples, such as DNA, mRNA, and mitochondria, with single-molecule precision. Here, “single-molecule precision” refers to the highly localised DEP field near the tweezer tip, which concentrates the strongest forces within a nanoscale volume rather than implying that surrounding molecules or cells experience no force.[16] At the cell level, electrical fields have been applied in cell trapping,[17, 18] cell rotation imaging,[19] selective separation and sorting,[20, 21] and highly controlled cell electrofusion.[22] For example, DEP can trap a P3X myeloma cell (a commonly used mouse myeloma fusion partner) together with an activated B lymphocyte (a B-cell blast) and bring them into close membrane contact. A short AC pulse can then initiate fusion, ultimately forming a heterokaryon, which is a fused cell that temporarily contains nuclei from both parent cells, after about 3 minutes (Fig. 1.4b).[22]

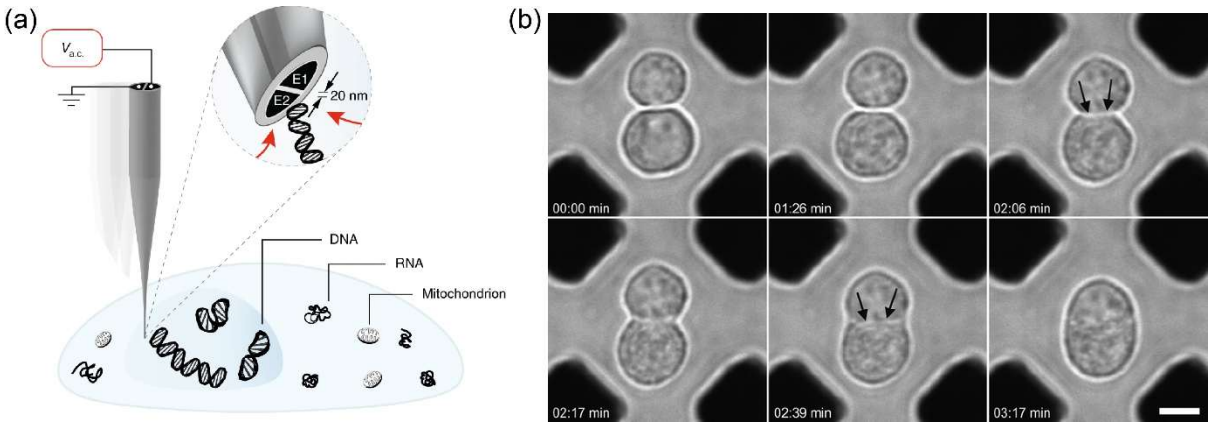

Figure 1.4. Electrical field applied in biomedicine researches. (a) Molecular-level: Schematic illustration of a DEP nanotweezer generates a highly localized electric field gradient that can trap targeted molecular inside a cell.[16] (b) Cell-level: Electrofusion of a P3X myeloma cell and a B cell blast under the DEP field cage.[22]

1.2.3 Magnetic Field Approaches

In demonstrations of magnetism, iron filings dispersed on a piece of paper held close to a magnet orient and align to reveal the distribution of magnetic field lines produced by the magnet, and they faithfully follow the magnet's movements and rotations. Following the same principles, Crick & Hughes used magnetic actuation to drag, twist, and prod magnetic particles within the cytoplasm of cells, providing the first demonstration of magnetic tweezers.[23]

Basic magnetic tweezers comprise a pair of permanent magnets positioned above the sample holder of an inverted microscope equipped with a charge-coupled device (CCD) camera connected to a frame grabber. Fig. 1.5 depicts the magnetic-field implementation used to investigate molecular unwinding mechanisms and rotational friction. A molecule is tethered between the surface of a flow cell and a paramagnetic bead. The applied magnetic field induces a magnetic moment in the bead, which experiences a force proportional to the field gradient. Rotating the external magnets causes the bead to rotate, thereby inducing coiling (twist) in the molecule. [24, 25]

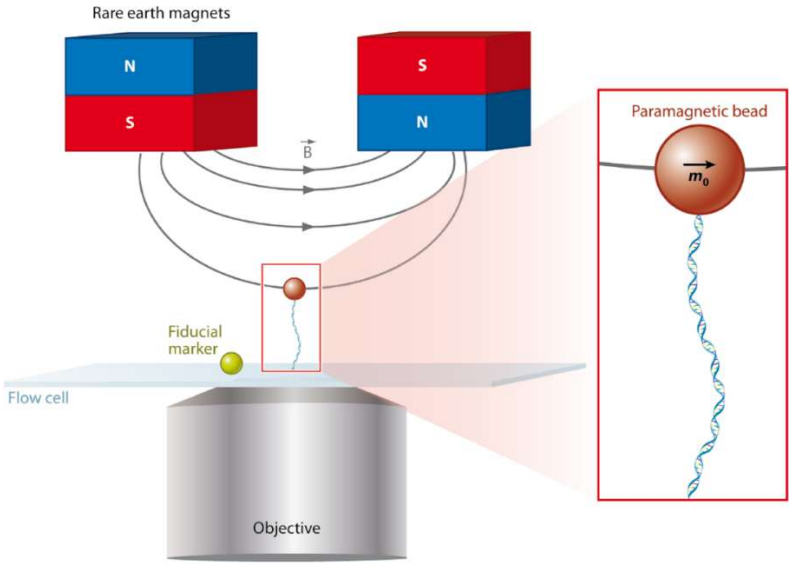

Figure 1.5. Magnetic field brief working principle illustration.[24]

Because biological tissue is nearly "transparent" to magnetic energy and fields (i.e., magnetic fields pass through tissue without being significantly absorbed or distorted), magnetic fields offer key advantages: large force output, high precision, and deep-tissue penetration. [26, 27] Building on these advantages, magnetic fields have seen substantial advances in molecular-level and cell-level applications. At the molecular

level, magnetic fields used to probe DNA topology and the activity of topoisomerases (enzymes that temporarily cut and rejoin DNA to relieve supercoiling),[28] measurement and deduction of effective torsional modulus of DNA,[29] protein folding mechanics and kinetics study.[30, 31] As an example illustration in Fig. 1.6a, a five-helix bundle protein (wildtype λ_{6-85}, refer as λ_{wt}) was reconstructed so that it can be pulled by magnetic forces at low loads. At a given force, hundreds of folding and unfolding events of λ_{wt} were observed over hundreds of seconds. Increasing the force inverted the populations from a predominantly folded state (low extension) to a predominantly unfolded state (high extension).[31] At the cell level, magnetic fields have been applied to cell transportation,[32] cell mechanics measurement,[33] and to study crosstalk between cell-death signalling pathways, where shared regulators and feedback loops can shift cells between apoptosis, necroptosis, and other death programmes depending on context.[34] As shown in Fig. 1.6b, after applying a 10 nN force to a mouse embryonic fibroblast cell (using magnetic microbeads coupled via integrin-type adhesion receptors to the cytoskeleton), the cell did not fully recover its original shape even after a waiting time of 5 s-more than 50 times the 0.1 s force-application duration.[33]

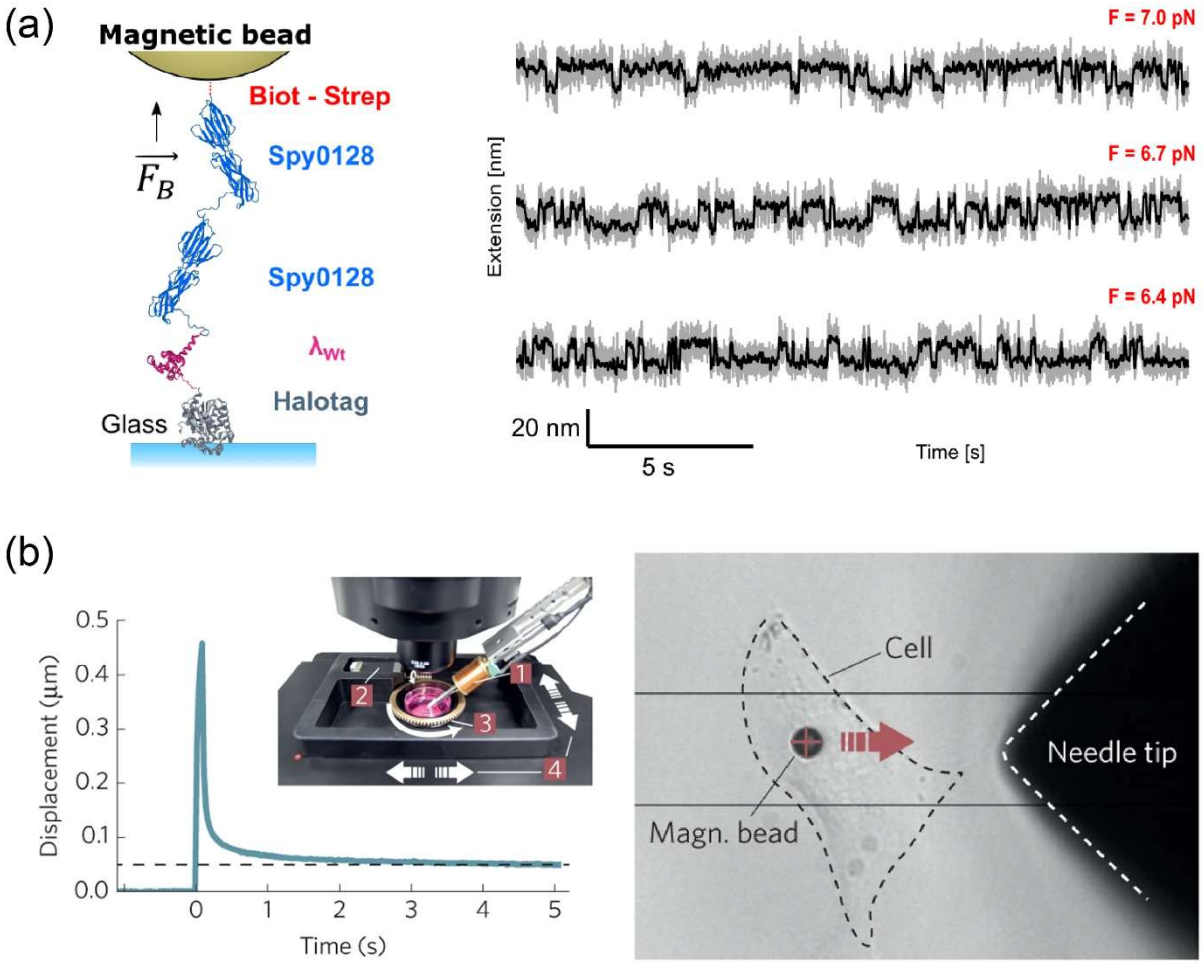

Figure 1.6. Magnetic fields applied in biomedicine researches. (a) Molecular-level: Schematics of the recombinant protein construct in the magnetic tweezers setup (left), and zoom-in to the extension over a time-lapse of 20 s for three different forces (right) showing unfolding and refolding of λ_{wt}.[31] (b) Cell-level: NIH3T3 mouse embryonic fibroblasts cell shape recovery measurement through stretching a magnetic particle attached to cell surface for 0.1 s and relaxation 5 s.[33]

1.2.4 Hydrodynamic Field Approaches

Hydrodynamic field approaches use controlled flow (e.g., laminar shear, pressure-driven transport, and sheath-flow focusing) to position and move cells/bioparticles in a predictable manner, typically without labels and with minimal perturbation. As a familiar example, in many flow cytometers (including FACS instruments), hydrodynamics is primarily used in the fluidics module to achieve sheath-flow hydrodynamic focusing, aligning cells into a narrow, near single-file stream for consistent interrogation; the measurement and sorting functions are handled by the optical, electronic, and actuation subsystems rather than by hydrodynamics itself.[35, 36]

Hydrodynamic technologies rely on the intrinsic properties of fluids (hydrodynamic effects) to manipulate bioparticles and do not require external fields for driving forces. Here we separate the mechanism in two scenarios: adherent and suspended bioparticles subjected to fluid flows that have two corresponding hydrodynamic effects (Fig. 1.7). When fluid flows in microfluidic channels at the velocity (U), the velocity profile inside a circular channel or pipe is referred to as being “parabolic”, with a maximum velocity occurring at the channel centreline. In this case, the wall shear rate generates shear stress that acts on wall-adherent bioparticles, and the wall strain rate can be controlled by the microchannel height and width (Fig. 1.7a). For suspended bioparticles in a straight microchannel, motion is governed predominantly by shear-gradient lift forces that drive the particle toward the walls, and wall-induced forces that drive it away from the walls toward the channel centre. The interplay between these forces yields a steady-state equilibrium position, and the locations of stable equilibria depend on the channel cross-sectional shape. In a curved microchannel, because of the curvature in the channel, centrifugal forces acting on fluid elements create a radial pressure gradient that drives the fluid radially, triggering a secondary recirculating flow across the channel cross section that consists of two symmetric vortices and is referred to as a Dean flow. Because larger particles experience stronger Dean drag, they tend to focus near the inner wall, whereas smaller particles focus near the outer wall (Fig. 1.7b).[37]

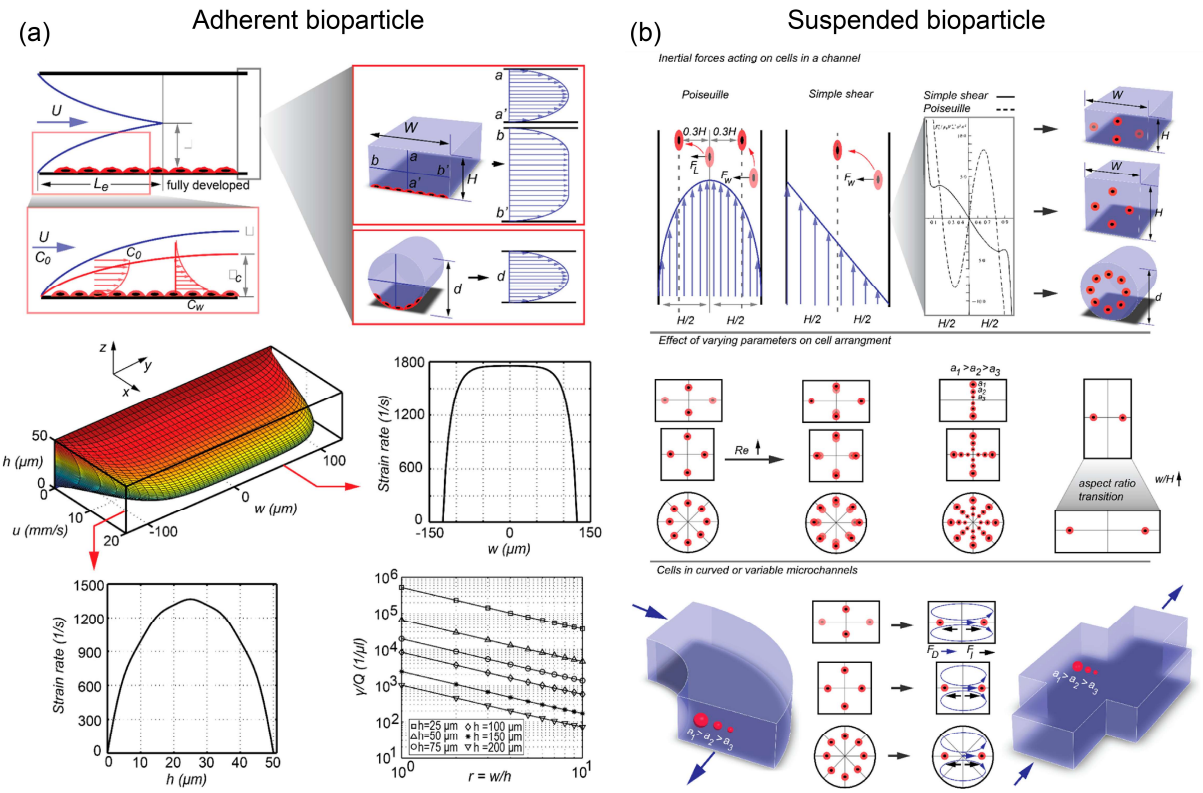

Figure 1.7. Hydrodynamic field short working principle illustration.[37] (a) For adherent bioparticle. (b) For suspended bioparticle.

Hydrodynamic fields are label-free and can be non-perturbative for bioparticles, meaning they can manipulate samples without significantly altering their native state, and they have therefore been widely applied in studies at the molecular and cell levels. At the molecular level, hydrodynamic fields have been used for DNA focusing and separation,[38, 39] and for the separation of bacterial artificial chromosome DNA.[40] As shown in Fig. 1.8a, the design of the hydrophoretic device consists of regularly patterned obstacles that serve as a molecular sieve. A large molecule (Micrococcus DNA, 115 kb, meaning ~115,000 base pairs) with a radius of gyration (R_g, a measure of how spread out the coiled molecule is in solution) that is greater than the obstacle gap (H_g) does not immediately pass through the gap but migrates toward the left sidewall, whereas a smaller molecule (λ-phage DNA, 49 kb) with R_g < $H_g$follows the hydrophoretic ordering and is separated from the large molecule. At the cell level, hydrodynamic methods have been applied to cell stimulation,[41, 42] selective cell sorting,[43] cell trapping,[44, 45] and cell mechanical phenotyping.[46, 47] Using inertial focusing to uniformly deliver cells to a stretching extensional flow where cells are deformed at high strain rates, high-throughput cell biophysical information including

initial diameter and deformability can be acquired and analysed (Fig. 1.8b). Based on this approach, researchers rapidly assayed the deformability of native leukocytes and malignant cells in pleural effusions and accurately predicted disease state in patients with cancer and immune activation, with a sensitivity of 91% and a specificity of 86%.[46]

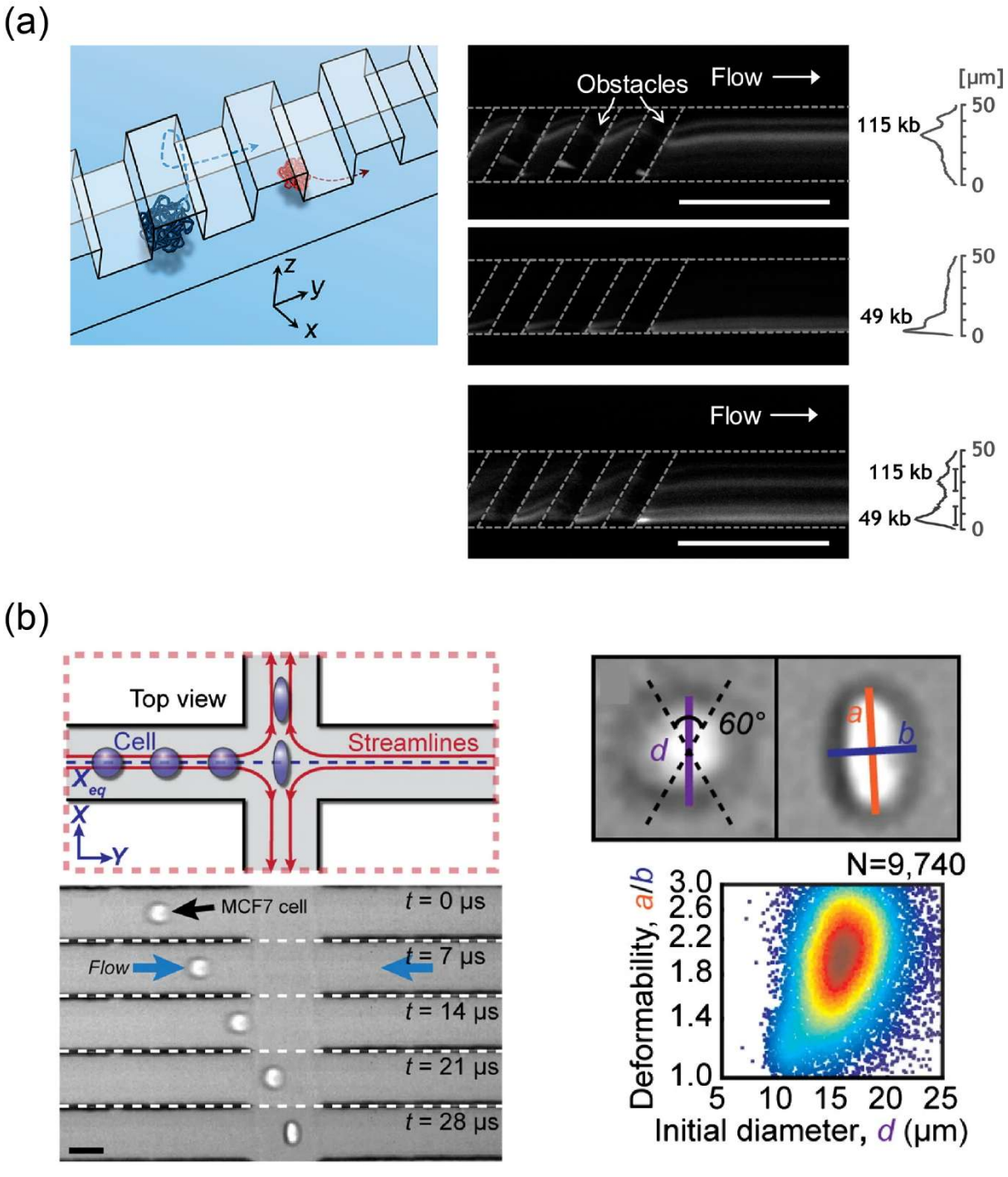

Figure 1.8. Hydrodynamic field applied in biomedicine researches. (a) Molecular-level: Differential molecular ordering of Micrococcus DNA and λ-phage DNA.[39] (b) Cell-level: Deformability cytometry for MCF-7 population biophysical measurements.[46]

1.2.5 Acoustic Field Approaches

The term “acoustic tweezers” was first used in 1991, when Junru Wu reported that acoustic potential well can trap the latex particles and frog eggs clusters and can move them axially.[48]

Acoustic-field approaches usually rely on two main nonlinear acoustic effects that induce the momentum change of the microparticles or their environments: acoustic radiation force and acoustic streaming. The acoustic radiation force (ARF) is a time-averaged force that acts at interfaces between media with different acoustic properties, arising from scattering and absorption of acoustic energy. When manipulating microparticles whose radius (a) is considerably smaller than the acoustic wavelength (λ) in the fluid, it is named Rayleigh particle ($a \ll \lambda$). In this regime, the Gor’kov potential derived an expression to calculate the gradient ARF on a Rayleigh particle. The second effect-acoustic streaming, is another nonlinear acoustic effect that converts acoustic energy into steady flows in the surrounding fluid. As shown in Fig. 1.9a, two pairs of acoustic-wave generators form a three-dimensional (3D) acoustic field. By controlling the interplay between the acoustic radiation force and the Stokes drag force induced by acoustic streaming, microparticles can be manipulated along the x, y, and z axis (Fig. 1.9b).[49] Here we provide only a brief introduction to acoustic fields, a detailed description is given in Chapter 2.

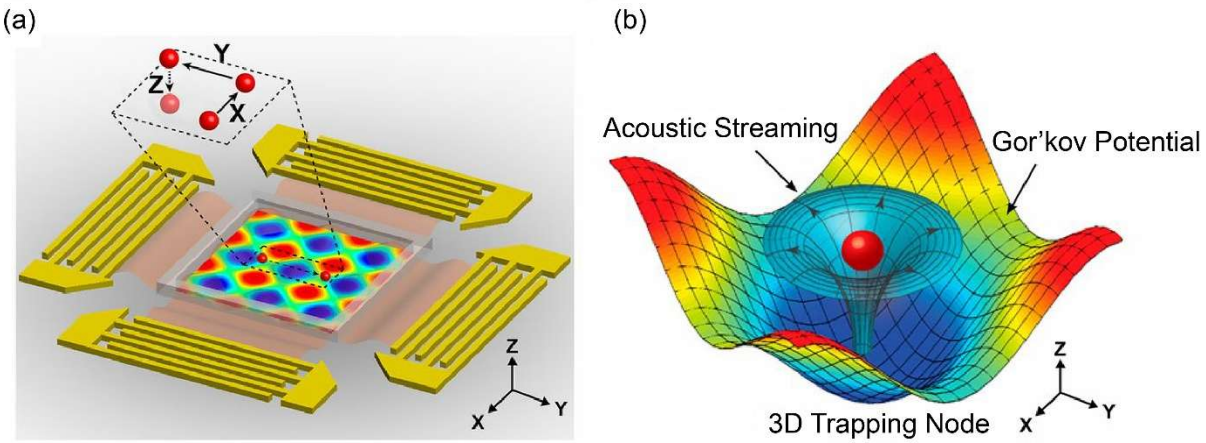

Figure 1.9. Acoustic field brief working principle illustration.[49] (a) Schematic of a three-dimensional (3D) acoustic manipulation. (b) Main acoustic forces that bioparticle experienced in the 3D trapping node.

Acoustic fields offer label-free manipulation and excellent biocompatibility. In recent years, acoustic micromanipulation has attracted growing research interest and has

been applied at the molecular, subcellular, single-cell, and tissue levels studies. At the molecular level, acoustic fields have been used for force spectroscopy of DNA-protein interaction,[50] and for accelerating enzymatic catalysis.[51, 52] As shown in Fig. 1.10a, an acoustofluidic platform featuring acoustic virtual stirrer (AVS) arrays uses an oscillating acoustic-node lattice to generate dynamic radiation forces and Eckart streaming, creating turbulence-like mixing for efficient in situ mixing and mass exchange. the AVS platform demonstrates effective enhancement of enzyme–nucleic acid reactions, including polymerization by DNA polymerase I and ligation by T4 DNA ligase.[52] At the subcellular level, acoustic fields have been extensively used for biomarker enrichment especially for exosome concentration.[53, 54] A dual wave acoustic device enables ultrafast concentration of extracellular vesicles (EVs) is presented in Fig. 1.10b. By setting a 120° angle between the interdigital electrodes and the reference flat of the piezoelectric substrate, the device simultaneously generates Rayleigh and shear-horizontal waves, resulting in effective EV concentration in droplets while preserving EV integrity under cryo-electron microscopy.[54] At the cell level, acoustic methods are widely used for cell separation and sorting,[55, 56] cell stimulation,[57] and cell lysis.[58, 59] As shown in Fig. 1.10c, a surface acoustic wave (SAW) based cell stimulation device has been built for cell differentiation stimulation. The generation of SAW coupling into the cell medium form leaky SAWs and induce surface vibration on the $LiNbO_3$ substrate. Together these effects act on human embryonic stem cells (hESCs), producing a significant acceleration in neural differentiation.[57] At the tissue level, acoustic tweezers support the construction of complex, functional tissue via bioprinting or bioassembly,[60, 61, 62] assist targeted drug delivery,[63, 64] and trigger tissue reprogramming or maturation.[61, 65, 66] One study reported that ultrasound standing waves can organize myoblast populations within material systems to engineer aligned muscle tissue constructs. Patterned muscle engineered using type I collagen hydrogels exhibits significant tensile anisotropy and, under mechanical constraint, produces microscale alignment at both the cell and fibre levels (Fig. 1.10d).[61]

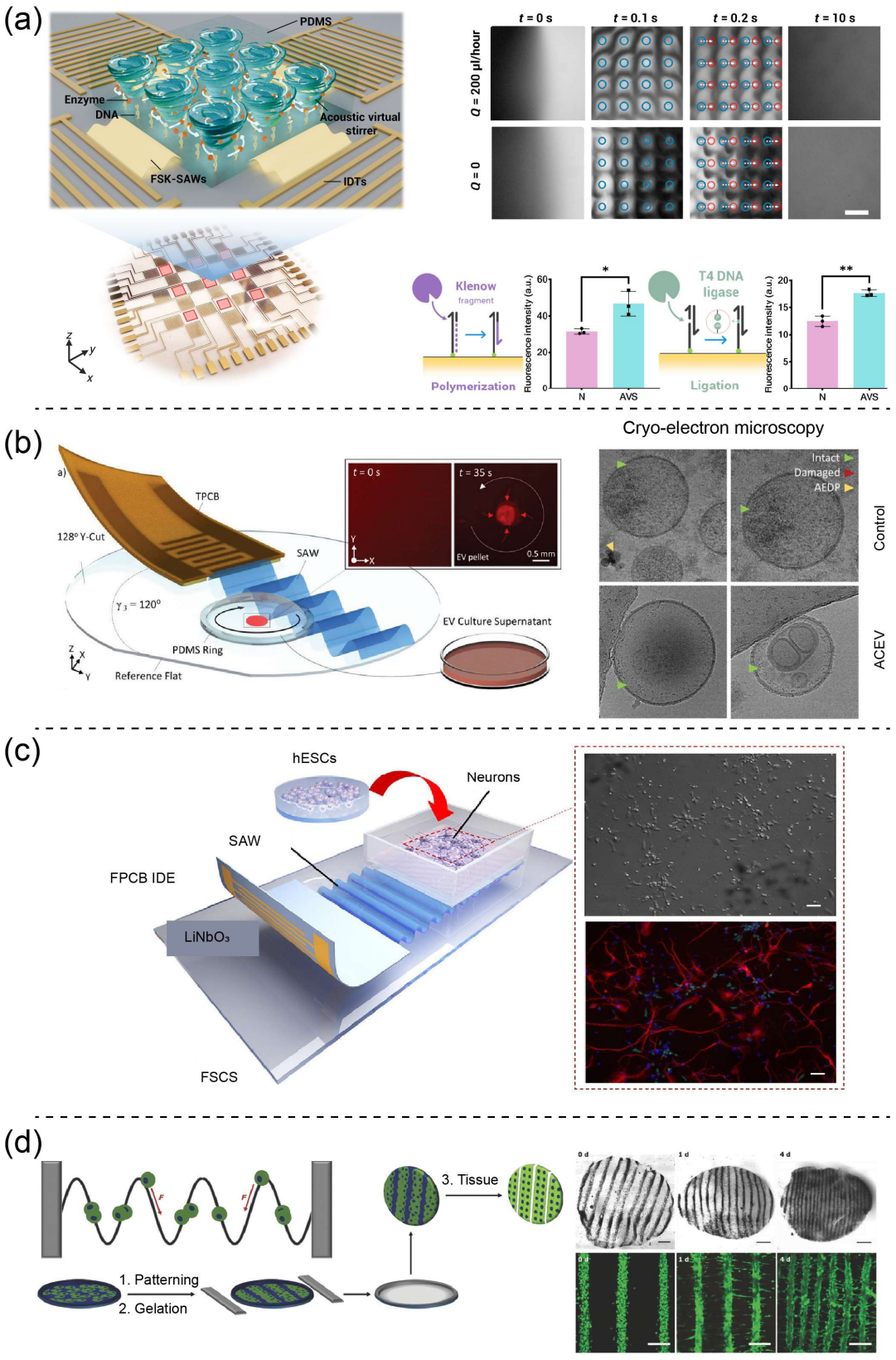

Figure 1.10. Acoustic field applied in biomedicine researches. (a) Molecular-level: Stirring to increase the efficiency of interfacial enzymatic nucleic acid reactions.[52] (b) Sub-cellular level: Ultrafast extracellular vesicle concentration.[54] (c) Cell-level: Human

embryonic stem cells acceleration differentiation to neurons.[57] (d) Tissue-level: Patterning myoblast populations forms engineering of aligned muscle tissue constructs.[61]

1.3 Summary of the Manipulation Approaches

As shown above, a range of physical-field modalities have been developed for microscale manipulation, each offering distinct advantages depending on the sample type and experimental goal. To support an objective comparison, Table 1.1 summarises representative manipulation performance and concise strengths/limitations across these methods. Optical tweezers provide the highest spatial resolution and precise single-object control; however, the high optical intensities required to form stable traps can potentially damage fragile biosamples.[67] Electrical-field approaches enable versatile on-chip actuation and can be highly programmable, but local application is challenging, requiring either closely spaced invasive electrodes or surface electrodes that may non-specifically stimulate cultured biosamples.[68] In addition, electric fields cannot provide mechanical stimuli during cell or tissue development.[69] Magnetic fields can penetrate deep tissue and generate high forces, yet most cells are not inherently responsive, often necessitating additives such as magnetic nanoparticles to transmit magnetic forces for assembly or mechanical stimulation.[70, 71] Such magnetic labelling methods may be cytotoxic and cause cell death.[72] Hydrodynamic methods are among the simplest and can be highly scalable; however, their controllability is limited and their ability to manipulate nanoparticles is typically of only modest precision.[73] Acoustic approaches provide a complementary contact-free route by coupling acoustic waves to fluids to generate acoustic radiation forces and acoustic streaming, enabling manipulation of particles and fluid flows using engineered pressure fields, often at power levels comparable to ultrasound imaging. Practical performance is device- and sample-dependent (e.g., resonance/geometry/medium), and achieving nanometre-scale precision remains challenging relative to optical trapping. Overall, there is a clear trend toward manipulation platforms that combine high flexibility, high precision, high repeatability, and contactless/biocompatible operation, while remaining practical and convenient for routine use.

Table 1.1. Summary of different particle manipulation technologies.

Technique	Size range	Input power	Spatial resolution	Strengths	Limitations
Optical	100 nm-1 mm	10^6-10^7 W/cm^2	0.1-1 nm	Ultra-fine positioning and strong single-target control	Risk of photo-heating/phototoxicity; complex setup
Electrical	1 nm-1 mm	10^4-10^7 V/m	0.1-1 μm	Highly tuneable actuation on-chip; good programmability	Electrode dependence; possible unintended cell stimulation; limited mechanical stimuli
Magnetic	1-10 μm	1-10 tesla	1-10 nm	Remote forcing with deep penetration; large achievable forces	Often requires magnetic tags/particles; potential bio-toxicity
Hydrodynamic	100 nm-1 mm	N/A	1-10 μm	Simple infrastructure; high-throughput handling/focusing	Geometry/flow constrained; weak “hold-and-place” control at nanoscale

Acoustic	100 nm-10 mm	10^{-2}-10 W/cm	1-10 μm	Contact-free actuation; typically label-free; can drive both particle motion and flow	Needs careful acoustic tuning (resonance/medium); nanoscale precision generally difficult

1.4 Representative Acoustofluidic Manipulation Applications at the Cell and Tissue Levels

Having briefly introduced the history and mechanisms of acoustofluidics and highlighted its superior advantages for biomedical manipulation, this section we present several representative studies in which acoustofluidic technologies have enabled critical advances at the cell and tissue levels.

1.4.1 Cell-Level Application

2D Patterning:

Arranging cells and microparticles into desired patterns is of great interest for biomedical applications such as single-cell analysis, cell-cell interaction studies, and micro-arrays.[74, 75] Based on the patterned shapes, acoustofluidic-enbled 2D cell patterning can typically be classified as: regular shape pattern (e.g., lines,[74] dot arrays.[76, 77]) and irregular shape patterns (e.g., letters,[78, 79, 80, 81] and arbitrary images.[82, 83]).

As shown in Figs. 1.11a-b, devices for regular patterns typically use a pair of interdigital transducers (IDTs) deposited on a piezoelectric substrate in either a parallel or an orthogonal arrangement. Generating two identical SAWs that propagate either in opposite (Fig. 1.11a) or orthogonal (Fig. 1.11b) directions produces standing SAWs (SSAWs) and, in turn, a periodic distribution of pressure nodes (minimum pressure amplitude) and antinodes (maximum pressure amplitude) on the substrate, which drives particles to the nodes or antinodes.[77] By further employing two pairs of orthogonally patterned IDTs at higher frequency (i.e., the acoustic wavelength is comparable to the microparticle size), single particles or cells can be arranged into dot

arrays.[76] For irregular pattern, an additional acoustic layer (e.g. lenses, holograms, and metasurfaces) is usually placed above the transducer to reshape the acoustic field for more precise patterning. As shown in Fig. 1.11c, Melde and colleagues used a single transducer coupled to a monolithic hologram element; only one electrical signal is required because the local thickness of the hologram element controls the pressure-field shape. In this way, they reconstructed diffraction-limited acoustic pressure fields and arbitrary ultrasound beams, patterning microparticles into a pigeon-shaped image in water and propelling objects to surf on the water surface.[83] More recently, an ultrathin metasurface approach using planarized micropillars in a discretized phase array has been demonstrated. Compared with prior acoustic holography, this metasurface enables ultrathin, planar holographic kinoforms without multilevel 3D fabrication, extending the potential of acoustic holograms—especially for high-frequency, small-wavelength micromanipulation—and achieving letter patterns with higher precision.[79]

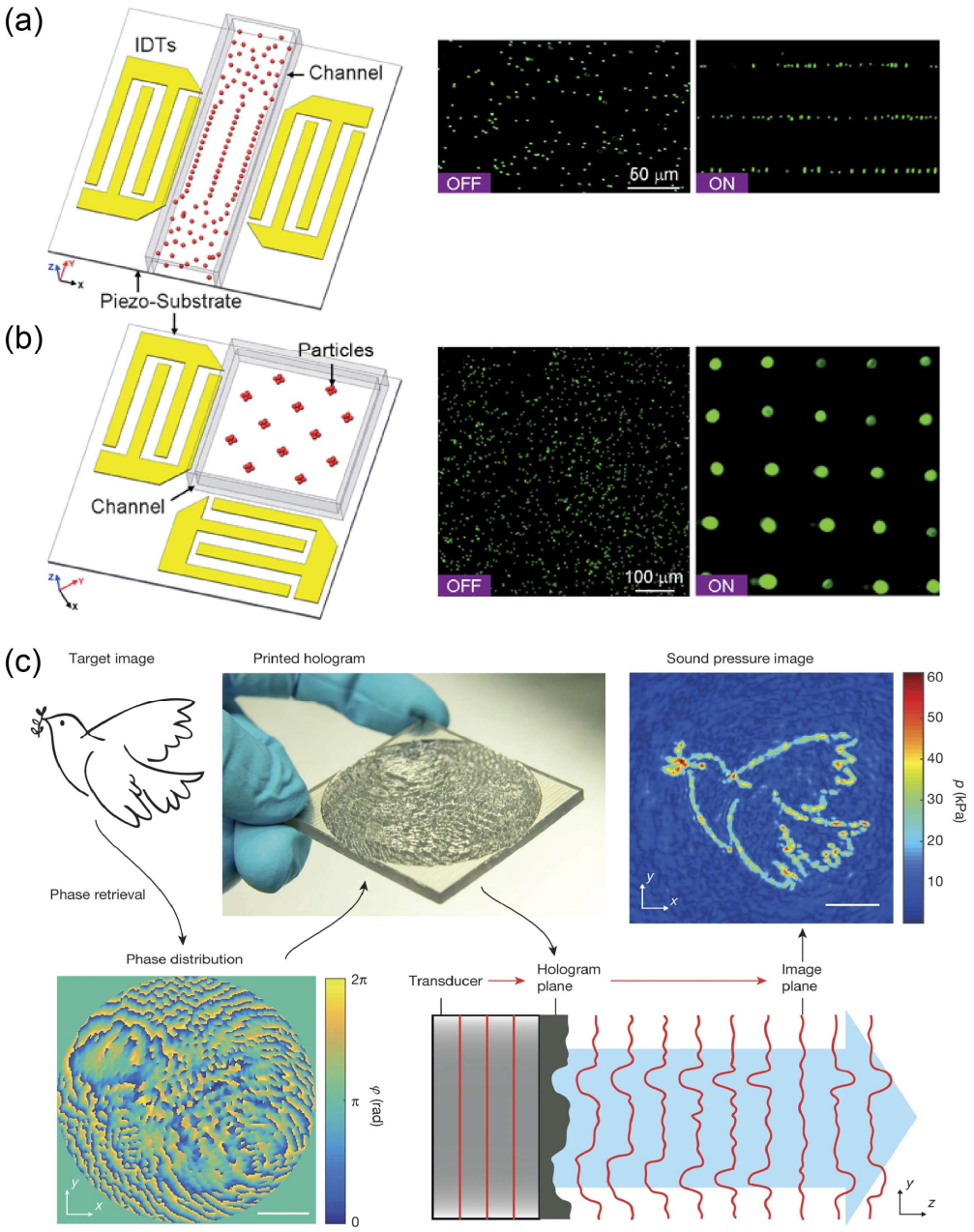

Figure 1.11. Acoustofluidic systems for 2D cell patterning. (a) Line pattern.[77] (b) Dots array pattern.[77] (c) Irregular pattern: pigeon image shape.[83]

Rotation:

Controllable rotational manipulation of microscale objects benefits various fields, as it permits observation of cells and small organisms from arbitrary angles and simplifies procedures for analysing cell mechanics, characterising biosample physiology, and performing microsurgery.[84] Acoustic-based rotational manipulation has recently emerged as a promising method for rotating microparticles, particularly in biological samples. Based on the working mechanism, acoustofluidics-enabled rotation can be

classified into two groups: bulk acoustic wave (BAW)-based rotations (including microbubble-based,[85, 86, 87, 88] microstructure-based,[89, 90] standing-wave superposition -based.[91, 92]) and SAW-based rotations.[93, 94]

For microbubble-, microstructure-, and standing-wave superposition-based rotations all rely on bulk acoustic wave (BAW) actuation, but the source of the rotational driving force differs. As shown in Fig. 1.12a, the trapped microbubbles are driven into oscillation, generating steady microvortices that precisely rotate a lily pollen grain, producing stable out-of-plane rotation. Because the fluorescent dye binds nucleic acids-DNA, the vegetative nucleus of the bicellular lily pollen grain can be visualised during rotation. By capturing multiple rotations at different focal planes—enabled by the grain's ellipsoidal (non-symmetric) shape—a dense 3D reconstruction of the fluorescently labelled lily pollen grain can be built.[85] For microstructure-based rotation, applying an external acoustic field to the microchannel causes sharp-edge structures to oscillate, generating acoustic streaming that, in turn, rotates single HeLa cells (Fig. 1.12b).[89] For standing-wave superposition-based rotation, an ultrasound acoustic trap was developed that levitates and reproducibly reorients zebrafish larvae and tumour spheroids for multi-angle optical coherence tomography (OCT), enabling non-contact, repeatable acquisition from arbitrary views for improved volumetric imaging (Fig. 1.12c).[91] For SAW-induced rotation, interdigital transducers (IDTs) are integrated with a microchannel whose dimensions are specifically designed to induce acoustic streaming for bioparticle rotation. As shown in Fig. 1.12d, the actuation of a pair of IDTs induces a large streaming vortex in the microchannel, which in turn rotates *C. elegans* to different orientations. Conventionally, examining *C. elegans* neurons is difficult without confocal microscopy. By controllably rotating *C. elegans* to any angle using the SAW chip, fluorescent images of neurons from distinct orientations can be acquired, clearly revealing the worms' biological characteristics.[94]

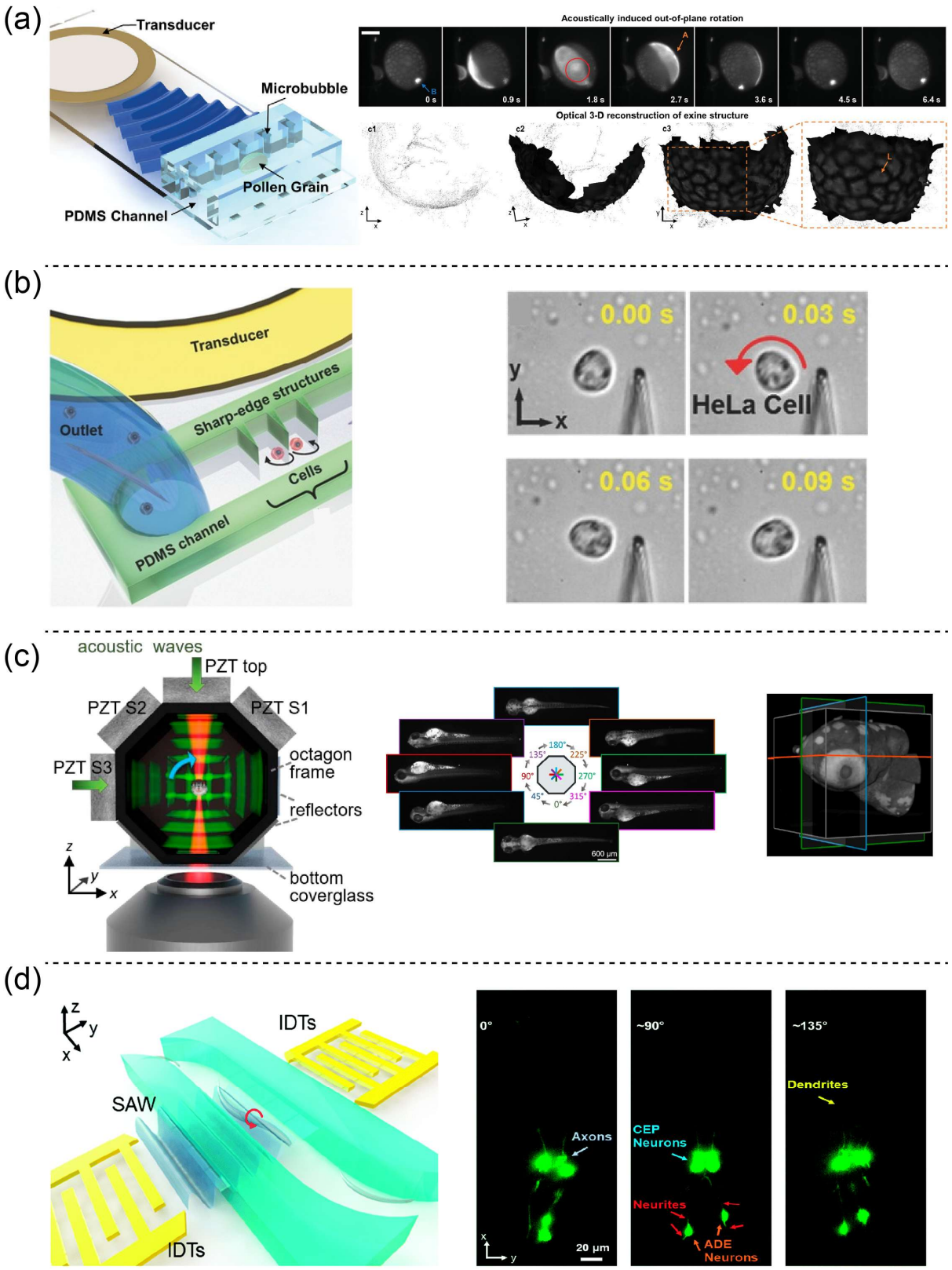

Figure 1.12. Acoustofluidic devices for bioparticle rotation. (a) Microbubble-based rotation.[85] (b) Microstructure-based rotation.[89] (c) Standing-wave superposition-based rotation.[91] (d) SAWs-based rotation.[94]

1.4.2 Tissue-Level Application

Targeted drug delivery

A major challenge in the drug delivery field is to effectively target and deliver therapeutic agents to their intended destinations. Acoustofluidic devices have therefore been explored as versatile tools to transiently and reversibly modulate biological barriers for drug transport. In practice, development at the tissue level has focused on two representative barriers: the skin (opening the stratum corneum for transdermal delivery)[63, 95, 96, 97, 98] and the brain (opening the blood–brain barrier for central nervous system delivery).[64, 99, 100]

For skin tissue transdermal drug delivery, acoustic devices typically rely on either cavitation (bubble oscillation and collapse) or non-cavitation ultrasound (pressure gradients and oscillations) to increase stratum corneum (SC) permeability. As a representative example (Fig. 1.13a), a conformable ultrasound patch (cUSP) induces cavitation in the coupling fluid between the patch and skin. The cUSP comprises piezoelectric transducers embedded in a soft elastomer, creating localised cavitation pockets over large areas of conformal contact. This design achieved a 26.2-fold enhancement of niacinamide delivery in a porcine model within 10 minutes compared with passive diffusion.[95] For brain tissue central nervous system (CNS) delivery, traditional acoustic technologies normally use focused ultrasound with concomitant administration of intravenous microbubbles. When the acoustic focus overlaps the microbubbles, their oscillation mechanically perturbs endothelial cells and transiently opens intercellular spaces, permitting drug passage the blood–brain barrier (BBB). In contrast, a more recent SAW-based acoustofluidic approach opens the BBB without exogenous microbubbles. The acoustofluidic transwell (AFT) was developed for reversible disruption of the BBB (Fig. 1.13b). The AFT comprises a transwell insert, in which the BBB model is established, and a SAW transducer implemented using open-source electronics based on printed-circuit-board techniques. In this device, SAW stimulation increased transendothelial permeability to sodium fluorescein and FITC–dextran of various molecular weights, primarily due to apparent stretching of intercellular (tight-junction) spaces. Further *in-vivo* study, a zebrafish model further demonstrated that SAW exposure promoted penetration of sodium fluorescein into the CNS.[64]

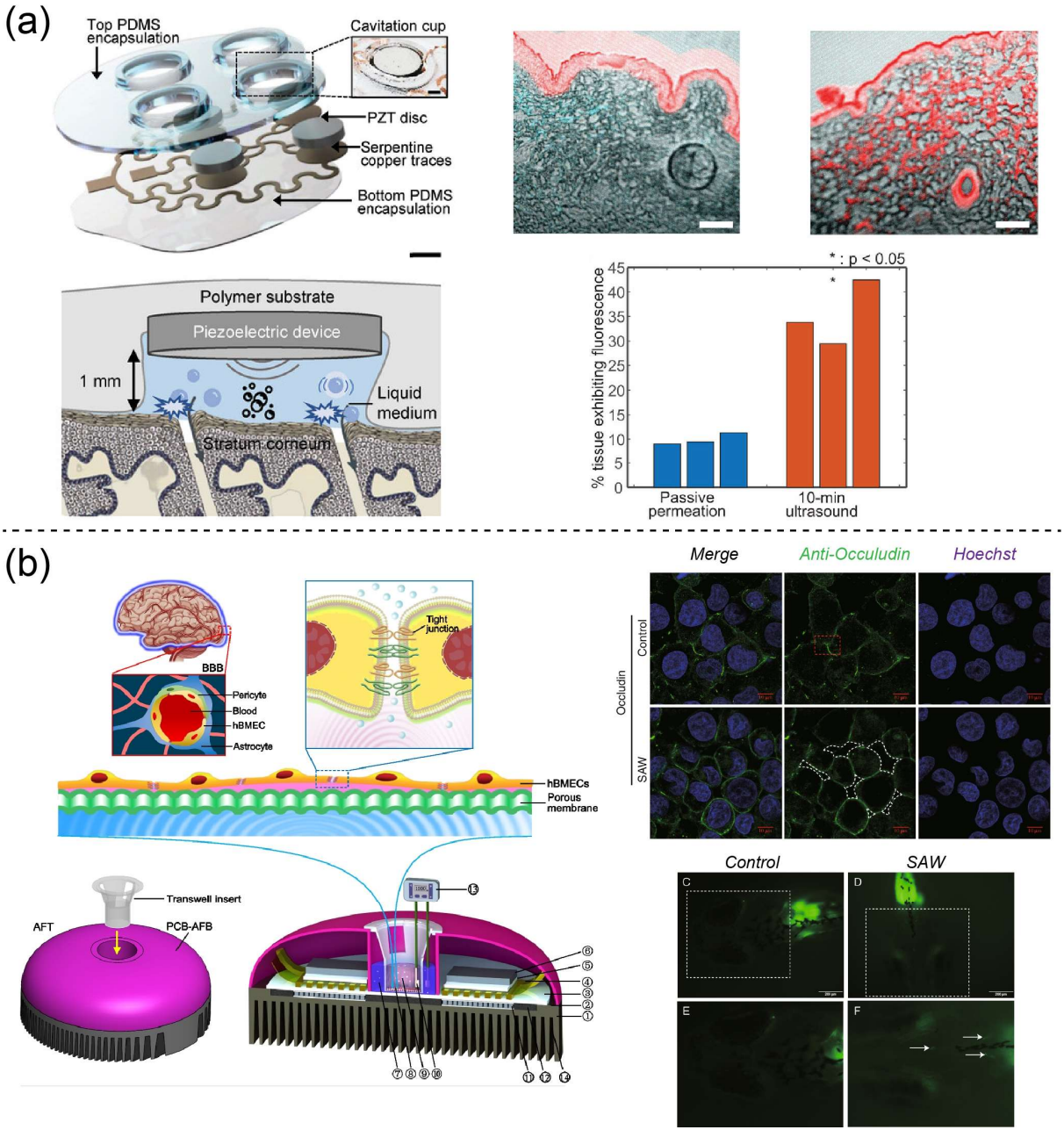

Figure 1.13. Acoustofluidic devices for drug delivery targeting to tissues. (a) Overcome SC layer for skin tissue transdermal drug delivery.[95] (b) Overcome BBB for brain tissue CNS drug delivery.[64]

1.5 Objectives and Thesis Outline

This PhD thesis describes my contribution to acoustofluidic devices manipulation for biomedical application in cell level and tissue level. The key contributions are: (1) Developed an acoustofluidic device named MARC (multi-view acoustofluidic rotation cytometry) for cell-level manipulation. MARC enhances cellular morphology analysis through comprehensive, multi-angle observations, and amplifies subtle cytological differences for enhanced cell phenotyping across various cell types and between cancerous and normal cells. (2) Developed another acoustofluidic device named ADAP (acoustic droplets activated permeation) for tissue-level manipulation/perturbation. ADAP achieves substantial improvements in transdermal drug delivery efficiency in *ex-vivo* tests, increasing delivery by approximately 31- to 82-fold compared with passive diffusion, and a 5-minute *in-vivo* ADAP treatment fully restores blood glucose levels in hypoglycaemic mouse models without observable skin damage.

The thesis comprises five chapters, summarised as follows:

Chapter 1: Introduces the importance of manipulation and its applications in biomedicine. Compares five mainstream manipulation technologies used in biomedical studies and highlights the advantages of acoustic methods. Presents representative biomedical applications enabled by acoustofluidic devices for cell-level and tissue-level manipulation.

Chapter 2: Provides fundamental background in acoustofluidics, including a brief history of sound, how sound waves work and wave types, and the relevant theories and working mechanisms for acoustic manipulation. Finally, outlines the two mainstream types of acoustofluidic devices.

Chapter 3: Describes the motivation for developing the MARC device, including its design and optimisation, fabrication and implementation, and parameter tuning to achieve controllable, high-throughput cell rotation. Evaluates its capability and performance in cytopathological detection compared with traditional 2D detection. Much of the text in this chapter is reproduced and/or adapted from our article published in *Advanced Science*.[101]

Chapter 4: Presents the motivation for building the ADAP device, its design, optimisation, and development; and the testing and characterisation of ADAP-induced perturbation. Reports *ex-vivo* permeation evaluation using drugs with various molecular weight and *in-vivo* therapy validation using the hypoglycemia mouse model. This project has been summarised in a research article currently under peer review.

Chapter 5: Summarises the two research works and outlines future directions for advancing these studies and developing improved acoustofluidic manipulation technologies.

Chapter 2: Acoustofluidic

2.1 Basic of Acoustofluidic

Acoustofluidic has an ancient history. In the Chinese Han dynasty (202 BC-AD 9), the Chinese Spouting Bowl was used as a tool to foster happiness, prolong life, and increase strength. As shown in Fig. 2.1, by rubbing the bowl's handles, vibrations are excited that couple to the liquid and drive continuous fountain-like jets.[102] This offers a vivid early example of acoustofluidics. As the term suggests, acoustofluidics uses acoustic waves to interact with fluids in a contact-free and biocompatible manner.[103] In recent decades, acoustofluidic devices have been increasingly adopted in biomedical research, enabling manipulation from nanoscale extracellular vesicles to millimetre-scale tissue-engineering constructs.[73] To fully understand the principles of acoustofluidics, it is first essential to establish a solid grasp of the basic concepts of waves.

Figure 2.1. Chinese Spouting Bowl and its working phenomena illustration. [source from https://www.prc68.com/I/Images/ChineseSpoutingBowlXXb.jpg]

2.1.1 Sound Waves

Sound (or sound wave) is an alteration in pressure, stress, particle displacement, or particle velocity that propagates through an elastic medium, or the superposition of such propagated alterations.[104]

All sound is generated by the motion of a source. For example, consider a piston (as in a loudspeaker) moving into an air volume. Its motion produces a local region where

density and pressure are slightly higher than their ambient values. If the piston displacement is extremely small, the molecular motion can be accommodated without effectively transferring energy between molecules, and no appreciable sound is produced. Likewise, if the source moves very slowly, the air flows gently around it, continuously equalizing pressure, and again no sound is created. However, if the piston's motion is sufficiently large and fast that there is not enough time for compensating flow, nearby molecules are forced together, locally compressing the air and creating a region of higher pressure and density. The compressed molecules then rush away from the high-pressure region, transferring momentum to adjacent molecules. When the piston moves back and forth, a wave is propagated by small oscillatory (out-and-back) motions of successive fluid elements along the direction of travel. Energy is conveyed through alternating regions of compression and rarefaction (the low-pressure/low-density "expansion" phase of a longitudinal sound wave, opposite to compression), accompanied by corresponding changes in particle velocity. The material properties of mass and elasticity enable this propagation, allowing the wave to travel through the surrounding medium and be detected by the ear or by a microphone.

As a wave propagates through a medium, particles oscillate back and forth as the wave passes. Regardless of the combination of wave motion and propagation medium, there is always a series of general equations that describe sound wave propagation through the medium, which can be expressed as:[105]

$$y(x,t) = Asin(kx \pm \omega t \pm \varphi) \tag{2.1}$$

$$k = \frac{2\pi}{\lambda} = \frac{\omega}{c} \tag{2.2}$$

$$\lambda = \frac{c}{f} \tag{2.3}$$

$$f = \frac{1}{T} = \frac{\omega}{2\pi} \tag{2.4}$$

where A, k, x , ω, t, φ , λ , c , f and T represent wave amplitude (Pa), wavenumber (rad/m), position (m), angular frequency (rad/s), time (s), phase (radians), wavelength (m), speed of sound propagation (m/s), frequency (Hz) and period (s). As shown in Fig. 2.2, the wave propagates from left to right. At the time t_1, the wave travels one full

wave cycles (λ), which are set by the speed of sound and the actuation frequency. Adding a positive phase shift of π ($\varphi = \pi$) is equivalent to shifting the spatial waveform by $\frac{\lambda}{2}$ (i.e., peaks and troughs swap). When at the time t_2, the wave moves two times distance than the time t_1. For clarity, Fig. 2.2 shows only a short segment of the sinusoidal waveform; a single-frequency component continues beyond the plotted region.

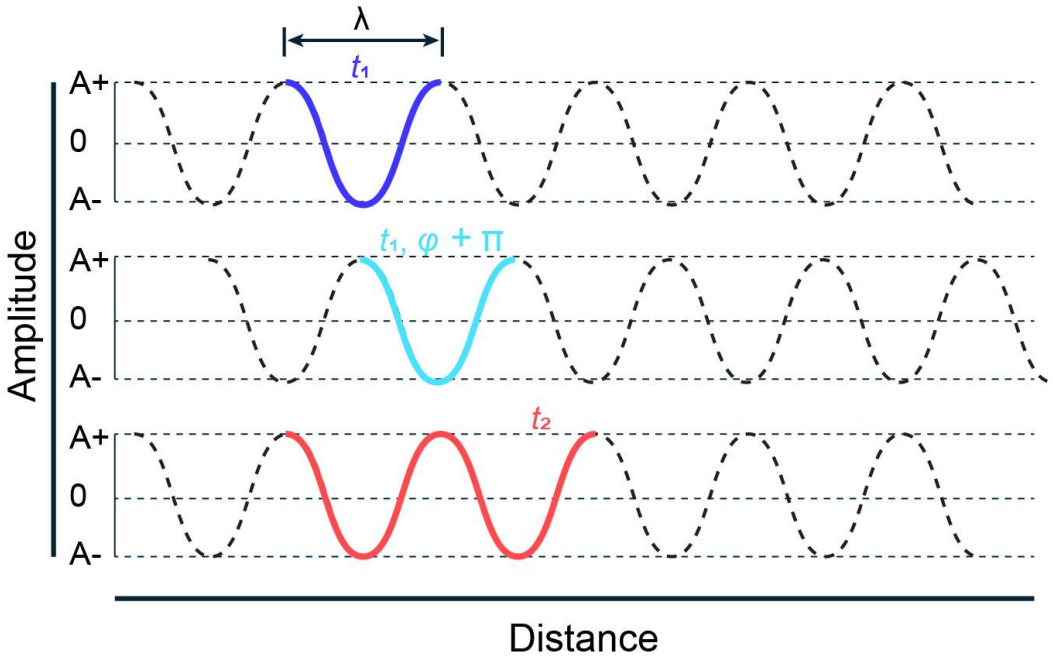

Figure 2.2. Plot for sound wave in the spatial domain at time t_1, t_1 with phase shift of π, and at different time intervals t_2. Only a short segment of the continuous sinusoid is shown for clarity (dashed curves indicate continuation beyond the plotted window).

2.1.2 Superposition

Sound can be a single pure tone, but more commonly it is a combination of many tones. Even the simplest telephone dial tone is the sum of two single-frequency components (350 and 440 Hz), and the acoustic environments in our daily life are far more complex and involve multiple wave combinations. When several waves occur simultaneously, the total pressure or displacement amplitude is the sum of their values at any one time. This behaviour is referred to as a linear superposition of waves and is most useful because complex periodic waveforms can be constructed by adding contributions from many sine and cosine functions. Consider two identical waves traveling in opposite directions (Fig. 2.3). At time t_1 the waves propagate toward one

another. When both waves have a phase difference by π are superposed at time t_2, the peak of one coincides with the trough of the other and their superposition produces cancellation. In contrast, if at time t_3 the two waves have zero phase difference, peaks align with peaks and troughs with troughs, yielding a standing wave with double the amplitude. For clarity, Fig. 2.3 shows only a short segment of the sinusoidal waveform; a single-frequency component continues beyond the plotted region.

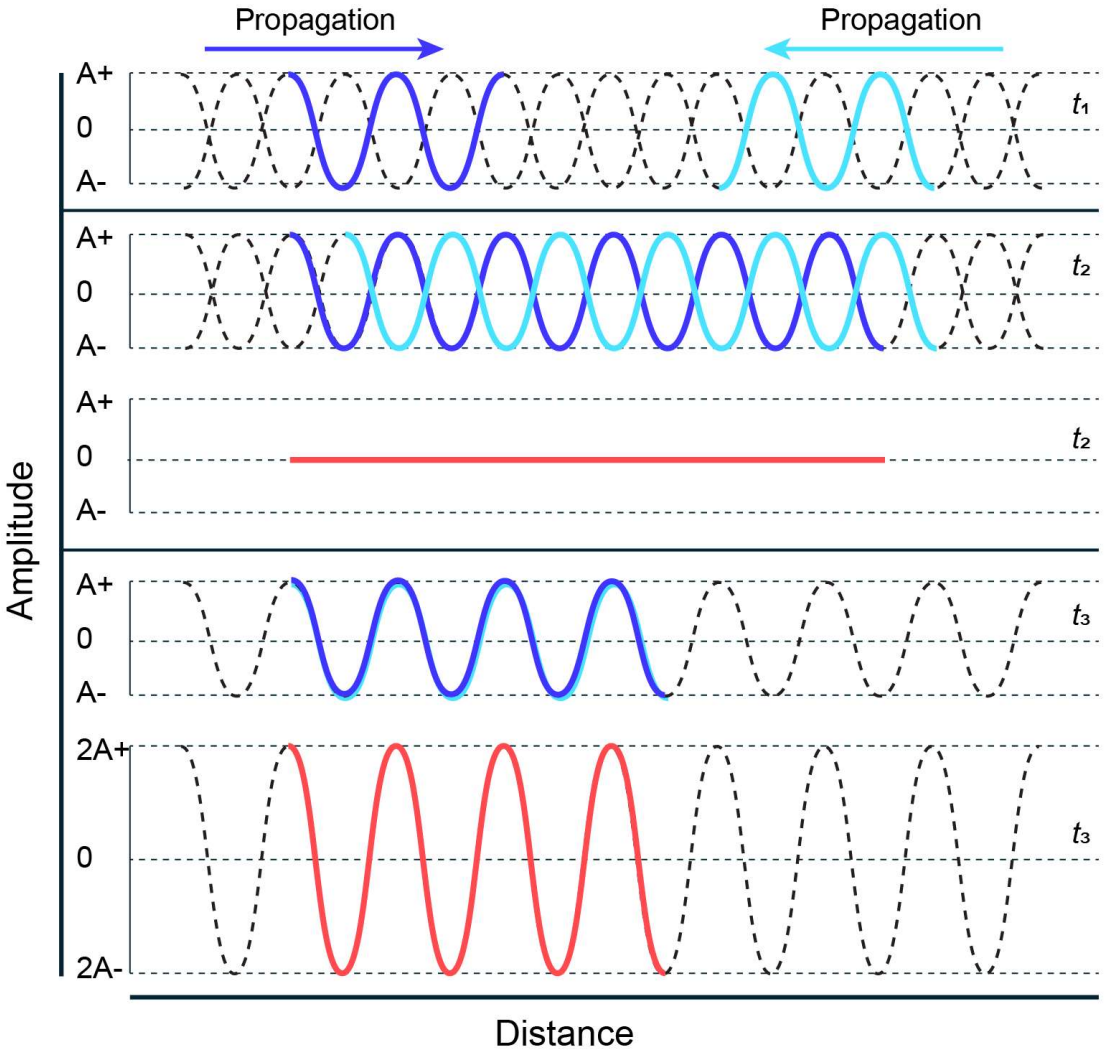

Figure 2.3. Plot illustration of two counterpropagating identical traveling wave at different intersection conditions forming cancellation and standing wave. Only a short segment of the continuous sinusoid is shown for clarity (dashed curves indicate continuation beyond the plotted window).

2.1.3 Wave Types

Based on how a wave vibrates and propagates through the host medium, it can be categorized into two groups: body waves and surface waves.

Body waves propagate through the entire host medium. In acoustofluidics, they are commonly referred to as bulk acoustic waves (BAWs).[106] Based on the direction of propagation relative to the host-medium oscillation, BAWs are classified as longitudinal or transverse. As shown in Fig. 2.4a, the medium is initially undeformed. When a longitudinal wave propagates along the x-axis (Fig. 2.4b), it travels parallel to the medium's oscillation direction and results in compression and expansion of the medium's lattice. By contrast, when a transverse wave propagates along the x-axis, it propagates perpendicularly to medium oscillation direction. Depending on the host-medium oscillation direction, transverse waves can be horizontal (along y-axis, Fig. 2.4c) or vertical (along z-axis, Fig. 2.4d).

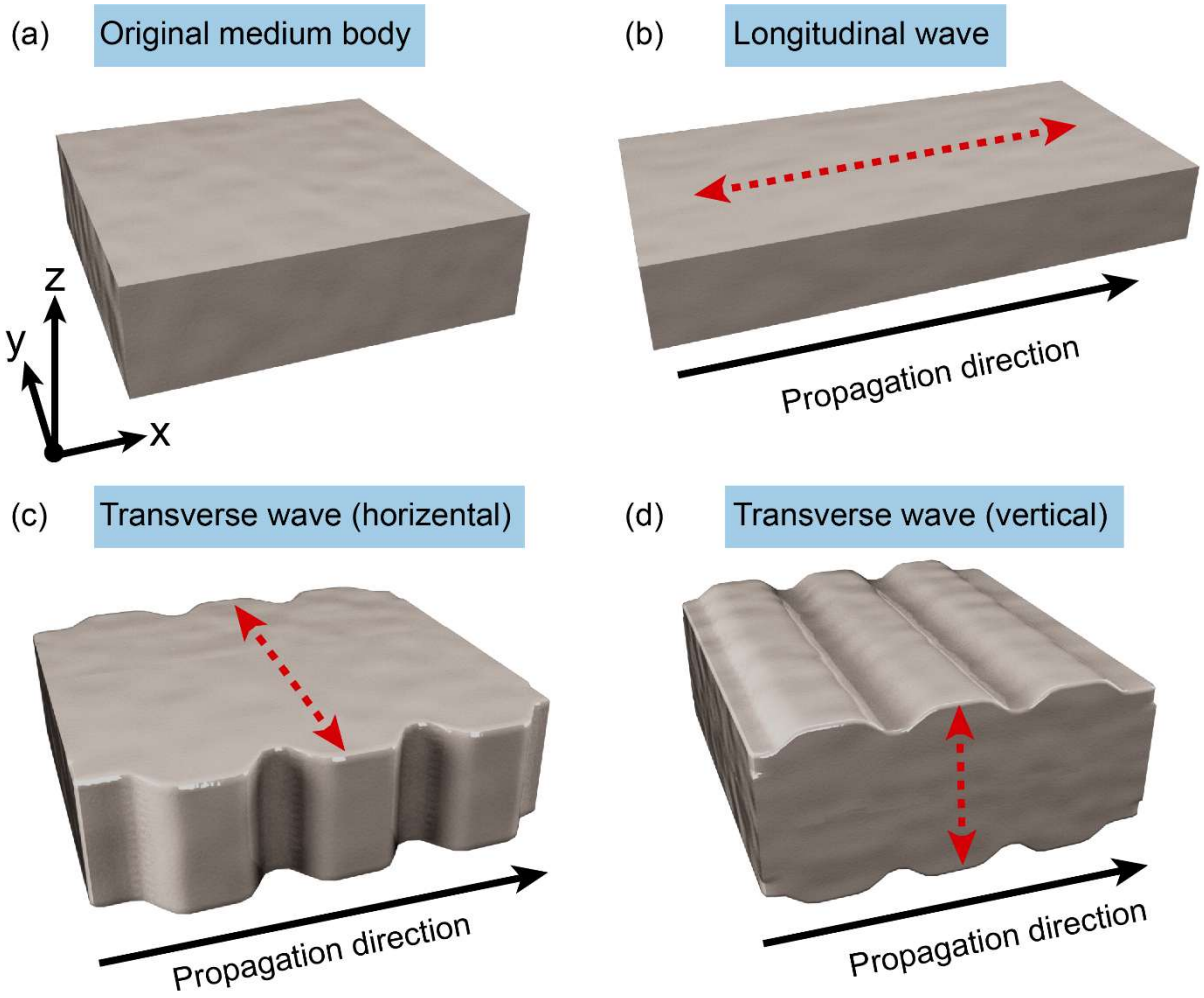

Figure 2.4. Several types of bulk wave illustrations. (a) The original host medium with no deformation. (b) Longitudinal wave. (c) Transverse wave in horizontal. (d) Transverse wave in vertical.

Surface waves, are waves traveling along the surface of the medium and are usually referred to as surface acoustic waves (SAWs) in acoustofluidics.[106] SAWs can be further separated into three types: Rayleigh waves, shear-horizontal waves, and Love waves. Rayleigh waves, first proposed by Lord Rayleigh in 1885, move with elliptical particle motion, producing both vertical and horizontal components in the direction of propagation.[107] The caused medium particle motion consists of elliptical motions (generally retrograde elliptical) in the vertical plane (i.e., out-of-plane) and parallel to the direction of wave propagation (Fig. 2.5a). Shear-horizontal surface acoustic waves (SH-SAWs) propagate in-plane on the substrate, with shear displacements parallel to the substrate surface. Figure 2.5b shows the host-medium displacement when an SH-SAW propagates along the x-axis direction, the vibration displacements are along the y-axis direction, parallel to the substrate. This piezoelectrically stiffened surface transverse wave exists due to the piezoelectric coupling effect.[108] Love waves occur in an SH-SAW device whose surface is covered with a thin wave-guide layer (typically of micron or sub-micron thickness), such as SiO_2, ZnO or polymers (Fig. 2.5c). The acoustic velocity in the wave-guide layer is much lower than in the substrate; therefore, the generated Love waves are largely trapped within this thin layer, leading to high sensitivity.[109, 110]

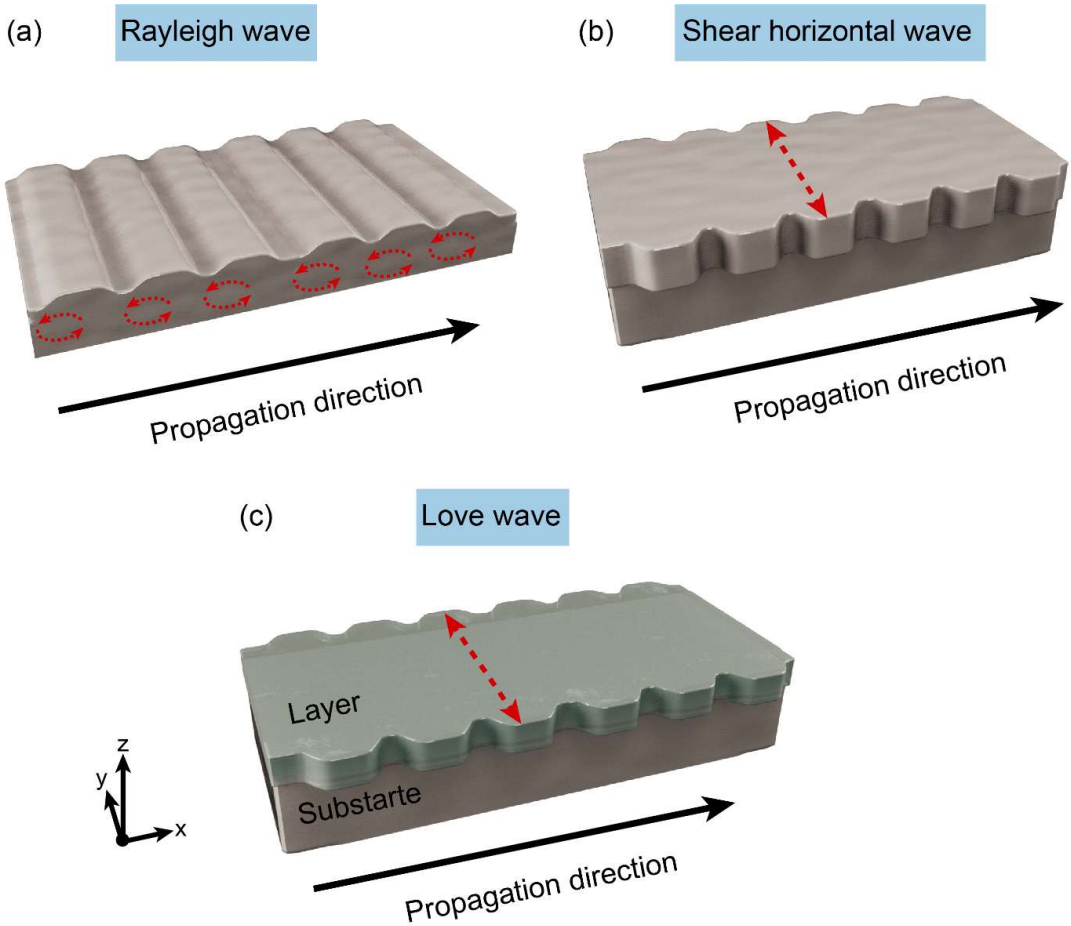

Figure 2.5. Several types of surface acoustic wave illustration. (a) Rayleigh wave. (b) Shear horizontal wave.(c) Love wave.

Another type of sound waves that is difficult to classify strictly as BAWs or SAWs are Lamb waves. These waves are generated when the substrate thickness is smaller than or comparable to the wavelength.[111] Typically, Lamb waves propagate in thin film piezoelectric on a membrane structure have two propagating modes: asymmetrical and symmetrical.[112] As shown in Fig. 2.6, both type Lamb waves travel along the whole plate structure (i.e., along both top and bottom surfaces), resulting in two free surfaces as guiding boundaries instead of just one. In the asymmetric mode, at higher-order frequencies or when the substrate thickness is larger than the wavelength the medium particle move similar to Rayleigh wave (Fig. 2.6a). While in the symmetric mode, the medium particles oscillate look like a bulk transverse vertical wave (Fig. 2.6b).

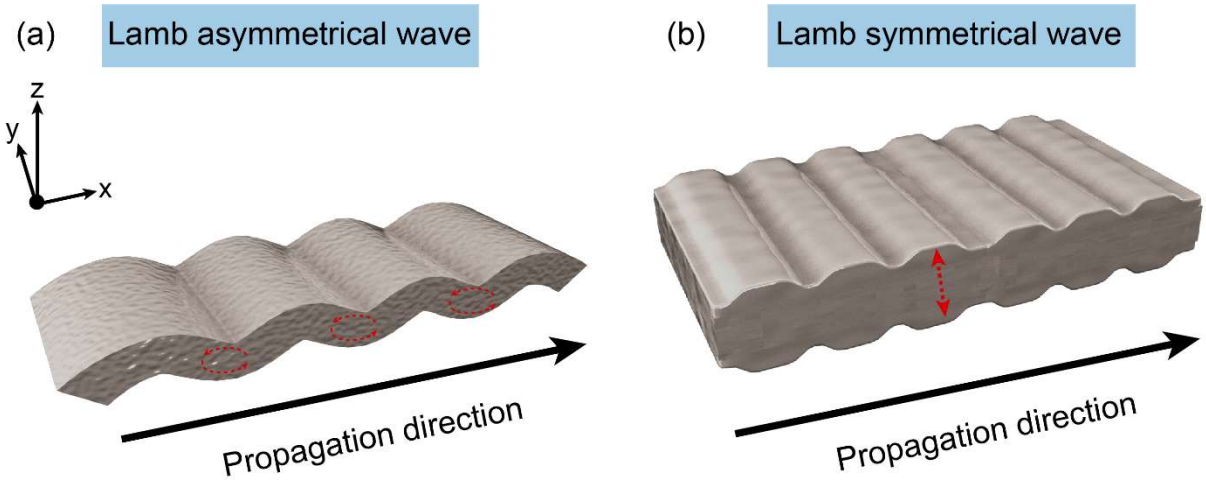

Figure 2.6. Two types of Lamb wave illustrations. (a) Lamb wave in asymmetrical mode. (b) Lamb wave in symmetrical mode. Unlike the bulk transverse wave in Fig. 2.4d, Lamb waves are guided plate waves whose displacement field is distributed through the thickness and constrained by the two free surfaces; "symmetric/asymmetric" refers to whether the displacement profile is symmetric or antisymmetric about the plate mid-plane (not simply "vertical" or "horizontal" motion).

2.2 Piezoelectricity and Piezoelectric Materials

Acoustic waves can be generated by piezoelectric materials, which rely on piezoelectricity to convert energy from an oscillating electric field into mechanical vibration. The first discovery of piezoelectricity was made by the young brothers Jacques and Pierre Curie, who found that compression or decompression of asymmetric crystals along their hemihedral axes produces electric polarization with opposite sign, and they announced the piezoelectric effect to the French Academy of Science on August 2, 1880.[113] Specifically, deformation of a piezoelectric material induces an asymmetric shift of charges, resulting in electric polarization and consequent electricity generation. This phenomenon is known as the direct piezoelectric effect. Conversely, piezoelectric materials can undergo strain in response to the application of an electric field; this mechanism is called the reverse piezoelectric effect.[114]

While, Piezoelectricity exists in piezoelectric materials, which are broadly classified into two groups: natural and man-made. Natural piezoelectric materials include quartz (SiO_2), topaz, tourmaline-group minerals, Rochelle salt, and some natural organic materials such as silk, wood, rubber, dentin, bone, hair, and enamel. Man-made

piezoelectric materials are typically grouped into ceramics (Lead zirconate titanate-PZT, Lithium niobate-$LiNbO_3$, and Zinc oxide-ZnO etc.), polymers (Nylon 11, Poly vinylidene difluoride: PVDF, and Polylactic acid: PLA etc.), and composite-based materials (PVDF-PZT, PVDF-ZnO, etc.). All piezoelectric materials have their advantages and disadvantages. For example, natural crystal–based materials have a high mechanical quality factor but are expensive and difficult to process. Ceramic-based materials exhibit higher piezoelectric constants, but their brittleness limits usability. Polymer-based materials offer higher flexibility, but their piezoelectric constants are lower than those of ceramics. Composite-based materials can be suitable because they combine the synergistic effects of polymer matrices and piezoelectric fillers; however, inconsistent polarization directions can lead to neutralization effects.[115]

In acoustofluidics, selecting a piezoelectric material generally depends on three properties: the effective electromechanical coupling coefficient (k_{eff}), the speed of sound in the substrate (c_s), and the overall crystal structure. The coupling coefficient quantifies the efficiency of converting electrical energy into mechanical deformation, while the speed of sound aids in designing actuators with the desired wavelength or operating frequency. The overall crystal structure refers to both the crystal unit cell and the crystallographic orientation.

2.3 Theory and Mechanism

Fluid dynamics enables the study of the behaviour of fluids under the influence of external forces such as acoustic forces. This section delves into the fundamental equations of fluid dynamics and explores the forces specific to Acoustofluidics.

2.3.1 Acoustofluidic Theories

The fundamental equations governing fluid dynamics are the continuity and Navier–Stokes equations, which describe how a fluid's velocity and pressure change in response to external forces and internal properties.[116, 117] In acoustofluidics, the primary governing equation is the continuity equation:

$$\frac{\partial \rho}{\partial t} + \nabla \cdot (\rho \boldsymbol{v}) = 0 \tag{2.5}$$

Where ρ,v and t are the fluid mass density, fluid velocity, and time. In basic terms, it means that the mass is conserved, and the change in density is due to fluid flow. The

second governing equation, the Navier–Stokes equation, describes the motion of fluids and is derived from the conservation of momentum and the momentum density:

$$\rho\left(\frac{\partial \boldsymbol{v}}{\partial t} + (\boldsymbol{v}\cdot\nabla)\boldsymbol{v}\right) = -\nabla p + \mu\nabla^2\boldsymbol{v} + \left(\mu_b + \frac{\mu}{3}\right)\nabla(\nabla\cdot\boldsymbol{v}) \tag{2.6}$$

Where p, μ, and μ_b are the fluid pressure, dynamic shear viscosity of the fluid, and the bulk or dilatational viscosity. In short, the Navier–Stokes equation describes how the fluid velocity changes over time and space due to pressure gradients, viscous forces, and external forces. The left-hand side represents changes in the fluid's velocity (inertial terms), while the right-hand side accounts for pressure, viscosity, and other forces that affect the motion. For incompressible fluids, the characteristic flow velocities are much smaller than the speed of sound, so the fluid can be treated as incompressible. This yields $\nabla\cdot\boldsymbol{v} = 0$, which allows significant simplifications.

In microfluidic systems that incorporate acoustic waves, the dimensionless Reynolds number (R_e) is used to characterize the fluid flow by measuring the ratio of inertial to viscous forces. When viscous forces dominate, the flow is laminar; when inertial forces dominate, the flow is turbulent. The value of R_e depends on the flow velocity and the fluid–mechanical length scale, and is defined as:[117]

$$R_e = \frac{\rho\boldsymbol{v}L}{\eta} \tag{2.7}$$

Where L and η are the characteristic length scale and the dynamic viscosity of the fluid. If $R_e \gg 1$, the convective acceleration is indeed necessary and the flow will be nonlinear as a consequence. If $R_e \ll 1$, the wave propagates linearly, either because its amplitude is small (infinitesimal) or because dissipation within the fluid is sufficiently strong to attenuate the wave before nonlinear compressibility effects cause it to "overturn" and form a shock. In acoustofuidics, for small flow velocities, the $R_e \ll 1$, so the non-linear term is expected to be negligible.

However, the governing equations above are quite complex to solve. In acoustofluidics, perturbation theory is therefore used to obtain approximate solutions for pressure, density, and velocity fluctuations. The governing equations for acoustic waves in fluids can be derived from first- and second-order perturbation theory:[118]

$$p = p_0 + p_1 + p_2 \tag{2.8}$$

$$\rho = \rho_0 + \rho_1 + \rho_2 \tag{2.9}$$

$$\boldsymbol{\nu} = \boldsymbol{\nu}_0 + \boldsymbol{\nu}_1 + \boldsymbol{\nu}_2 \tag{2.10}$$

$$p_1 = c_0^2 \rho_1 \tag{2.11}$$

Where subscript 0, 1, 2, and c_0 denote the ambient environment (i.e., a quiescent liquid with no sound presence), the first-order correction, the second-order correction, and the speed of sound in the fluid. Under ambient conditions the liquid is still, so $\boldsymbol{\nu}_0 = 0$. By introducing these perturbation expansions, the continuity and Navier–Stokes equations can be solved order by order for the acoustic field components. The first-order perturbation solution describes the oscillatory acoustic wave motions, with $\boldsymbol{v}_1$ representing the acoustic velocity and p_1 indicating the acoustic pressure field. Employing these first-order solutions into second-order equations and time-averaging them yields the solution for acoustic streaming, which encompasses both harmonic and steady components. The time-averaged second-order velocity ($\boldsymbol{v}_2$) corresponds to acoustic streaming, induced by the transfer of energy and momentum from the acoustic waves to the fluid. The time-averaged second-order pressure (p_2) causes the generation of the acoustic radiation force.[119]

Based on the above, two main forces act on microparticles in acoustofluidics: the acoustic radiation force and acoustic streaming.

2.3.2 Acoustic Radiation Force

In principle, nonlinear sound propagation in a fluid generates a time-averaged acoustic pressure gradient, which gives rise to the acoustic radiation force (ARF) acting on particles.[120] There are two types of ARFs: the primary acoustic radiation force and the secondary acoustic radiation force. The primary acoustic radiation force is the force exerted on an individual particle by direct irradiation from the acoustic field. In contrast, the secondary acoustic radiation force arises from acoustic interactions between particles within the fluid.[121]

The acoustic radiation force and its effect on particles also depends on whether the waves are travelling or standing. King derived the acoustic radiation force acting in a traveling wave ($\boldsymbol{F}_{T-rad}$) as written:[122]

$$\boldsymbol{F}_{T-rad} = 2\pi\rho_l|A|^2(\kappa R_p)^6 \frac{9+2(1-\lambda_p)^2}{9(2+\lambda_p)^2} \tag{2.12}$$

$$\lambda_p = \frac{\rho_l}{\rho_p} \tag{2.13}$$

Where A, κ, R_p, λ_p, ρ_l, and ρ_p represent the complex amplitude of velocity potential, the wavenumber of acoustic radiation, the particle radius, the density of the liquid, and the density of the particle, respectively.

However, in a standing-wave field, the situation is different, and the ARF is given by:[123]

$$\boldsymbol{F}_{S-rad} = -\left(\frac{\pi p_0^2 V_p \beta_l}{2\lambda}\right)\varphi(\beta,\rho)sin(2\kappa x) \tag{2.14}$$

$$\varphi(\beta,\rho) = \frac{5\rho_p - 2\rho_l}{2\rho_p + \rho_l} - \frac{\beta_p}{\beta_l} \tag{2.15}$$

Where p_0, V_p, x, φ, β_p, and β_l represent the acoustic pressure amplitude, the particle volume, the axial distance of the particle from the pressure nodes, the acoustic contrast factor, the compressibility of the particle, and the compressibility of the fluid, respectively. The force $\boldsymbol{F}_{S-rad}$ drives a particle toward either the pressure nodes (PNs) or the pressure antinodes (ANs), as determined by the particle's acoustic contrast factor (φ). When particle has a positive acoustic contrast factor ($\varphi > 0$), particle moves toward the PNs; when particle has a negative acoustic contrast factor ($\varphi < 0$), it moves toward the ANs.

2.3.3 Acoustic Streaming

Acoustic streaming is another commonly utilized nonlinear acoustic effect for particle manipulation in acoustofluidics that converts acoustic energy into fluid flow.[124] Indeed, acoustic streaming is a steady fluid flow formed by viscous attenuation of an acoustic wave.[125] The microparticles in acoustic streaming are subjected to the resistance force of the fluid, which is called the Stokes drag force.[126] For a sphere of radius R_p in a low Reynold's number flow with medium viscosity η, the Stokes drag force ($\boldsymbol{F}_{drag}$) is:[127]

$$\boldsymbol{F}_{drag} = 6\pi\eta R_p(\boldsymbol{v} - \boldsymbol{v_p}) \tag{2.16}$$

Where $\boldsymbol{v}$, and $\boldsymbol{v_p}$ are the surrounding fluid flow velocity and the particle velocity, so $(\boldsymbol{v} - \boldsymbol{v_p})$ represents the relative velocity between fluid and particle.

Streaming flows vary greatly depending on the mechanism behind the attenuation of the acoustic wave. The variations include the velocity of the flow, the length scale of the flow and the geometry of the flow.[128] Usually, there are three main types of acoustic streaming phenomena: Eckart streaming, Schlichting streaming, and Rayleigh streaming, which can also be grouped as bulk-driven and boundary-driven streaming.[128, 129] Boundary-driven acoustic streaming arises from viscous dissipation of acoustic energy within the boundary layer along any solid structures (e.g., channel walls, micropillars, or sharp edges) whose lengths are comparable to or greater than one quarter of the acoustic wavelength in the direction of propagation. Near solid surfaces, the no-slip condition keeps the fluid at the boundary nearly stationary, creating a very thin viscous Stokes layer with steep velocity gradients. This localized effect generates small inner vortices known as Schlichting streaming, which in turn drive larger secondary flows away from the boundary, producing the counter-rotating outer vortex pairs characteristic of Rayleigh streaming (Fig. 2.7a). Put simply, Schlichting streaming occurs in the viscous boundary layer near surfaces, while Rayleigh streaming is the bulk vortex flow that this boundary-layer forcing drives (especially in standing waves). In contrast, bulk-driven streaming occurs as an acoustic wave travels through a fluid and its energy is gradually absorbed; the associated net momentum transfer produces a jet-like flow along the direction of propagation, known as Eckart streaming (or quartz wind). While boundary-layer streaming is governed primarily by fluid–solid interactions and tends to dominate in the smaller, confined dimensions of microfluidic devices, with whose length dimension is smaller than the wavelength ($L < \lambda$). Eckart streaming becomes more significant in larger channels where the system dimension greatly exceeds the acoustic wavelength ($L > \lambda$). In microfluidic devices, the small dimensions often mean that boundary-driven (Schlichting and Rayleigh) streaming dominates, whereas Eckart streaming becomes important in larger or specially designed channels.[130]

Microparticles in acoustofluidic channels are exposed to the acoustic radiation force and the acoustic streaming simultaneously. While the radiation force acting on a particle depends on its volume, the streaming moves the micro-object through the flow

previously developed inside the chamber that depends on the particle size. Consequently, the size of the manipulated bio-particle is crucial in acoustofluidics. When the acoustic radiation force and the Stokes drag force balance, the particle remains stationary, and the critical particle diameter ($2R_c$) is:[119]

$$2R_c = \sqrt{12\frac{\psi}{\varphi}} \tag{2.17}$$

Where ψ is a geometry-dependent factor of order unity. As shown in Fig. 2.7b, for small particle ($R < R_c$), the acoustic streaming induced Stoke drag force dominates ($\boldsymbol{F}_{rad} < \boldsymbol{F}_{drag}$) so particles follow along vortex streamlines. In contrast, for larger particles ($R > R_c$), the acoustic radiation force dominates ($\boldsymbol{F}_{rad} > \boldsymbol{F}_{drag}$), pushing the particles toward the pressure nodes PN or antinodes AN.

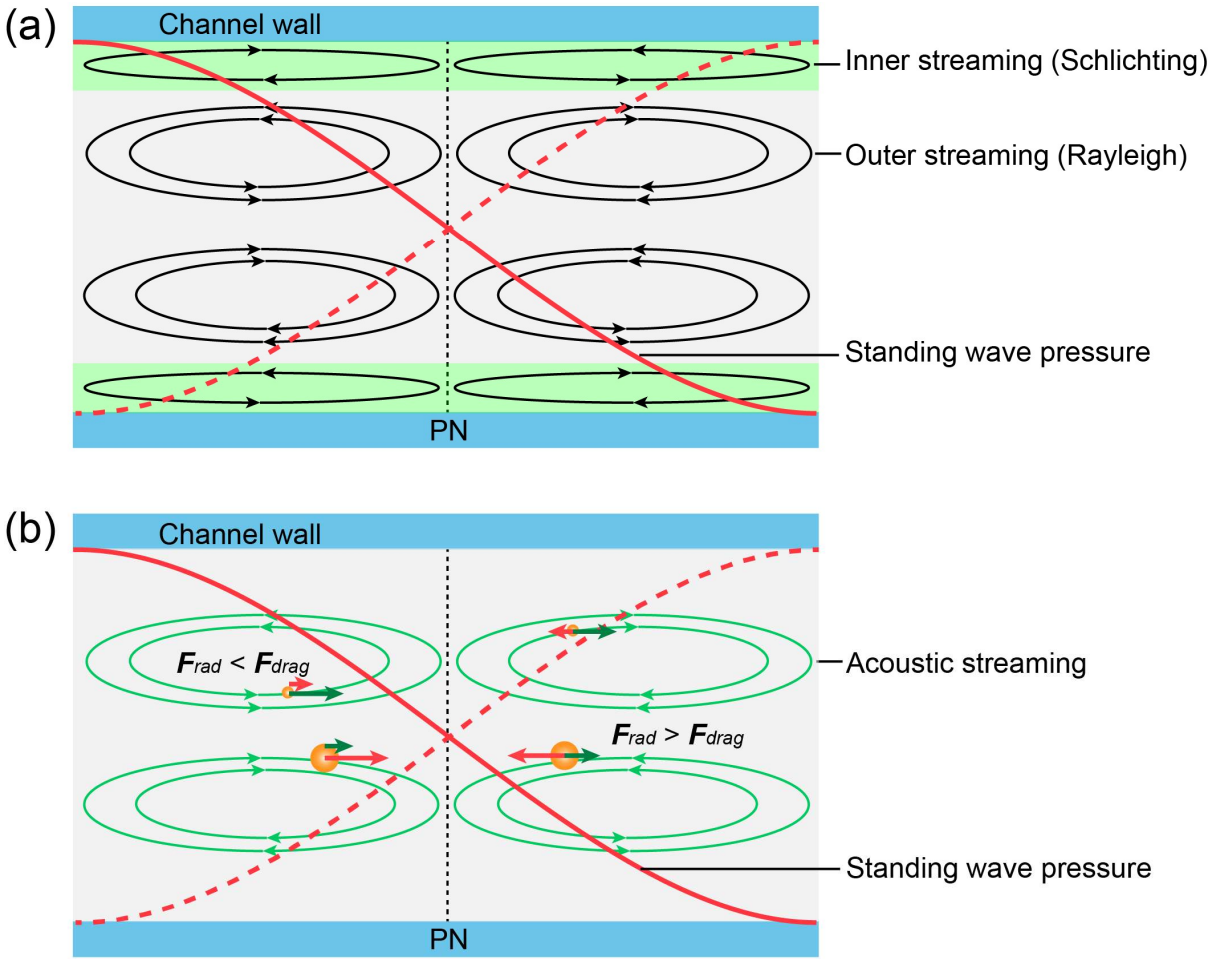

Figure 2.7. Acoustic streaming induced by a standing wave and particle movement at different sizes. (a) A standing wave induced boundary-driven streaming in the microchannel: inner (Schlichting) streaming and outer (Rayleigh)

streaming. (b) The impact of microparticle size for particle movement under experienced $\boldsymbol{F}_{rad}$ and $\boldsymbol{F}_{drag}$.

2.4 Acoustofluidic Devices

In acoustofluidics, an acoustofluidic device generates acoustic waves to manipulate particles and fluids in an adjacent chamber for various applications. The core component of the device is the piezoelectric transducer, usually made of piezoelectric materials, which can convert electrical signals to acoustic signals or vice versa (as detailed in Section 2.2). The driving electrical signal for the transducer is produced by a function generator and can be amplified with a power amplifier when greater acoustic pressures are required. Depending on acoustic wave generation and propagation characteristics, the transducer is usually categorized as a BAW transducer or a SAW transducer. Therefore, the corresponding devices are named BAW-based acoustofluidic devices and SAW-based acoustofluidic devices.[103]

2.4.1 BAW-based Acoustofluidic Devices

In BAW-based acoustofluidic devices, the bulk acoustic transducer is the core component, often made of lead zirconate titanate (PZT) polarized ceramic plates sandwiched by metal electrodes. The polarization and electric field are typically along the thickness direction or the radial direction, enabling thickness-mode or radial-mode vibrations at discrete resonances in the transducer.

The fluidic chamber is also important, as its walls reflect or absorb incident acoustic waves. Standing waves are commonly used in BAW acoustofluidics and can be formed as the result of acoustic waves reflected from the chamber wall. The acoustic properties (speed of sound, density, and acoustic impedance) and the chamber geometry influence the acoustic field pattern.[131, 132] Both acoustically hard materials (glass and silicon, whose acoustic impedance is high relative to water) and acoustically soft materials (polydimethylsiloxane, PDMS, and polymethyl methacrylate, PMMA, whose acoustic impedance is close to water) have been used to fabricate acoustofluidic chambers through microfabrication techniques. When the chamber is formed from hard materials, acoustic energy is reflected within the microchannel, leading to enhanced acoustic energy density for improved manipulation efficiency. By contrast, using soft materials leads to acoustic energy leakage or absorption, causing a loss of acoustic energy within the microchannel.[133] Nevertheless, soft polymers are

often deliberately chosen when strong wall reflections and high-Q (quality factor) cavity resonances are undesirable, their relatively low impedance mismatch to water and higher damping can reduce unwanted reflections/standing waves and suppress spurious wavemodes.[134, 135] In addition, PDMS is widely used in lab-on-a-chip systems because it is optically transparent, chemically inert/biocompatible, low-cost, and easy to fabricate and bond/seal.[136] The trade-off is increased attenuation/leakage (often requiring higher drive power and potentially increasing heating) and, due to mechanical compliance, greater susceptibility to deformation or resonance drift, which can reduce repeatability.

Based on the PZT transducer, BAW-based acoustofluidic devices can be categorized into three groups: single BAW transducer, hologram BAW transducer, and BAW transducer arrays (Fig. 2.8). The single BAW transducer device usually consists of a single PZT attached to a substrate with a microchannel, as shown in Fig. 2.8a. Although this type design is simple, it has been widely used in various applications, including droplet generation,[137, 138] bioparticle focusing,[139] and particle manipulation.[88, 140] To realize more complex particle manipulation, an effective and economical way to shape the field is to add acoustic artificial-structure holograms on the surface of the transducer, forming a hologram BAW transducer (Fig. 2.8b). These artificial structures can modify the output of a single transducer to generate a high-fidelity acoustic field as desired, providing unique features such as sub-wavelength-scale amplitude control and complex beam patterns. The shaped fields can then realize desired particle patterns and manipulation in 2D and 3D.[141, 142] Another group, BAW transducer arrays, has also been used to selectively manipulate particles (Fig. 2.8c). The elements in these arrays are individually driven to create arbitrary and dynamically tuneable wavefronts via superposition, enabling single-particle 3D manipulation and individual manipulation of up to 25 microparticles simultaneously.[143, 144]

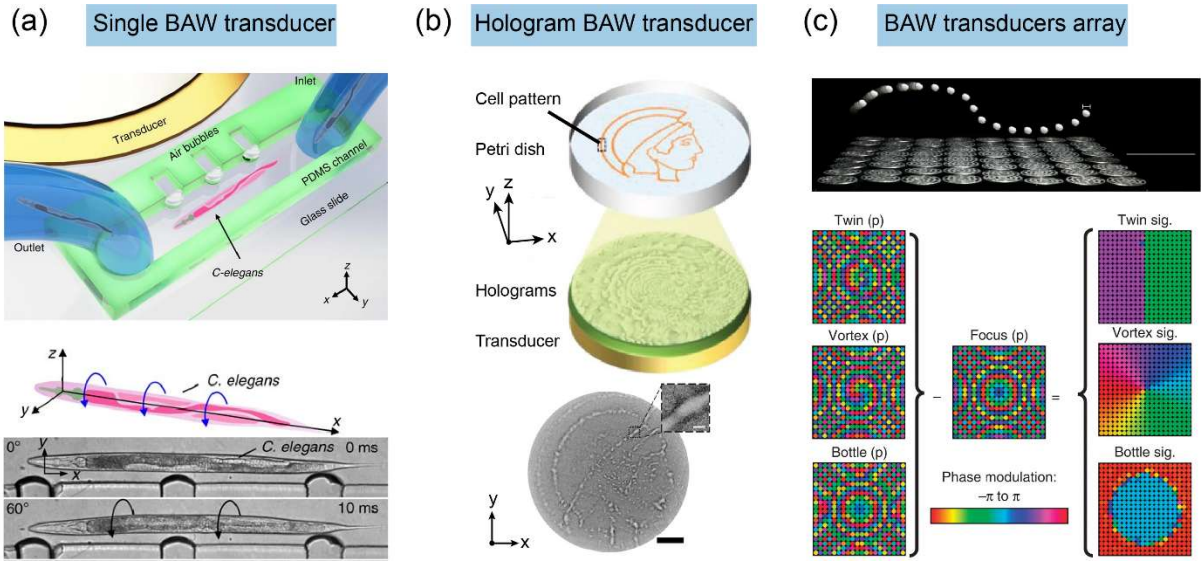

Figure 2.8. BAW-based transducers in acoustofluidics. (a) Single PZT transducer.[86] (b) Holographic BAW transducer.[82] (c) BAW phase transducers array.[144]

2.4.2 SAW-based Acoustofluidic Devices

In SAW-based acoustofluidic devices, interdigital electrodes—commonly called interdigital transducers (IDTs)—patterned on a piezoelectric substrate are the key components. An IDT consists of metallic fingers connected to a common electrode (bus bar) and interdigitated with a second set of metallic fingers attached to a second bus bar, all deposited directly onto the piezoelectric layer by standard lithographic techniques. The IDT structure determines the frequency, bandwidth, and directivity of the generated SAW. By varying the number, spacing, and aperture (overlapping length) of the metallic fingers, the generated SAW can be tuned (Fig. 2.9a). For most SAW devices, the piezoelectric substrate is often a 128º Y-cut lithium niobate (128°-Y-rotated, X-propagating $LiNbO_3$) wafer with a thickness of 500 μm.[103]

The geometry and acoustic properties of the microchamber, as well as the acoustic properties of the liquid (density, speed of sound, and viscosity) loaded on the substrate surface, all significantly influence the SAW behavior. If the fluid layer on the substrate is thinner than the viscous boundary layer, no sound propagates into the fluid and the fluid follows the propagation of the SAW. If the fluid layer is thicker than this depth but smaller than the wavelength of sound in the fluid at the operating frequency, sound enters the fluid to produce a 2D planar sound field. When the chamber height exceeds the wavelength of sound in the fluid, the SAW produces a longitudinal sound wave that propagates into the bulk from the substrate–fluid interface at the Rayleigh angle,

forming a leaky SAW and inducing fluid streaming (Fig. 2.9b). The Rayleigh angle is given by:[145]

$$\theta_R = \sin^{-1}\frac{c_l}{c_s} \tag{2.18}$$

Where c_l and c_s are the speed of sound in the fluid liquid and speed of sound in the substrate. For 128° Y-cut $LiNbO_3$, $c_l \approx 1490\, m/s$ and $c_s \approx 3900\, m/s$, yielding a Rayleigh angle of $\approx 22°$.[146]

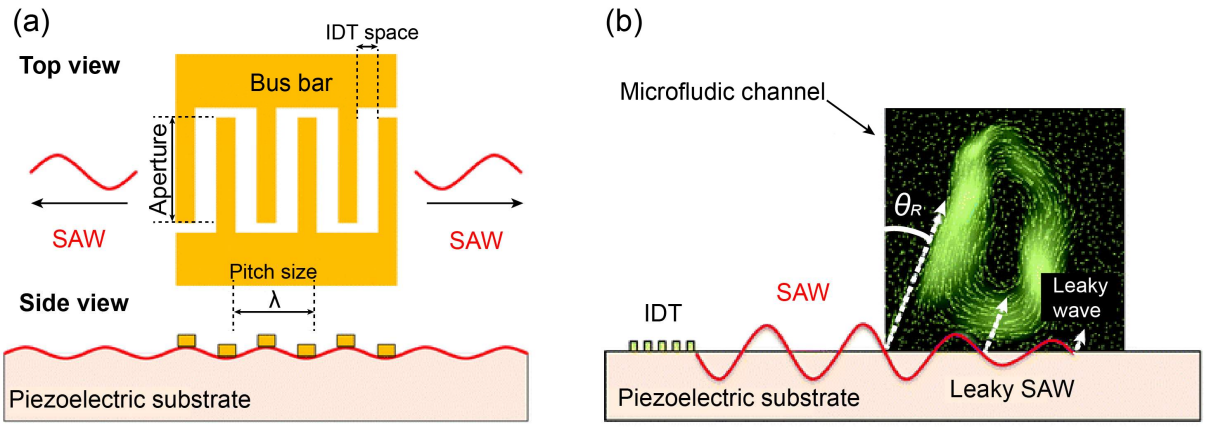

Figure 2.9. IDTs induced SAW generations and Leaky SAW. (a) IDT structure and generate SAW.[146] (b) Leaky SAW generation.[146]

Similar to BAW-based devices, SAW-based acoustofluidic devices can also be divided into three groups by considering the IDT transducer: single SAW transducer, hologram SAW transducer, and SAW transducer arrays (Fig. 2.10). In single SAW transducer devices, a single IDT generates a travelling SAW on the $LiNbO_3$ substrate, impacting the bonded microchannel or a liquid droplet at the substrate surface (Fig. 2.10a). This type of device has been widely used in cell sorting,[147, 148] nebulization,[149, 150] and droplet manipulation.[151, 152] Recently, more complex SAW fields have been achieved by altering the IDT shape to form so-called hologram SAW acoustofluidic devices.[153, 154] As shown in Fig. 2.10b, a focused acoustic vortex is synthesized by spiralling metallic electrodes deposited on the surface of a piezoelectric substrate. The IDT encodes the phase of the field, similar to a hologram, enabling generation of the targeted acoustic vortex.[155] Standing SAWs are also commonly used in acoustofluidics. Similar to BAW acoustofluidics, a pair of opposing IDTs—or an IDT with an opposing reflector—can form 1D standing SAWs in the substrate, whereas two pairs of IDTs arranged orthogonally can produce 2D standing SAWs. By fabricating pairs of IDTs

from multiple directions, SAW transducer array devices are formed. By activating pairs of IDTs from different directions, SAWs with various wavefields can be shaped for multifunctional bioparticle manipulation (Fig. 2.10c).[156]

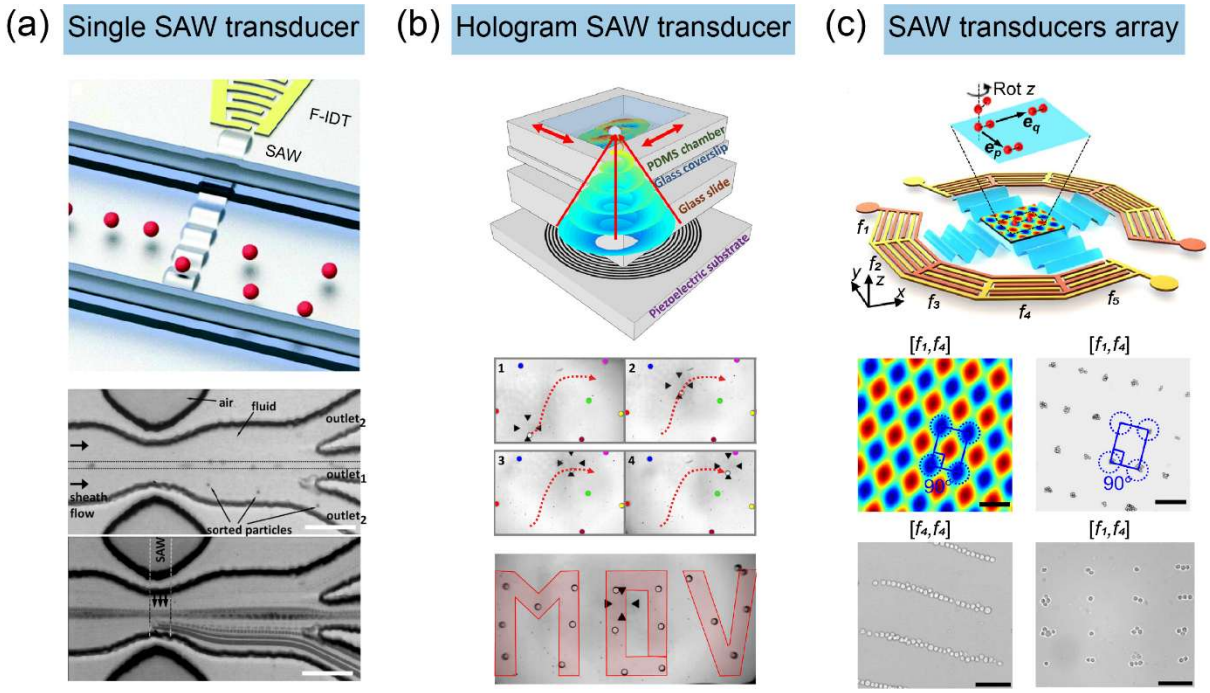

Figure 2.10. SAW-based transducers in acoustofluidics. (a) Single IDT transducer.[157] (b) Hologram IDT transducer.[155] (c) IDT transducer arrays.[156]

Chapter 3: Manipulation at the Cell Level for Pre-Cytopathological Screening

Cell-level manipulation is essential in clinical cytopathology, enabling detailed morphological analyses critical for disease diagnosis. In this chapter, we focus specifically on rotational manipulation and analysis of six cell lines, including cancerous and healthy cells. The distinct morphological and cytological characteristics of these cell lines make them suitable models for demonstrating the potential of advanced manipulation technologies in Recognizing the challenges and limitations posed by current cell-rotation and morphological-analysis methods—particularly regarding throughput, biocompatibility, and morphological clarity—we introduce the Multi-view Acoustofluidic Rotation Cytometry (MARC) device. This chapter outlines the design, optimization, experimental validation, and evaluation of MARC, demonstrating its unique ability to provide high-throughput, controllable, and detailed multi-angle cellular morphology analysis, thereby significantly enhancing the accuracy and efficiency of pre-cytopathological screening.

The corresponding content in this chapter has been published in *Advanced Science*:[101]

- X. Zhang, P. Dumčius, R. Mikhaylov, et al. Surface Acoustic Wave-Enhanced Multi-View Acoustofluidic Rotation Cytometry (MARC) for Pre-Cytopathological Screening. *Advanced Science*, 2024, 11, 2403574.

Author Contribution:

I (Xiaoyan Zhang) led the device concept and application framing, designed and fabricated the MARC device, performed the experiments, and carried out data processing and quantitative analysis. I drafted the original manuscript and coordinated revisions with co-authors. The numerical modelling/simulation reported in this chapter was performed by a co-author (Povilas Dumčius) and is included here to support the design interpretation and experimental findings rather than as my original modelling contribution.

3.1 Introduction

3.1.1 Background

Cell rotation is one of the most important techniques for cell manipulation in modern bioscience, as it not only permits cell observation from any arbitrary angle, but also simplifies the procedures for analyzing the mechanical properties of cells, characterizing cell physiology, and performing microsurgery.[84] Cell rotation typically refers to its rotational movement, often observed in organisms during their early development or in the context of cell migration and tissue morphogenesis.[158, 159, 160] Cell rotation under external forces provides opportunities to actively manipulate cells, which facilitates 3D cell imaging and allows observation from a designated angle. The rotational motion exhibited by cells under specific conditions, such as acoustic rotation, can serve as a label-free parameter for distinguishing different cell types and offering additional information about 3D cell morphology. For example, nuclear and cytoplasmic information including mitotic division have been better imaged for improving classification of suspended MCF-7 cells through multi-angle cell images.[161] A high-resolution 3D reconstruction of fluorescently labeled pollen grains was enabled by acoustic rotation to demonstrate and analyze their heterogeneous surface morphologies.[85] Refining the techniques that manipulate the rotational dynamics of cells can offer invaluable insights, expediting the analysis and differentiation of heterogeneous cells according to their rotational characteristics.

Acoustofluidic technology, which utilizes either surface acoustic waves (SAWs) or bulk acoustic waves (BAWs), has been increasingly applied in cell rotation applications. BAWs enabled rotation always rely on micro-bubbles (with bubble size typically chosen to be comparable to the device dimensions and the target object, often on the order of ~10–70 μm),[85, 86] micro-structures, and standing-wave superposition. Previously microbubble-based acoustic cell rotation technique has been developed for analyzing reproductive system pathologies and nervous system morphology in Caenorhabditis elegans.[86] A mode-switchable acoustofluidic device has achieved stable transportation, trapping, 3D rotation, and circular revolution of micro-objects.[140] Microbubble-based acoustofluidics commonly involves initiating microbubbles in the device before manipulation. Acoustofluidic techniques were also employed with oscillating microstructures to precisely rotate cells using acoustic microstreaming.[89, 90] BAW rotation can also be achieved via standing-wave superposition, in which two (or

more) orthogonal ultrasound modes are combined to create a time-varying pressure field (i.e., a rotating or re-orienting potential well) that generates an acoustic radiation torque and drives controlled rotation without microbubbles and without oscillating microstructures.[91, 92] For example, Schwarz et al. demonstrated contactless rotation of non-spherical microparticles by amplitude modulation of two orthogonal ultrasonic modes, enabling continuous rotation and the ability to stop at arbitrary angular positions.[92] SAWs travel along the surface of a substrate, creating nanoscale mechanical vibrations on the surface while experiencing minimal acoustic energy loss within a depth of one or two wavelengths below the surface.[103] Compared to BAWs, SAWs offer better manipulation resolution due to their higher operating frequency up to GHz ranges, and the SAW wavelengths are often comparable to or smaller than the size of typical cells, allowing for more precise control.[162, 163] Recently, SAWs-based techniques have been used for high-speed direct rotation of zebrafish larvae and C. elegans, facilitating multispectral imaging of these model organisms and their internal structures.[93, 94] However, although many of these acoustofluidic techniques can rotate a single trapped object in situ, they generally do not support parallel manipulation of many individual cells/particles while keeping each target separately trackable (i.e., individually identifiable/addressable), which results in limited throughput. Furthermore, when microbubbles are used, their quantity determines the number of cells captured and rotated. Larger cell populations necessitate longer microchannels to accommodate the physical size of each microbubble. Therefore, a rotation device with higher throughput but a smaller footprint is desired.

Cytopathology, an important branch of pathology, offers diagnostic information for diseases at the cellular level, and is commonly used to diagnose diseases including cancers, inflammatory conditions, and infections.[164] For example, prevention strategy of cervical cancer involves the collection of a small sample of cells from the cervix (by a smear test) for cytopathological examination to identify cells from cancer or its potential precursors.[165] Cells exfoliated from a suspicious lesion through smears, scrapings, brushings, and washings, play a crucial role in disease screening. These cells are meticulously collected and transferred onto glass slides for microscopic examination, which requires highly trained pathologists. The evaluation is focused on searching cytomorphological abnormal features such as nuclear/cytoplasmic area, nuclear-to-cytoplasmic (N/C) ratio, and nuclear irregularity.[166, 167] The percentage of

true negative pathological results (i.e., patients do not have the disease) in smears can vary significantly depending on multiple factors such as the type of smear, the population and quality of the sample, and the expertise of the pathologist. In many cases, the majority of smears in routine screenings for human papillomavirus (HPV) yield true negative results. For instance, 60% of HPV tests for women aged 20 to 24 in the UK return negative results.[168] Consequently, pre-screening methods that prioritise higher-risk specimens could streamline workflows and improve diagnostic efficiency by focusing expert review on cases most likely to require follow-up.

3.1.2 Design Rationale and Development Process

Informed by discussions with cytopathologists and direct observation of the clinical workflow from sample processing to slide review and reporting, the MARC device was developed to address two practical requirements for pre-cytopathological screening. First, routine screening includes a high proportion of true-negative cases, yet these still demand substantial review time from trained pathologists.[168, 169] A rapid pre-screening tool is therefore desirable to extract morphology-relevant information efficiently and prioritise cases that warrant further conventional examination. Second, key cytomorphological descriptors (e.g., nuclear shape and N/C ratio) can be viewpoint dependent for suspended cells; therefore, we hypothesised that acquiring multi-view images of the same cell at defined rotational angles could provide more comprehensive morphological information for cytopathologists, thereby supporting more reliable assessment than single-view imaging.[161] This motivated the development of a platform for controlled, multi-angle imaging of individually trackable cells.

These needs translated into specific design targets: (i) stable, controllable rotation of individual cells while preserving cell identity for tracking across viewing angles; (ii) parallel operation to increase throughput within a compact footprint; (iii) contact-free handling compatible with fragile bio-samples; and (iv) compatibility with standard microscopy and routine sample preparation. SAW-based acoustofluidics was selected because it enables contact-free actuation and can generate controllable pressure and streaming fields at cellular length scales, supporting both trapping and rotation. The final MARC architecture was established through iterative design–test cycles, in which the field configuration and chamber layout were refined to achieve two simultaneously addressable rows of rotating, individually trackable cells with repeatable operation.

Guided by these requirements, we present a device capable of performing multi-view acoustofluidic rotation cytometry (MARC) for pre-cytopathological screening to address limitations in throughput and individual target trackability in existing acoustic-rotation approaches, and to support efficient cytopathology workflows. MARC uses a designed acoustofluidic field to trap and rotate two rows of cells simultaneously, enabling higher-throughput multi-angle imaging while keeping each cell separately trackable. We apply MARC to hepatocyte cell lines Huh7 (cancer) and IHH (normal) and show that cytopathological assessment metrics, particularly the N/C ratio, are strongly influenced by viewing angle. Moreover, MARC improves sensitivity in distinguishing cancer and healthy cells compared with conventional slide-based evaluation, highlighting its potential to assist pathologists in improving screening efficiency and conserving clinical resources.

3.2 Results and Discussion

3.2.1 Working Mechanism and Experimental Setup

The MARC device was designed to actively induce cell rotation within the microchannel by establishing acoustic microstreaming around the cells. As shown in Fig. 3.1a, a pair of interdigital transducers (IDTs), powered by radio frequency (RF) signals, generate identical SAWs that travel in opposite directions, effectively forming standing SAWs (SSAWs) (Fig. 3.1b). The SSAWs exhibit a series of locations at which their amplitudes are zero or maximum, and these locations are pressure nodes (PNs) or pressure antinodes, respectively. The SAWs meet the fluid in the microchannel and leak their energy into the fluid exerting leaky acoustic waves. Generally any particles that are placed in the acoustofluidic field experience both acoustic radiation force ($\boldsymbol{F}_{rad}$) and streaming induced drag force ($\boldsymbol{F}_{drag}$) as already been detailed stated in chapter 2. The ratio of two forces can be calculated:

$$\frac{\boldsymbol{F}_{rad}}{\boldsymbol{F}_{drag}} = \left(\frac{\pi P_0^2 V_p \beta_l \varphi(\beta,\rho) sin(2\kappa x)}{12\lambda\pi\eta R_p \boldsymbol{v}}\right) \tag{3.1}$$

Properties of the particles such as their size, density, and compressibility, determine the above force ratio. For particles with $\frac{\boldsymbol{F}_{rad}}{\boldsymbol{F}_{drag}} > 1$, the radiation force is dominant and they are attracted toward the PN. Whereas when $\frac{\boldsymbol{F}_{rad}}{\boldsymbol{F}_{drag}} < 1$, the acoustic streaming is dominant and the particles are dragged to flow through micro-circulation. It is noted

that when $\frac{\boldsymbol{F}_{rad}}{\boldsymbol{F}_{drag}} = 1$, particles are at equilibrium around the PNs, where the radiation force on a particle is balanced against the streaming force. In the MARC SSAWs field, the pressure nodes define two trapping lines (rows). Because the acoustic radiation force scales with cell size and acoustic contrast (effective cell density/compressibility relative to the medium), cells are driven toward these nodes with cell-dependent trapping strength and migration dynamics. Near the node, the associated acoustic microstreaming produces a local shear flow that exerts a torque on the trapped cells, driving rotation.[86] This rotation is beneficial for thoroughly scanning the cells to capture their multi-angle morphology while maintaining a constant microscope focus. The MARC device can simultaneously attract cells using the radiation force and rotate them with microstreaming vortices, without the need using various microstructures such as air bubbles or sharp edges.

The MARC diagnosis process unfolds as follows (Fig. 3.1c). By loading the cell sample into the microchannel and then activating with the SAWs, the cells will be trapped into two traces and rotated in the opposite directions. The rotational motions of the cells cause their morphological features exposed at multiple angles of observations, facilitating the characterization of multiple cellular properties corresponding to cellular status, chemical composition, or physical features. Owing to the multi-angle images of the single cell during rotation, a more comprehensive cytopathological evaluation can be attained, potentially offering additional insights into cellular abnormalities and enhancing diagnostic assessment.

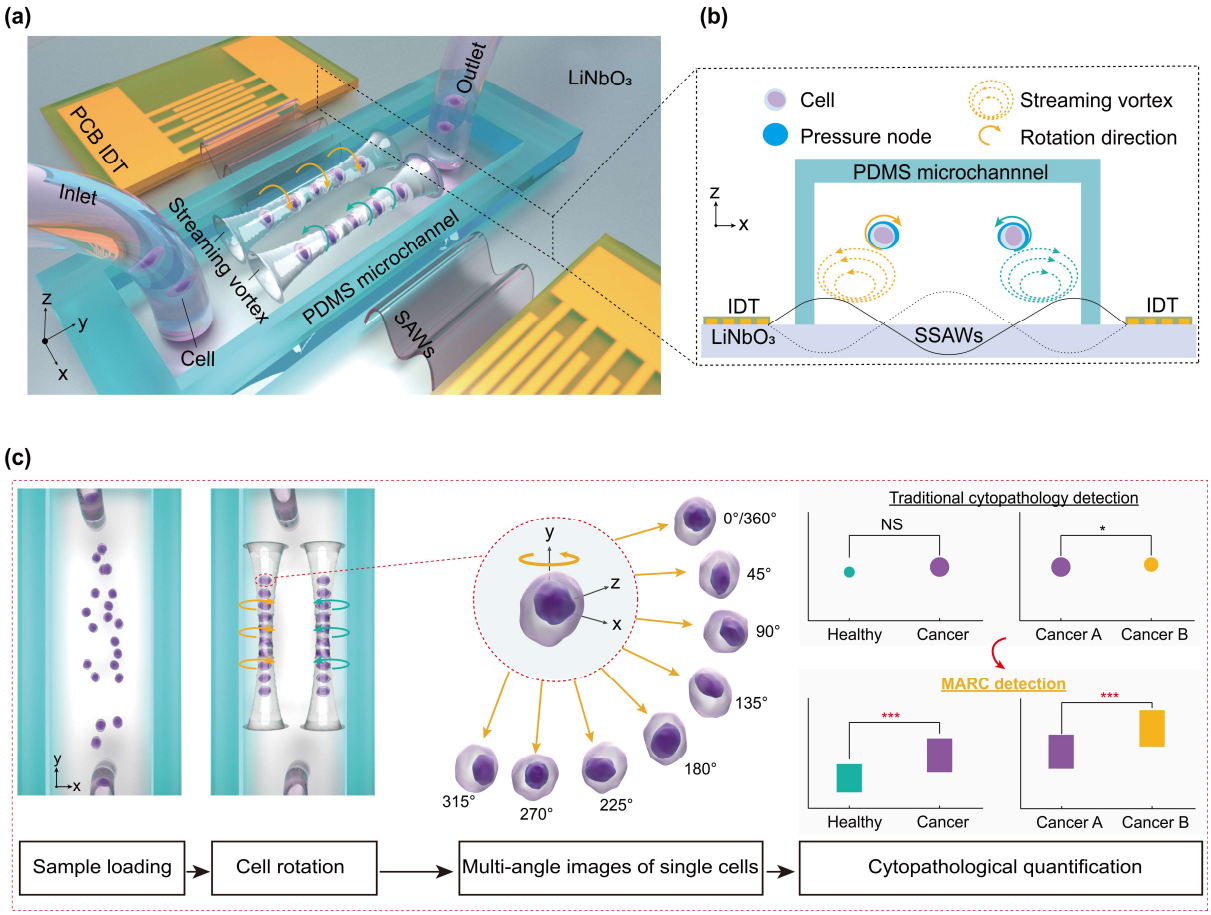

Figure 3.1. Working mechanism illustration of MARC system. (a) Illustration of the MARC device, which comprises two identical printed circuit board-based interdigital transducers (PCB-IDTs) for producing surface acoustic waves (SAWs) and a polydimethylsiloxane (PDMS) microchannel with an inlet and an outlet for cell loading. (b) SAW-induced radiation force and microstreaming are responsible for trapping and rotating the cells, respectively. The two PCB-IDTs generate two counter-propagating SAWs to form a standing SAW (SSAW) yielding two pressure nodes (PNs) within the microchannel, which trap the dispersed cells to form two traces. Meanwhile, streaming vortexes produced in the microchannel drive the trapped cells to rotate opposite the streaming vortexes. (c) Flow chart of the working mechanism of the MARC system.

The setup of the MARC device is shown in Fig. 3.2. The device is driven by the powered RF signals, with both incident and reflected power being monitored using two power meters. An impedance matching network is used to mitigate the impedance mismatch between the printed circuit board (PCB)-based IDTs and an RF power amplifier.[170] The technique for constructing and testing the PCB-based IDTs has been previously introduced for various applications.[54, 57, 64, 171, 172] A syringe pump is used to

introduce the cell sample into the MARC device. A microscope and camera system capture sequential images, providing a rotational descriptor of the cells.

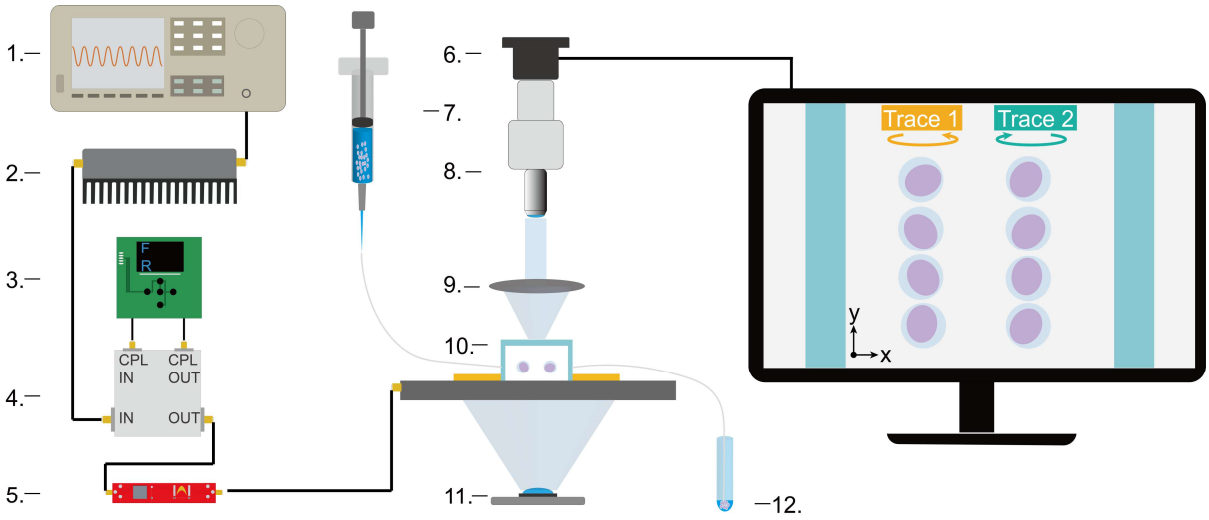

1. Signal generator
2. RF power amplfier
3. Power meter
4. Coupler
5. Matching network
6. Camera
7. Syringe pump
8. Microscope
9. Polarizer
10. MARC
11. Light
12. Waste

Figure 3.2. Schematic illustration of the MARC system setup.

3.2.2 Optimization of Acoustofluidic Rotation

The MARC device was optimized to effectively trap the cells at the PNs for acoustic rotation driven by the induced streaming vortexes (Fig. 3.1b). It is crucial to establish a precise and symmetric streaming vortex within the microchannel to enable simultaneous manipulation of both traces of cells. This allows for capturing the morphology of multiple cells from multiple angles simultaneously. To achieve this, the channel dimensions and acoustofluidic parameters were first studied numerically to optimize the design. The width and height of the microchannel were swept from $\frac{\lambda}{2}$ to λ ($\lambda \approx 200$ μm), and from $\frac{\lambda}{5}$ to $\frac{\lambda}{2}$, respectively. This range was chosen to accommodate two symmetric PNs formed along the x-axis within the microchannel. Fig. 3.3a shows the simulation result of the maximum acoustic pressure in association with the height and width of microchannels. It is observed that a more consistent maximum acoustic pressure across different microchannel heights is achieved at a channel width of approximately 200 μm (cyan curve). This specific channel width was

then chosen for further numerical analysis aimed to determine the optimal channel height.

The simulated acoustic pressure and fluid streaming patterns for four-channel heights, including 100, 80, 60, and 40 μm, are plotted in Figs. 3.3b-c, showing maximum acoustic pressure of 309, 349, 345, and 319 kPa, respectively. Channel heights of 100 and 80 μm were not selected due to the presence of additional unwanted PNs near the top of the channel, as indicated by the black-outlined blue oval regions, which are likely to trap cells against the channel wall. The channel height of 40 μm was not used either, as the fluid streaming around the PNs exhibits identical intensities but in the opposite directions, which would cancel out the cell rotation.

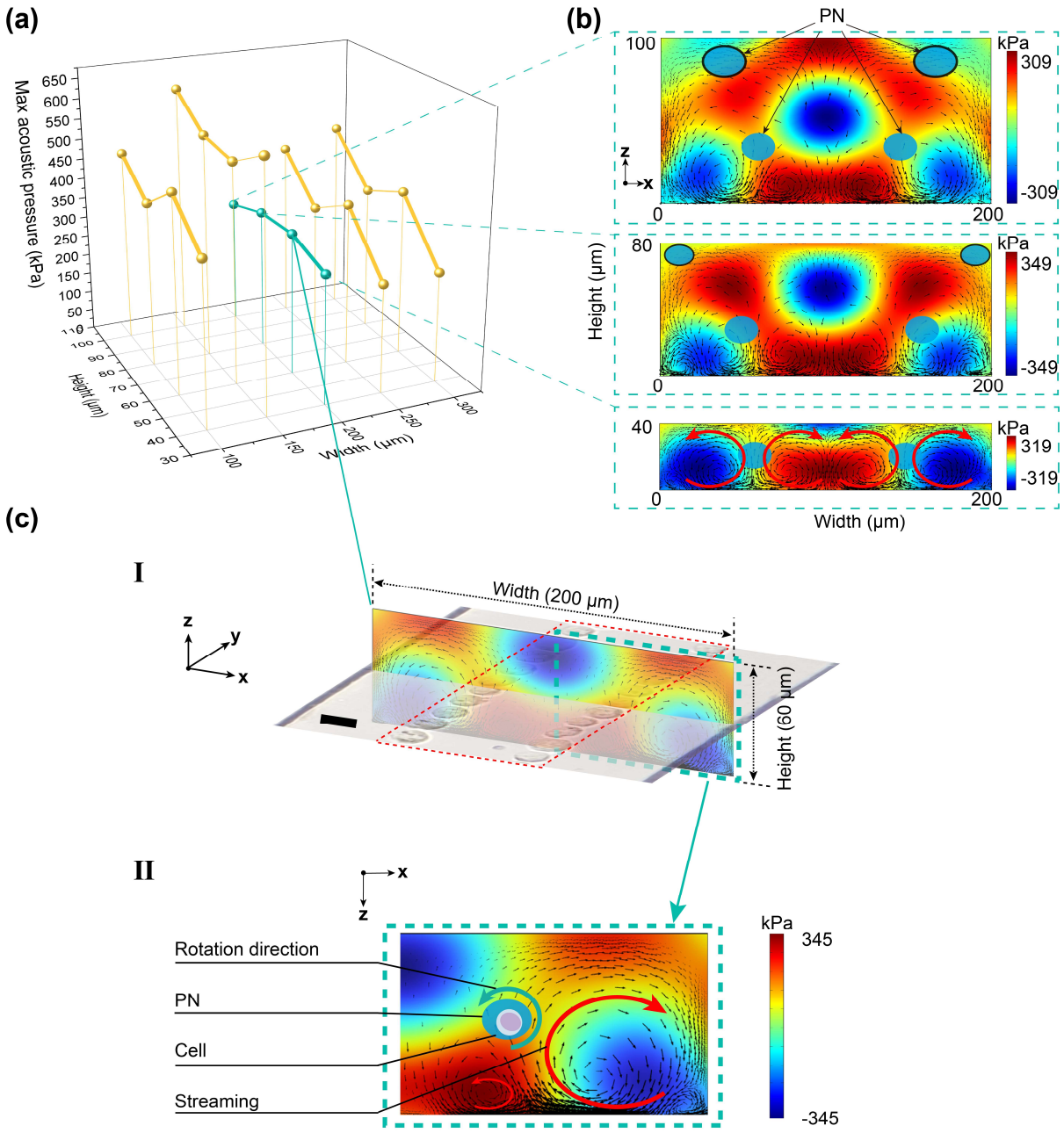

Figure 3.3. Numerical simulation (COMSOL Multiphysics 6.0) of various microchannel dimensions and acoustic field in the cross-section of the microchannel. (a) The sweep of the maximum acoustic pressure against the dimensions of the height and width of the microchannel. (b) The acoustic pressure and streaming pattern for the three different channel heights with the same channel width of 200 μm. The PN is indicated by the blue oval, and the acoustic streaming direction is indicated by the black arrows. (c.I) The acoustic pressure and streaming pattern for the dimension of 60 μm (height) 200 μm (width), which indicates two PN formed within the microchannel. Two cell traces formation after SAW excitation shows a good agreement with the two PNs. (c.II) The zoom-in simulation of the half microchannel

dimension indicates the formation of streaming vortexes around the PN. The coexistence of the PN and streaming will lead to cell rotation in situ along the PN. The red arrows indicate the direction of regional streaming vortexes. Scale bar, 20 μm.

The channel height of 60 μm denotes a favorable balance between the PN pattern and streaming dynamics, as shown in Fig. 3.3c. This configuration yields a symmetric distribution of PN within the MARC device, effectively trapping cells to form two distinct traces for microscopic imaging (Fig. 3.3c.I). The half microchannel part simulation result is shown in Fig. 3.3c.II, where the lateral streaming vortex displays a larger streaming velocity, leading to the in-situ cell rotation. While small experimental offsets may occur (e.g., due to fabrication tolerances or cell height variation), the observed two-trace trapping pattern is consistent with the simulated two-PN topology under the same operating condition. The generation of SSAWs was simulated under the condition which both IDTs were driven by the RF signals with the same phase ($\Delta\varphi = 0°$). To further investigate the influence of phase difference, we applied various phase differences between the two IDTs, as shown in Fig. 3.4. When applying a 90° phase difference ($\Delta\varphi = 90°$), asymmetrical acoustic patterns form within the microchannel. When applying a 180° phase difference ($\Delta\varphi = 180°$), although a PN is located at the center of the microchannel, the streaming flows around the PN counteract each other, negating the possibility of in situ cell rotation.

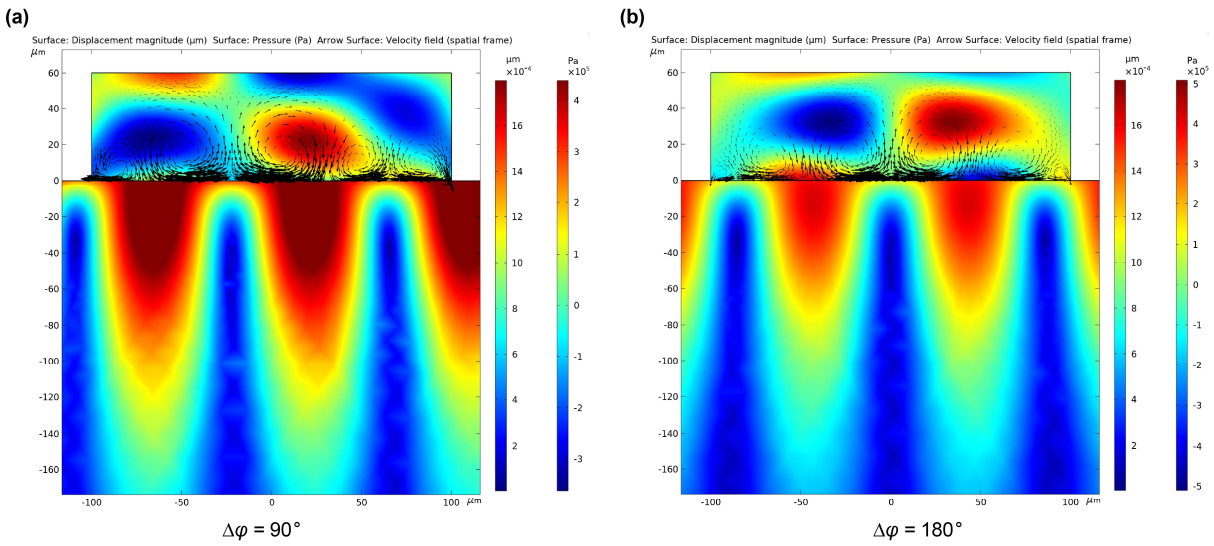

Figure 3.4. Numerical simulation of applying phase difference between the two IDTs at (a) 90° ($\Delta\boldsymbol{\varphi} = \mathbf{90}^{\circ}$), and (b) 180° ($\Delta\boldsymbol{\varphi} = \mathbf{180}^{\circ}$).

Compared with microbubble-based acoustic rotation techniques, the MARC device overcomes the issue of temporal instability of the microbubble within the channel[173] and does not require a pretreatment process before the sample loading. Additionally, cells can be accurately trapped by the two PNs located at the defined regions inside the microchannel, ensuring active and contactless manipulation of cells. This arrangement greatly enhances the convenience for multi-angle observation.

3.2.3 High-Throughput Cell Rotation

The acoustic rotation of the cells within the MARC device was tested using two types of liver cell lines, i.e., Huh7 (cancer) and IHH (normal). To test the hypothesis that MARC can register more cellular morphology parameters, such as the number of nuclei, cell area, and cell circularity, without the need for cell staining, unstained cell samples were introduced to the MARC device resulting in an initially even dispersion in the microchannel (Fig. 3.5a, left). Upon applying RF signals to the MARC device, the acoustofluidic field is activated, exhibiting immediate trapping of cells at the two PNs (Fig. 3.5a, right). The development of two traces of cells, where individual cells lined up end-to-end forming a continuous chain with no spaces between adjacent cells, significantly enhances the cell density within microfluidics. This setup positions cells at defined locations close to PNs, allowing efficient tracing rotating cells for high-throughput multi-view cytopathology.

The cells were rotated immediately after being trapped at the PNs, as illustrated in Fig. 3.5b. Both traces of the cells were rotated stably near the PNs owing to the acoustic trapping effect. The microstreaming induced in opposite directions and symmetrically to the channel center leads to clockwise and counterclockwise cell rotations. Multi-view images of each single cell, captured at different time stamps, offer highly informative morphology, revealing physical features and chemical composition at the single-cell level. It is worth noting that the field of view captured in the experiment corresponds to the highlighted region (red dotted line boxes) in the simulation given in Fig. 3.3c.I, where two traces of the cells rotate in opposite directions.

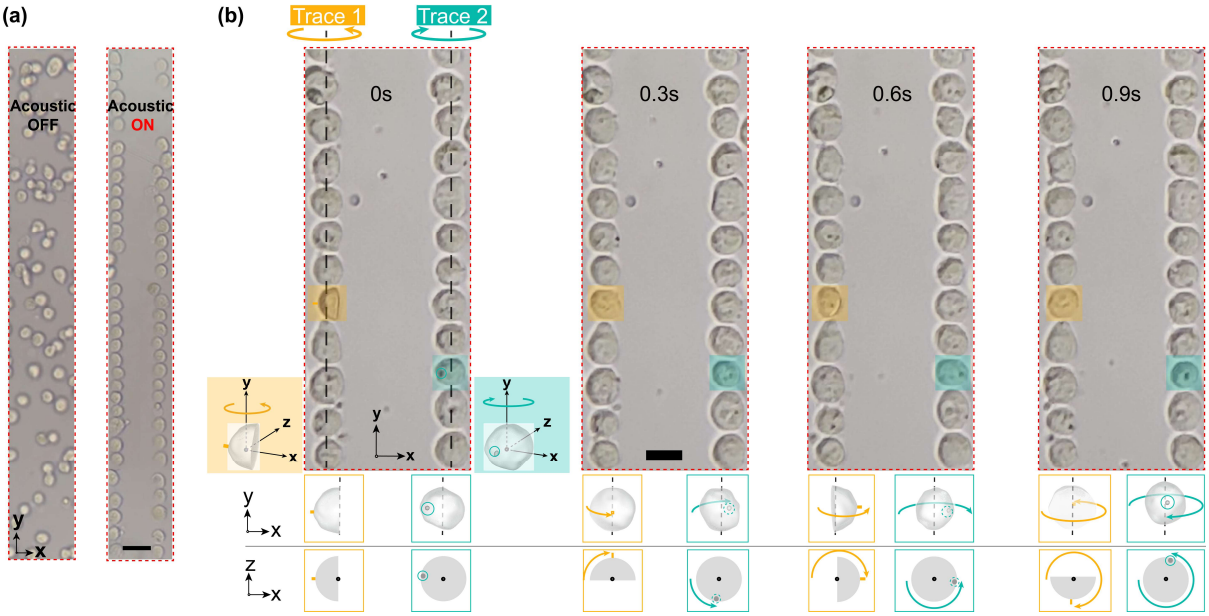

Figure 3.5. High-throughput cell rotation manipulation. (a) Cells are trapped at the two PNs to form two traces of cells when the SAW is ON, which soon to rotate in situ. The red dashed box represents the cell rotation observation field. (b) All the cells in the two traces are rotating driven by the surrounding acoustic streaming. Scale bars in (a–b) are 50 μm, 20 μm, respectively.

Multi-view cellular morphology, accessible through rotation, may provide more comprehensive information to aid cytomorphology investigations. Sequential images of cells, taken at intervals ranged from 0.1 s to 0.15 s, are shown in Fig. 3.6, in which the dual nucleoli (indicated by blue arrows) are identified at 0.1, 0.2, 0.5, 0.8, and 0.9 s for Huh7-#1 (Fig. 3.6a) but are not visible in other views. Cell morphology varies with the observation angle, including nucleolar number, cell area, and cell circularity, all of which change during rotation (Figs. 3.6b-d). For example, the shape of cell Huh7-#2 (outlined in black) changes from oval (0.6 s) to circular (0.9 s) at different observation angles. For the IHH cell sample shown in Fig. 3.6e, the intermittent appearance of the nucleus during the rotation can be clearly identified without nucleus staining (indicated by red arrows). In addition, as shown in Figs. 3.6f-h, notable variations in the nucleus outline, cell area, and cell circularity can be clearly observed during rotation. For instance, the cell area changes by 20% from 0.3 to 1.2 s for IHH-#1. Such changes are also found in another studies using magnetic resonance imaging (MRI) to analyze cell morphology.[174, 175] The cell area is used as a key parameter to evaluate cell evolution, e.g., a 10.5% cell area loss was found in 50 days senescent erythrocytes.[176]

Additionally, cell circularity is another crucial parameter to evaluate cellular physiology state, e.g., response to drugs and other external materials. The circularity of IHH-#2 cells changes by 18% from 0.15 to 0.6 s as shown in Fig.3.6e. A circularity reduction of 19.6%, from 0.903 to 0.726, is registered when HepG2 cells expose to 5% squaramide-based supramolecular materials.[177] The ability to detect cell area and circularity holds significant potential for advancing our understanding of cellular physiological processes.

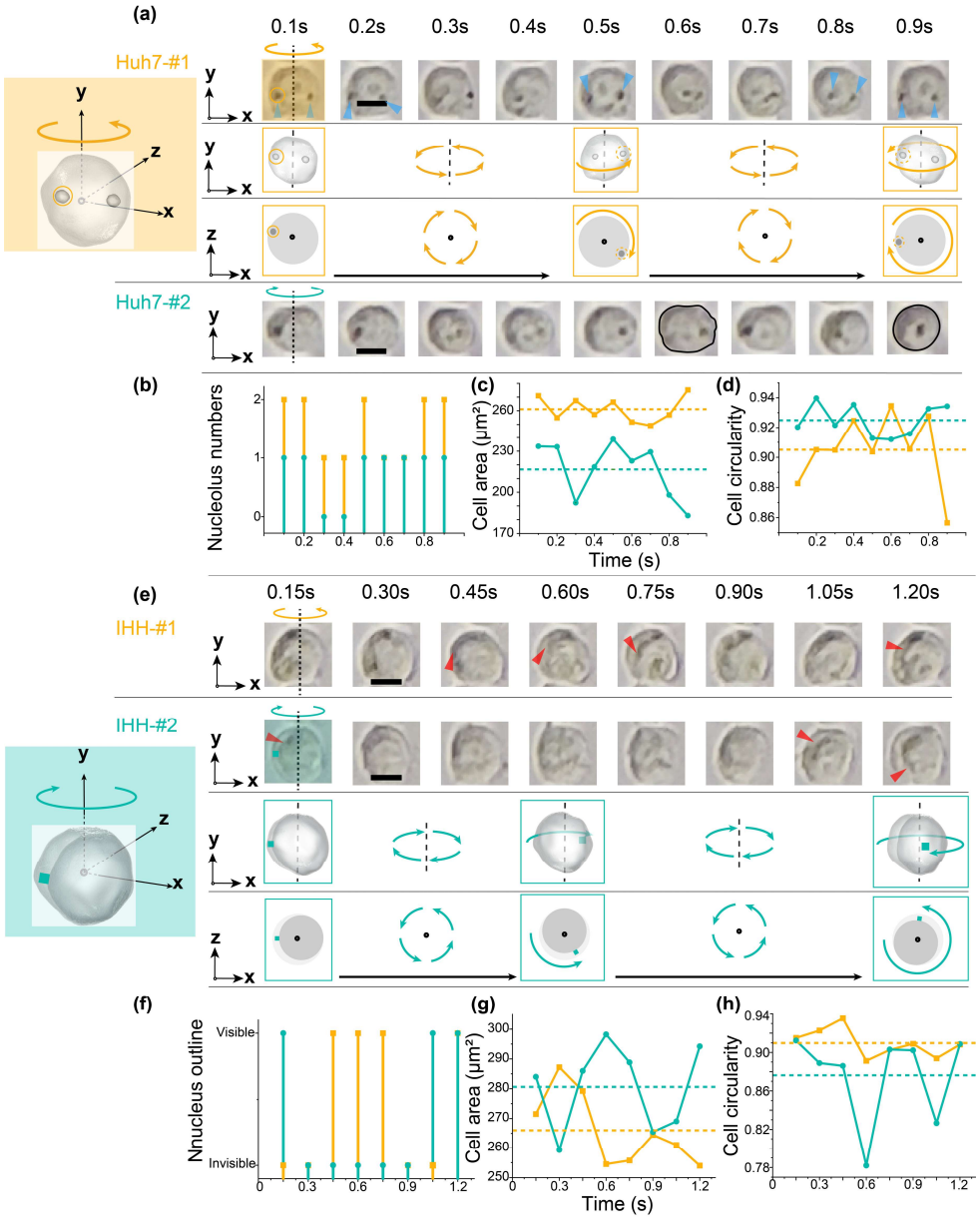

Figure 3.6. Examples of Huh7 and IHH cells during rotation. (a)-(d): Examples of Huh7 (hepatocyte cancer line) cells during rotation. The morphology parameters including the nucleolus number, cell area, and cell circularity are changing during the

rotation. (e)-(h): Example of IHH (hepatocyte cancer line) cells during rotation. The morphology parameters including the nucleus outline visibility, cell area, and cell circularity are varying during the rotation. (c), (d), (g), (h): Quantification of cell area and cell circularity during rotation process of Huh7 and IHH cell lines, respectively. Note: the area and circularity traces were obtained by frame-by-frame measurements in ImageJ after interactive ROI/outline selection (i.e., semi-manual segmentation rather than fully automated analysis). The dashed lines represent the average value of the cell area and cell circularity, which is calculated based on the sum of each time-interval quantification for the total rotation process. Scale bars are 10 μm .

The examples of cell morphology captured during rotation demonstrate that the MARC device successfully symmetrically trapped and rotated two traces of cells. The discovery of inconsistencies in nucleolar number, cell area, circularity, and nuclear outline within a single cell preliminarily proved the value of using MARC for multi-angle cytology. We further applied the MARC device to compare the circularity between Huh7 and IHH cells during rotation. As shown in Fig. 3.7a, no significant difference (*NS*) in circularity is observed at angles of 135, 225, 270, and 360 degrees. Whereas a significant difference in circularity ($p < 0.0001$) is detected between these two cell types (Fig. 3.7b). This demonstrates that MARC considerably enhances the discrimination between the cancer and normal tissue cells.

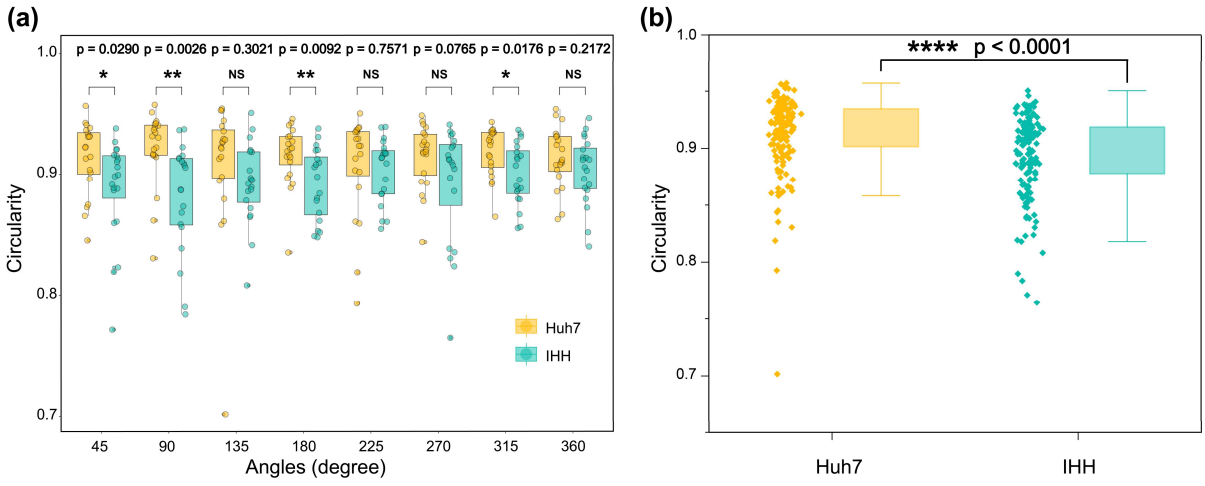

Figure 3.7. Cell circularity comparison between Huh7 cells and IHH cells under different observation angles during rotation. (a) At each single angle comparison. (b) Rotation-based multi-angle integrated cell circularity comparison. All p-values were

determined using one-way ANOVA. *NS*: no significance. * $p < 0.05$, ** $p < 0.01$, **** $p < 0.001$.

The throughput of the current study is calculated using the formula:

$$Throughput = \frac{N}{RA \times \frac{1}{FPS}} \tag{3.2}$$

Where *N* is the maximum number of cells observed in the microscope window, FPS is the camera frame rate, and RA is the number of rotation angles captured during cell rotation. In this study, *N* was approximately 50, as observed with a 20× objective lens. FPS was 30 for the camera used to validate the concept. RA was 8, as eight angles were captured during cell rotation for morphological quantification. Therefore, the throughput was estimated as:

$$\frac{N}{RA \times \frac{1}{FPS}} = \frac{50}{8 \times \frac{1}{30}} = 188\ cells/s \tag{3.3}$$

The throughput can be increased by using cameras with higher frame rates. For instance, a camera with 1000 fps could achieve a throughput of 6250 cells/s, approaching the capacities of imaging flow cytometry. In comparison, traditional pathology slide scanners have a throughput of about 2 min per slide, excluding slide preparation time, and can scan approximately 150,000 cells per slide.[178] This corresponds to an estimated throughput of 1,250 cells/s. However, considering the preparation steps such as fixation, embedding, sectioning, staining, mounting, and labelling-which can take more than 24 h—the actual throughput of traditional pathology examinations might be lower than that achieved with MARC.[161, 179] The MARC device also exhibited a much higher throughput compared to other acoustic rotation methods using microbubbles.[85, 88] Assuming both MARC and other methods operate at the same rotation speed, the time required to capture a 360° morphology is the same. The throughput is defined by the number of cells being rotated and captured within a microscope's field of view, which is determined by the magnification used. For instance, a 20× objective lens can visualize approximately 50 cells in the field of view accommodated in the MARC device, whereas most devices applying microbubbles contain only five cells. In addition, the MARC has the capacity to attract and rotate more than two cell traces by widening the channel to accommodate more PNs,

resulting in the throughput at least 10 times larger than that of microbubble methods. This higher throughput is due to the MARC device's elimination of microstructures inside the channel, allowing for a higher cell density during rotation.

3.2.4 Controllable Cell Rotation

The velocity of the acoustic streaming determines the rotational speed of the cells. The amplitude of the streaming velocity was controlled by the amplitude of the RF signal applied to the MARC device. The control of this speed allows capturing multi-view morphology using the imaging system with various frame rates. Fig. 3.8 compares the measured rotational speed of cells (revolutions per minute, r.p.m.) from two representative rotation traces with the simulated acoustic-streaming velocity, both plotted against the peak-to-peak voltage applied to the MARC device. Note that the rotation speed is quantified from top-view trajectories in the $x-y$ plane, whereas the simulated streaming velocity is extracted from a cross-section ($x-z$ plane); therefore, the axes used for experiment and simulation are defined differently and are not directly comparable. The purpose of this figure is to demonstrate that the model reproduces the experimentally observed trend: increasing the RF drive amplitude increases the streaming strength and, correspondingly, increases the cell rotation speed. For example, increasing the amplitude from 7.5 V_{pp} to 17.5 V_{pp} results in an increase in rotational speed from $\approx$5.2 to $\approx$55 r.p.m. Within the tested range (up to ~55 r.p.m.), we did not observe obvious rotation-speed-induced deformation; the apparent changes in cell outline (area/circularity) primarily reflect different 2D projections at different viewing angles during rotation.

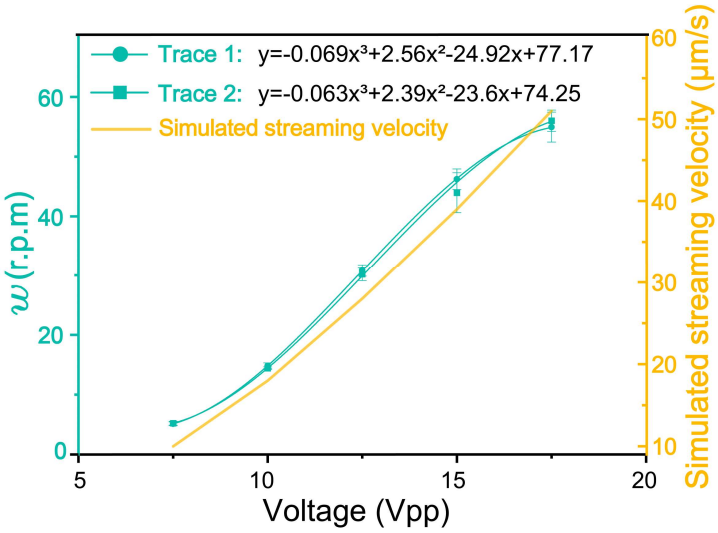

Figure 3.8. Cell rotation velocity and simulated streaming velocity quantification between two cell traces under various input voltage (*n* = 15). Note: rotation is quantified from top-view $x-y$ trajectories, whereas streaming is extracted from an $x-z$ cross-section in simulation; thus the axes differ, and the aim is to show that the model predicts the correct experimental trend with increasing drive amplitude

The statistical comparison data of two cell traces are listed in Table 3.1. These results show that symmetric cell rotation with similar rotational speeds is created in the MARC device. As expected, the rotation angle can be predicted by using the time as their linear relationship shown in Fig. 3.9.

Table 3.1. The measured rotational speed of Huh cells against the amplitude of the input signal from 7.5 Vpp to 17.5 Vpp.

Input voltage (V_{pp})	Cell rotation angular velocity (r.p.m., revolutions per minute)						*p* values of statistical analysis between trace 1 and trace 2. (*NS*: no significance, $p > 0.05$)
	Cell trace 1			Cell trace 2			
	Mean	SD	*n*	Mean	SD	*n*	
7.5	5.13333	0.73568	15	5.23333	0.74141	15	0.77 (*NS*)
10	14.8406	0.1327	15	14.43242	0.06562	15	0.33 (*NS*)
12.5	30.84364	0.06136	15	30.16413	0.07201	15	0.54 (*NS*)
15	46.21856	0.04907	15	43.96559	0.09915	15	0.44 (*NS*)
17.5	54.94048	0.05152	15	56.01462	0.03356	15	0.65 (*NS*)

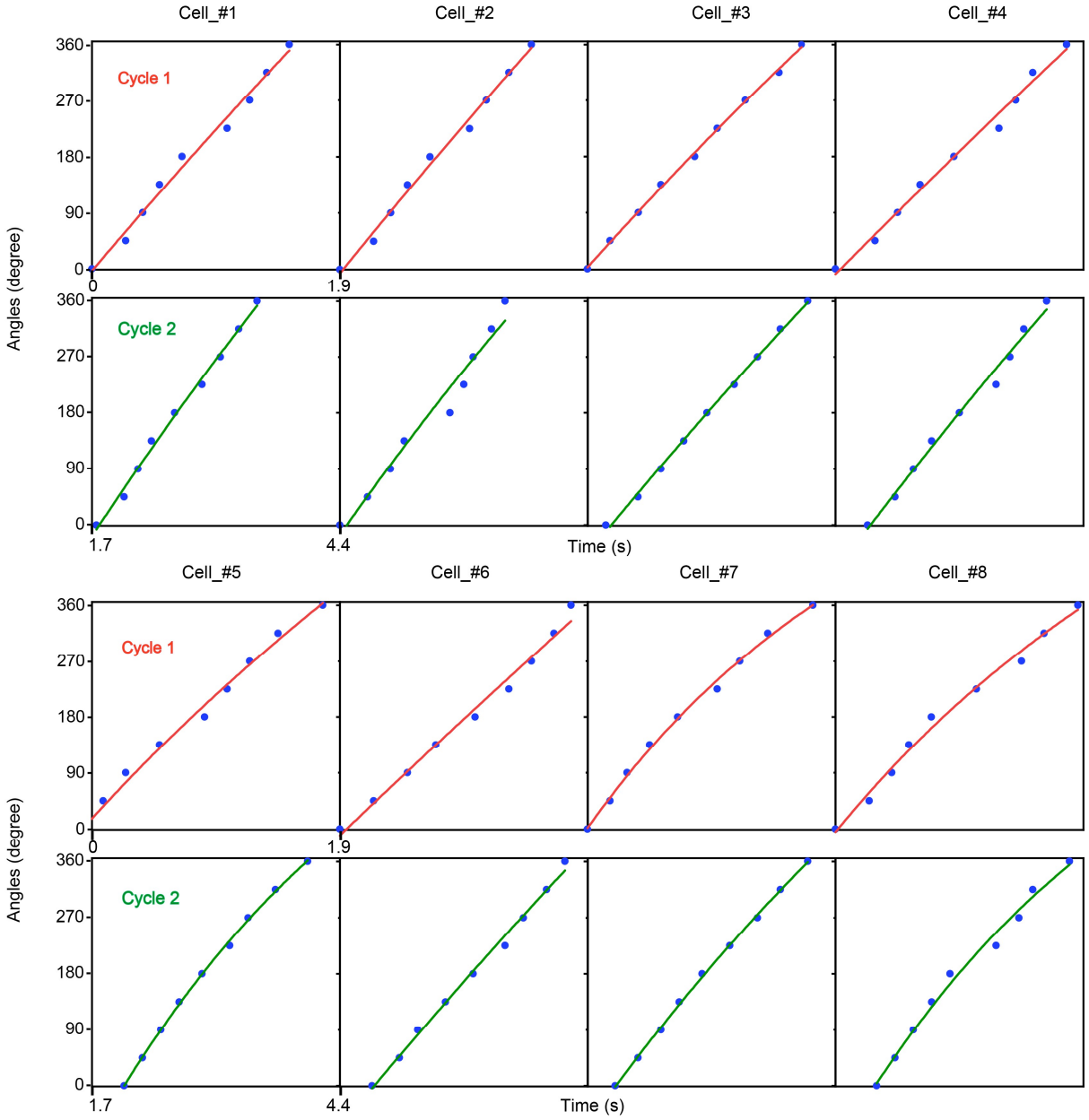

Figure 3.9. Rotation angle quantification of the Huh7 cell (*n* = 8) during two rotation cycles (i.e., two times 360 degree) under 12.5 Vpp.

The contactless feature of MARC facilitates the cell rotation taking place in a free space inside the microchannel. However, the potential cell position offset during rotational is crucial for achieving stable image capture (Fig. 3.10a), which is strongly influenced by the amplitude of the RF input signal. We therefore measured the cell shift under the input signals ranging from 12.5 to 17.5 V_{pp}. As shown in Figs. 3.10b-c, the cells on both traces drift off their starting positions for only a few microns. The average drifts under the three input signals range from $\approx$0.6 to $\approx$1.2 μm, and from 0.5 to 1 μm, respectively, on the x-axis for both traces. These values indicate the

minimal lateral displacements during the rotation due to the streaming effects. Similarly, the cell drift on the y-axis ranges from ≈1.0 to ≈2.6 μm, and from 1.2 to 2.5 μm, respectively. While the cell displacement offset shows minimal position drift during rotation, the two cell traces exhibit inconsistent responses to input voltages along the x- and y-axes. This inconsistency may stem from small out-of-plane (z-direction) deviations, i.e., the cell's height within the channel is not completely stable during rotation; when cell positions are extracted from a top-view ($x-y$ plane) image, any z-motion can introduce small apparent $x-y$ measurement errors.

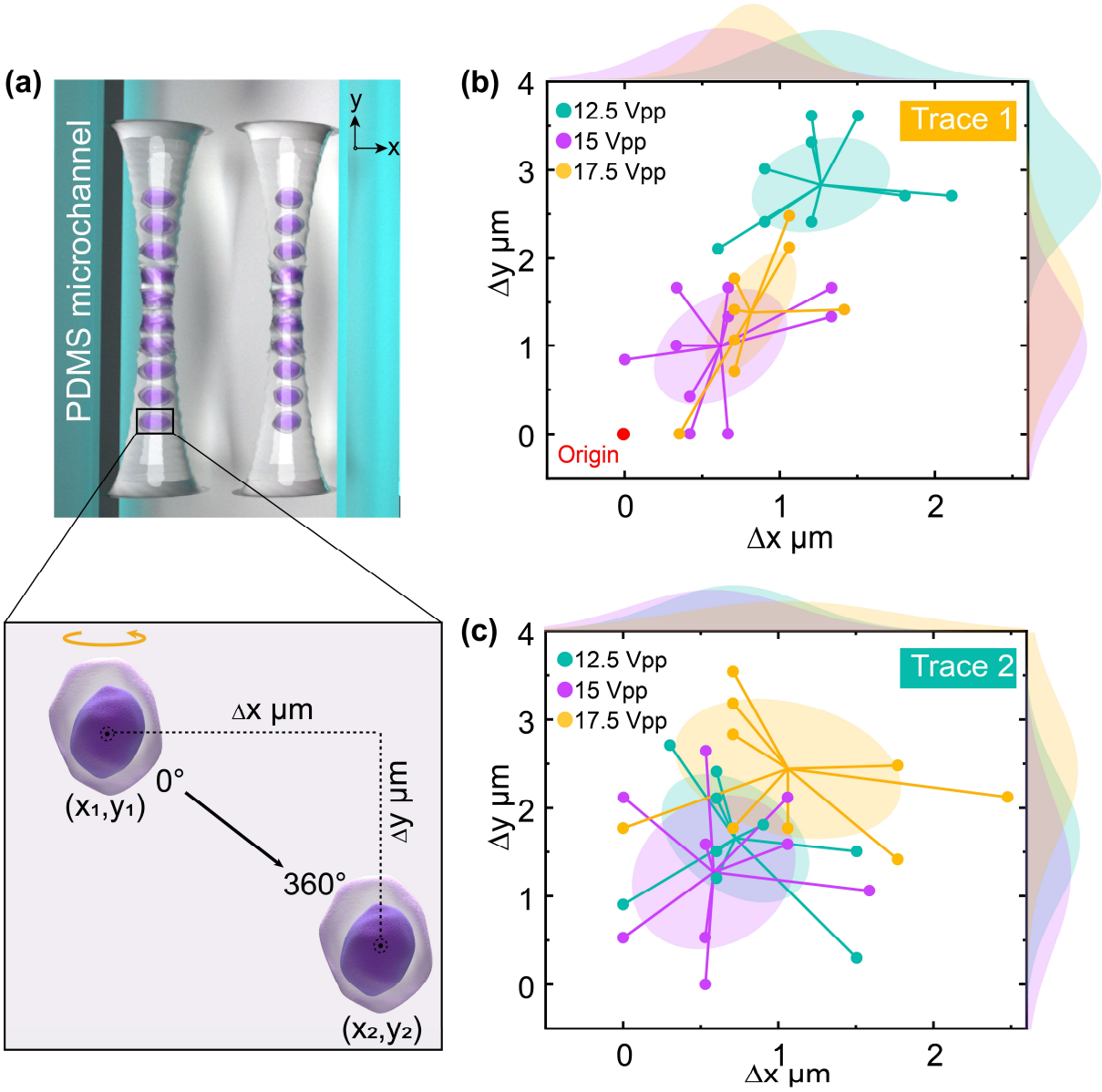

Figure 3.10. Cell shift quantification along x and y-axis during rotation process for both cell traces. (a) Illustration of the cell displacement on the x- and y-axes. (b)-(c) Distribution of the cell shift on the x- and y-axis for both cell traces (n = 30).

Further analysis comparing the offset values reveals a significant variation between the two traces under 12.5 V_{pp} on both axes and 17.5 V_{pp} on the y-axis (Fig. 3.11). The variation at 12.5 V_{pp} may be attributed to a weaker acoustic radiation force in trapping the cells, whereas the use of 17.5 V_{pp} may produce unstable acoustic streaming to drive the rotation. To ensure minimal cell displacement in situ, an input signal of 15 V_{pp} was used in the following manipulation, as it produced in no obvious cell drift. In comparison to optically induced and metal-electrode-based dielectrophoresis methods, MARC can achieve in-situ rotation manipulation of multiple cells with minimal position drift during rotation. This feature allows imaging a group of cells without changing microscopic focus, which is crucial when using high magnification for high-throughput cytomorphological evaluation.

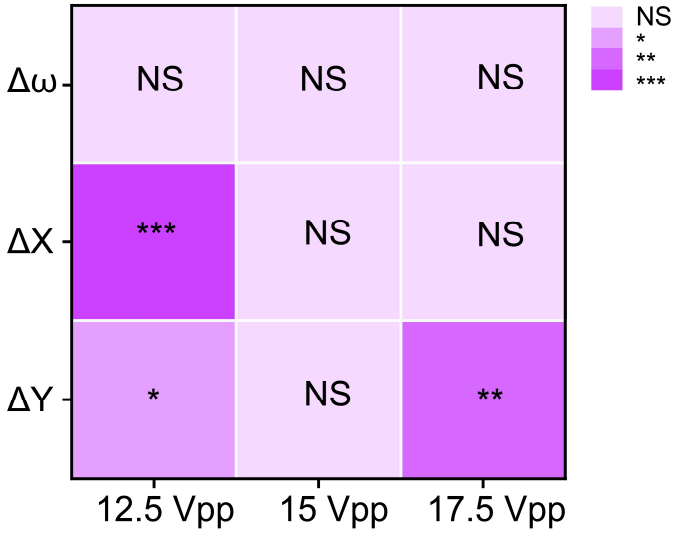

Figure 3.11. Quantification of the rotation variation between cell trace 1 and trace 2 under three input voltages. All *p*-values were determined using one-way ANOVA. *NS*: no significance. * $p < 0.05$, ** $p < 0.01$, *** $p < 0.001$.

3.2.5 Cytomorphological Evaluation during Cell Rotation

Cytomorphological evaluation was conducted using parameters including nucleus solidity, circularity, and N/C ratio, with their definitions illustrated in Fig. 3.12a. It is expected that these parameters exhibit variations when measured at different angles for a given cell. To investigate the utility of the additional morphology information during rotation, the captured multi-views of the cell were split into eight representative frames with an interval of 45°, with an example shown in Fig. 3.12b. In this example,

the nuclear morphology displays considerably different roundness, e.g., the nucleus appears rounder at 360° compared to 135° (highlighted by the cyan outline).

We further conducted a detailed analysis of three nucleus parameters of 30 individual Huh7 cells during rotation. Each cell was quantified at eight distinct rotation angles, separated by an interval of 45°. These 30 cells were then combined to form a single group, again analyzed at the same eight rotation angles. Our analysis revealed prevalent inconsistencies in value ranges across all parameters during the group cell rotation (as shown in Fig. 3.12c). Delving into the specifics, the solidity parameter exhibits the most substantial variation at 315°, ranging from 0.75 to 0.97. This variation suggests a broad spectrum from pronounced nucleus branching to minimal nucleus invagination. The circularity parameter, on the other hand, has its widest value which is dominant at the angle of 45°, oscillating between 0.47 and 0.95. Such a range indicates variations from highly irregular nucleus shapes to more rounded forms. Finally, the N/C ratio, a critical metric in pathology, shows marked fluctuations at angle 360°, with values ranging from 0.37 to 0.94. A high N/C ratio often indicates cellular atypia or malignancy, underscoring the importance of precise assessments.[180] Inconsistencies in these measurements from different observation angles, as identified through MARC, can potentially impact diagnostic outcomes.

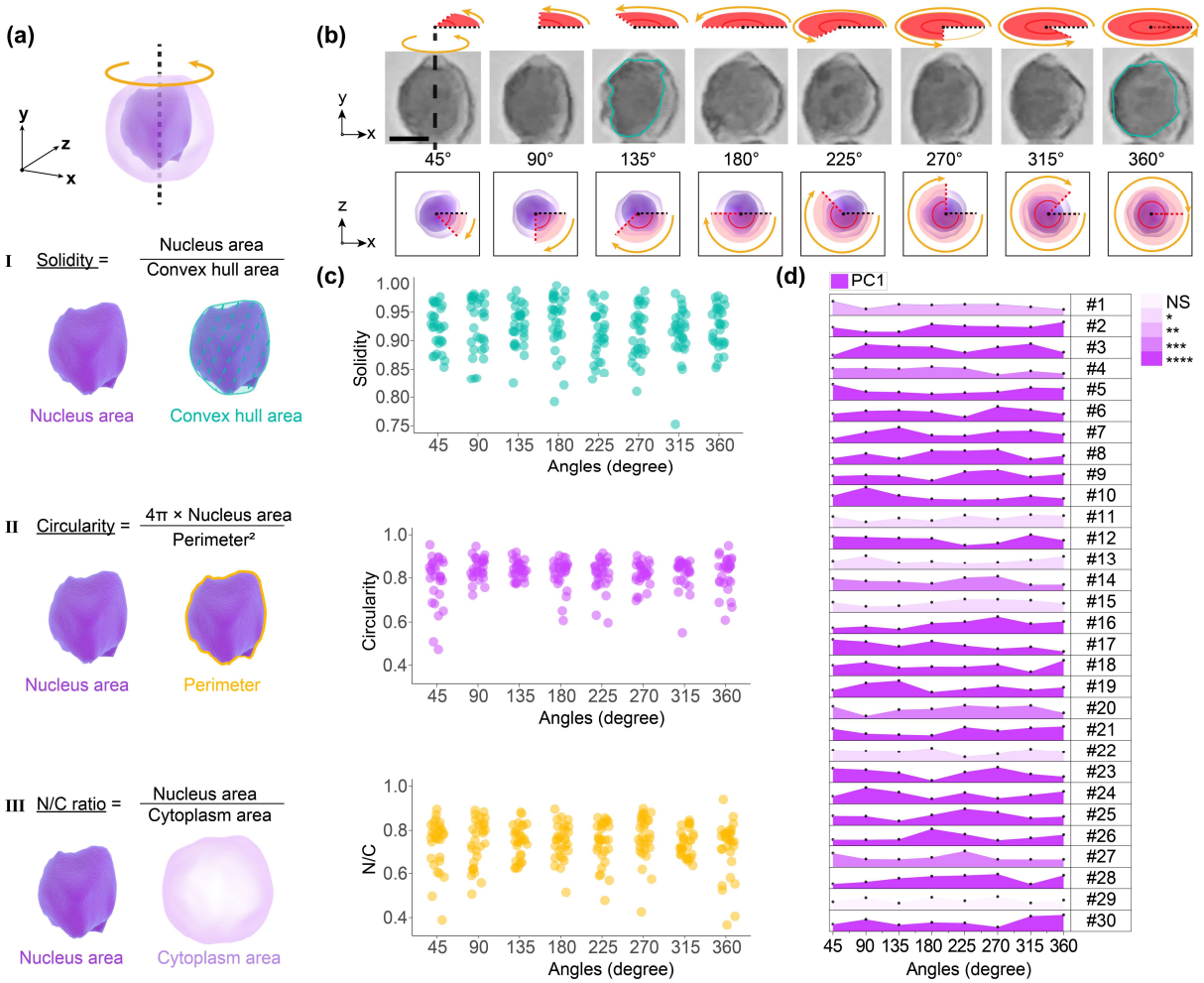

Figure 3.12. Cytopathological evaluation in the cell rotation process. (a) I – III: Definition of three commonly used nuclear morphology parameters: solidity, circularity, and N/C ratio. (b) Eight representative observation angle of a single hematoxylin-stained Huh7 cell. (c) Quantification of the three nuclear parameters for the Huh7 cell group (n = 30). (d) PCA analysis of the nuclear morphology variation under different observation angles for the Huh7 cells (n = 30). All p-values were determined using one-way ANOVA (normally distributed) or Kruskal-Wallis tests (non-normally distributed). *NS*: no significance. * $p < 0.05$, ** $p < 0.01$, *** $p < 0.001$, **** $p < 0.0001$. Scale bar, 10 μm.

To better integrate the above three parameters for evaluating the nuclear morphology influenced by observation angles, we employed principal component analysis (PCA). The first principal component (PC1) accounted for a significant portion of the total variance, ranging between 40.89% and 80.07%, making it a robust indicator.[181] A deeper examination of the PC1 for the 30 Huh7 cells across eight viewing angles reveals considerable variations, as depicted in Fig. 3.12d. Remarkably, out of these

samples, 29 cells exhibit significant differences ($p < 0.05$) in the PC1 across the multi-angle views. In contrast, cell #29 maintains consistent morphology regardless of the viewing angle, as detailed in Fig. 3.13.

Huh7-#29

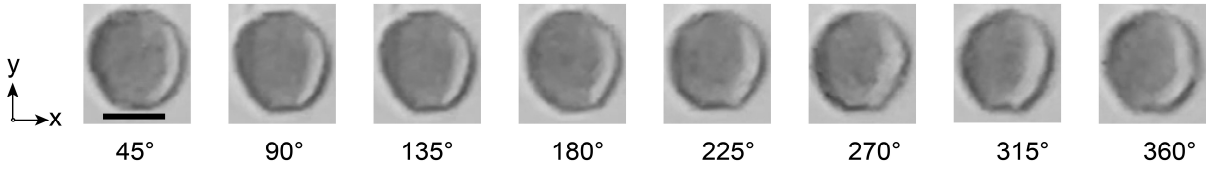

Figure 3.13. The microscopic image of the Huh7-#29 during the rotation. Scale bar, 10 μm.

The observation angle plays a vital role in quantifying nuclear morphology at the single-cell level. Details are shown in Figs. 3.14a-c, where all three parameters display significant differences under multi-view observations, while the N/C ratio varies more than the circularity and solidity (Fig. 3.14d). During the rotation of the 30 cells, cells #4 and #16 displayed notable fluctuations in nucleus circularity and N/C ratio values, ranging from 0.51 to 0.92 and 0.43 to 0.83, respectively. Such variations surely add complexity to cytological analysis, emphasizing the need for a thorough evaluation. For example, misshapen nuclei of fibroblast are often used as the warning signs of diseases, defined as circularity $\leqslant 0.65$,[182, 183, 184] therefore, a careful observation is required for accurate diagnosis. Similarly, distinguishing between circulating tumor cells with a N/C ratio greater than 0.8 and leukocytes with a smaller N/C ratio can be challenging, particularly in liquid biopsies where both may coexist.[185, 186] The observation angle from the results shows that it is crucial to correctly classify these cell types.

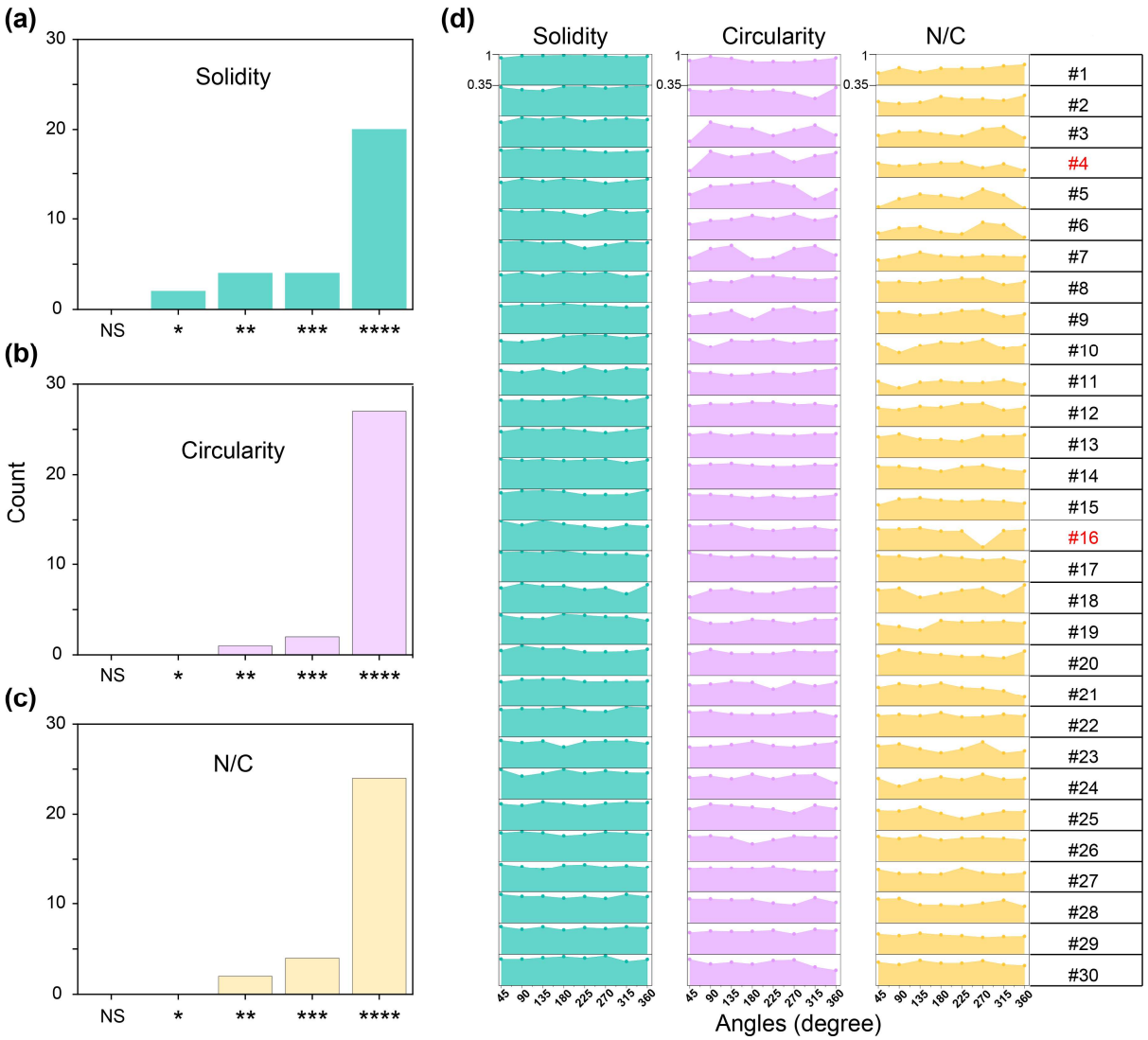

Figure 3.14. Statistical analysis of the multi-angle impact on Huh7 cell cytopathology evaluation. Significant difference analysis of nuclear (a) solidity, (b) circularity, and (c) N/C for single-cell during one circle rotation process. (d) The shaded connection lines of eight angles for each cell further visually reflect the significant effect of the multi-angle on the three nuclear parameters quantification (n = 30). All p-values were determined using one-way ANOVA (normally distributed) or Kruskal-Wallis tests (non-normally distributed). *NS*: no significance. *: $p < 0.05$, **: $p < 0.01$, ***: $p < 0.001$, ****: $p < 0.0001$.

3.2.6 Enhanced Sensitivity through Cell Rotation

After successfully demonstrating the MARC device's capability in assessing cellular morphology from multiple angles, we further explored its potential to differentiate between tumor and normal tissue cells using this approach. Breast and lung cancer

cells, along with their normal tissue counterparts, were used with the results shown in Figs. 3.15a-b.

In the case of breast cancer cells (MDA-MB-231), the N/C ratio measured during the rotation was found to be higher than that of epithelial cells from the mammary gland (MCF-10A). This contrasts dramatically with the results from the conventional slide-based examination, which shows no significant difference between cancerous and normal counterpart cells, as illustrated in Figs. 3.15d-e. Similarly, lung cancer cells (A549) exhibited a lower N/C ratio compared to that of the lung epithelial cells (BEAS-2B). The average N/C ratio obtained from the rotation of A549 cells was smaller than that of BEAS-2B cells (Fig. 3.15b), seemingly contradicting the characteristic expectation of cancer having enlarged N/C ratios due to increased chromatin content within malignant cells.[187] However, this discrepancy could be attributed to alterations in their biophysical properties resulting from genetic editing during cell line development.[188] These results demonstrate the MARC device's ability to offer a different perspective on N/C ratios between cancerous and noncancerous cells, providing additional data that may not be as apparent with single-plane traditional slide-based cytology. This Supporting Information could contribute to more informed cytological discrimination.

Another valuable application of the MARC is in phenotyping various cancer cell types, particularly in the context of differentiating cells in biofluids.[189, 190] The rotation-based N/C ratio measurements (Fig. 3.15c) reveal significant differences among A549, MDA-MB-231, and Huh7 cells, with mean values of 0.51, 0.68, and 0.78, respectively. In contrast, the traditional single-plane measurements (Fig. 3.15f) show a narrower spread in mean values (0.61, 0.63, and 0.70, respectively). Because MARC quantifies N/C across multiple viewing angles during rotation, whereas conventional cytology measures a single 2D projection, the absolute mean values are not expected to match one-to-one between the two methods. Instead, the key outcome is that MARC provides clearer separation between cell types in this dataset, indicating improved discriminatory power compared with standard single-plane cytological examination. Therefore, in this thesis MARC is positioned as a pre-cytopathological screening/triage approach to support and prioritise downstream conventional cytology, rather than as a stand-alone cancer screening or diagnostic test.

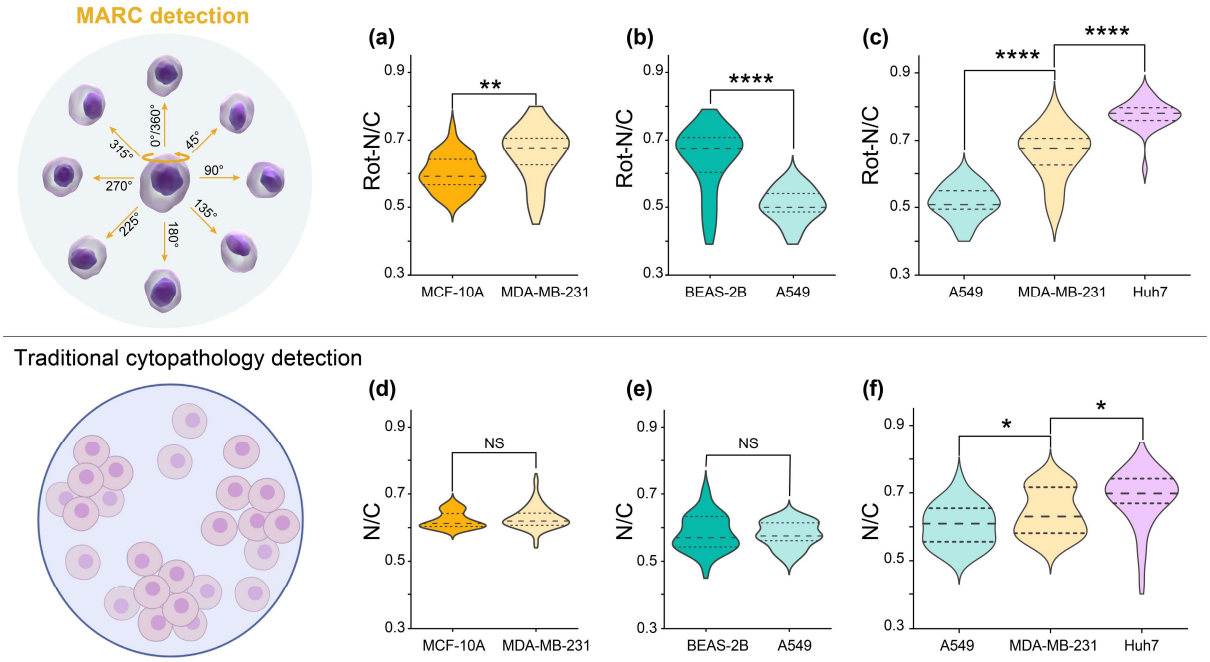

Figure 3.15. N/C-based examination of cells. Rotation-based N/C comparison between (a) breast healthy cell MCF10A and breast cancer cell MDA-MB-231, between (b) lung healthy cell BEAS-2B and lung cancer cell A549, and among (c) three cancer cells: lung cancer cell A549, breast cancer cell MDA-MB-231 and liver cancer cell Huh-7. Traditional cytopathology detection one angle quantification based N/C comparison between (d) breast healthy cell MCF10A and breast cancer cell MDA-MB-231, between e) lung healthy cell BEAS-2B and lung cancer cell A549, and among (f) three cancer cells: lung cancer cell A549, breast cancer cell MDA-MB-231 and liver cancer cell Huh-7. All cell lines were analyzed based on the quantification of 30 cells, per cell averaged by the N/C value of 8 angles. All p-values were determined using one-way ANOVA. *NS*: no significance. * $p < 0.05$, ** $p < 0.01$, **** $p < 0.0001$.

The multi-angle analysis provided by the MARC device enriches cytology by providing a more comprehensive understanding of cellular morphology, thereby aiding in overall evaluation. It is worth noting that the MARC device aims to rotate cells along the y-axis only, unlike the rotation induced by microbubbles, which involves in rotations in both the $x-$ and $y-$axes. This operational difference facilitates device simplification and throughput enhancement, while still achieving a considerable sensitivity in revealing cellular morphology throughout the entire revolution. As depicted in Fig. 3.15, the specificity of MARC in identifying samples with significant N/C ratio variances underscores its potential as a preliminary screening tool. In light of these findings, we propose that MARC can enhance precytopathological screening by identifying

samples marked as positive that undergo further traditional cytopathological evaluation, as illustrated in Fig. 3.16. This strategic approach holds the potential to greatly enhance the diagnostic efficiency. By directing only positively screened samples to subsequent traditional cytopathology, MARC has the great potential to optimize diagnostic efficiency.

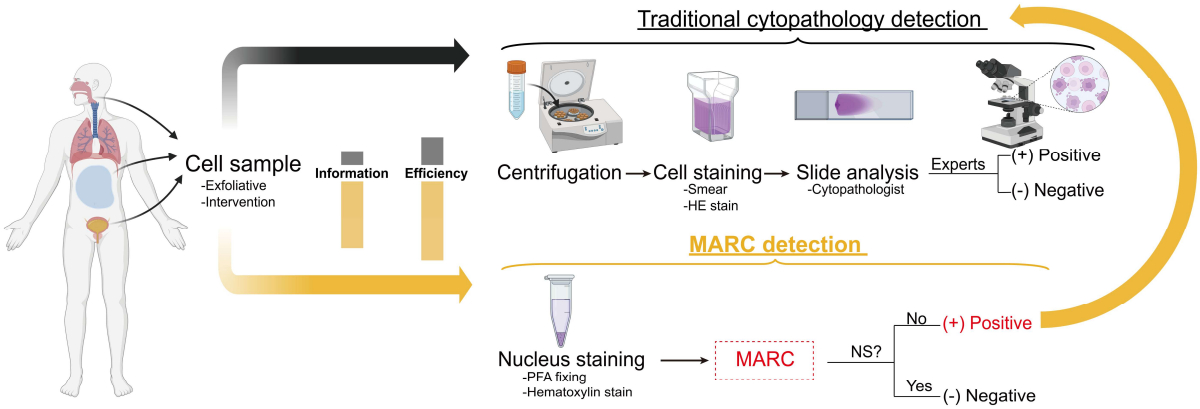

Figure 3.16. The envision illustration for MARC enabled cytopathological screening. Cell samples collected from biofluid are subjected to two analysis pathways. The traditional path involves sample centrifugation, hematoxylin and eosin (HE) staining and cytopathologist examination, yielding binary outcomes based on experience. Alternatively, the MARC detection route offers nucleus staining and muti-view morphological analysis. Only positive MARC results (No NS: significance) prompt traditional cytopathology, enhancing screening efficiency and information depth.

3.3 Conclusion

In this chapter, we introduced the MARC device to enhance the analytical information at the single cell level. Its capability provided multi-angle morphological insights into hepatocyte cell line Huh7 and IHH cells dramatically improved our ability to interpret cytopathological evaluations. A notable feature of this advanced cytometry is its precision, characterized by the controlled rotation speed of two cell traces, adjustable through the modulation of the device's input power. The MARC device's ability to amplify morphological variations, particularly the N/C ratio dynamics, has shown exceptional proficiency in differentiating between cancerous and noncancerous cells, surpassing traditional cytopathological methods. These findings indicate that MARC holds good promise in enhancing pre-cytopathological screening. By focusing on samples that test positive in MARC screening for further analysis through traditional

cytopathology, it could greatly improve the efficiency of the diagnostic process and optimize the use of medical resources.

3.4 Robustness, Reproducibility, and Biomedical User Feedback

Repeat experiments and reproducibility. The main comparison results in this chapter were assessed for repeatability across device runs performed on different days. For each cell line, all measurements were taken from the same fixed sample tube (same batch); however, the sample was loaded and processed on multiple days, meaning each dataset corresponds to a separate device run with a new loading/trapping/rotation sequence. This design tests technical reproducibility (day-to-day repeatability of device operation and analysis) while holding the biological sample constant. It should be noted that this does not constitute an independent biological replicate (e.g., different culture passages, independently prepared samples, or patient specimens), which would be required to demonstrate broader biological generalisability.

Biomedical user feedback. Feedback gathered during discussions with cytopathologists and workflow observation indicated that (i) a large proportion of routine screening samples are true-negative yet still consume review time, and (ii) multi-view morphology could be valuable where single-view assessment is ambiguous. In this context, MARC's ability to maintain focus while rotating cells and quantify angle-dependent morphology (e.g., N/C ratio variation) aligns with user-identified needs for efficient pre-screening.

Standards of proof and current scope. The results presented here meet a proof-of-concept standard commonly expected at the device-development stage: repeatable operation across independent runs and statistically supported separation of cell-line datasets. However, biomedical standards for translation would require additional validation, including independent biological replicates, multi-operator/multi-day studies, blinded comparison against expert ground truth, and evaluation on clinically relevant specimens with diagnostic performance metrics (e.g., sensitivity/specificity and inter-rater agreement).

3.5 Limitations and Practical Considerations

This chapter demonstrates controlled, multi-view rotation of individually trackable cells and shows that viewing angle can influence morphology metrics (e.g., apparent N/C

ratio), highlighting the value of multi-angle imaging for pre-cytopathological screening. However, the comparison is currently demonstrated on a limited set of fixed cell lines under controlled conditions; generalisation to primary clinical samples will require larger cohorts, blinded evaluation, and benchmarking against ground-truth pathology outcomes. In addition, while MARC enables parallelised rotation with a compact footprint, the achievable rotation range and stability remain dependent on operating parameters (e.g., acoustic field configuration, medium properties, and cell size/contrast), and also needs manually fine-tune by the operator. Future work should include systematic inter-day/inter-device reproducibility studies and user-centred validation with cytopathologists to define performance thresholds for clinical adoption.

3.6 Methods and Materials

3.6.1 Device Fabrication and Assembly

To simplify the fabrication process, the IDTs on the MARC device were manufactured by using a PCB technique.[170] Briefly, a PCB patterned with a pair of gold interdigital electrodes was mechanically mounted to a piezoelectric substrate ($LiNbO_3$) to form the IDT by using a jig (Fig. 3.17). The specifications of the PCB IDT and the microchannel are provided in Table 3.2. The Rayleigh SAW wavelength produced by the MARC device was $\approx$200 μm.

For the microchannel fabrication, a standard PDMS technique was employed, consistent with our previous studies.[172] Initially, a 60 μm thick layer of SU-8 photoresist was spin-coated onto a 4 inch silicon wafer and patterned by using a mask aligner. The silicon wafer's surface was then coated with silane vapor to modify its surface properties. Subsequently, the PDMS microchannel was cast from the silicon mold with a 10:1 (w/w) mixture of PDMS base and curing agent (Sylgard 184, Dow Corning), after degassing, the PDMS was cured at 65 °C for 1 h. Finally, the cured PDMS microchannel was punched to create inlet and outlet ports for sample loading.

The assembly process for the MARC device began with the thorough cleaning of the PCB IDTs and the PDMS microchannel using isopropyl alcohol followed by deionized water. Various components of the jig as illustrated in Fig. 3.17a, including two main holders, two localized pressers, four reverse stands, and a microchannel presser, were all 3D printed. The $LiNbO_3$ substrate was placed onto a customized aluminium plate to support the mechanical components. When mechanically clamping the two

components, the finger electrodes of the PCB were aligned in parallel with the reference flat on the $LiNbO_3$.

Four pogo pins were contacted with the bus pads on the PCB to deliver RF signals to the MARC device, eliminating the need for soldering any cables directly onto the IDTs and improved the device's pinout robustness. After the PCB IDTs were assembled, the PDMS microchannel was placed onto the $LiNbO_3$. A 4 mm thick acrylic presser was then mounted onto the PDMS microchannel, providing even force distribution across the microchannel. A microchannel presser was positioned above the acrylic presser to firmly clamp the PDMS microchannel onto the $LiNbO_3$. The entire MARC device was mechanically assembled, allowing for on-demand cleaning and amendment. The combination of the PCB technique and mechanical packaging offered flexibility in constructing acoustofluidic devices.[191] A polarizer (43785, Edmund Optics) was placed below the $LiNbO_3$ substrate to correct the polarization, securely fitted into the hole of the aluminium plate. To enhance observation quality specifically to eliminate double-image phenomena and achieve clearer visibility, the device was inverted to observe from the $LiNbO_3$ side.

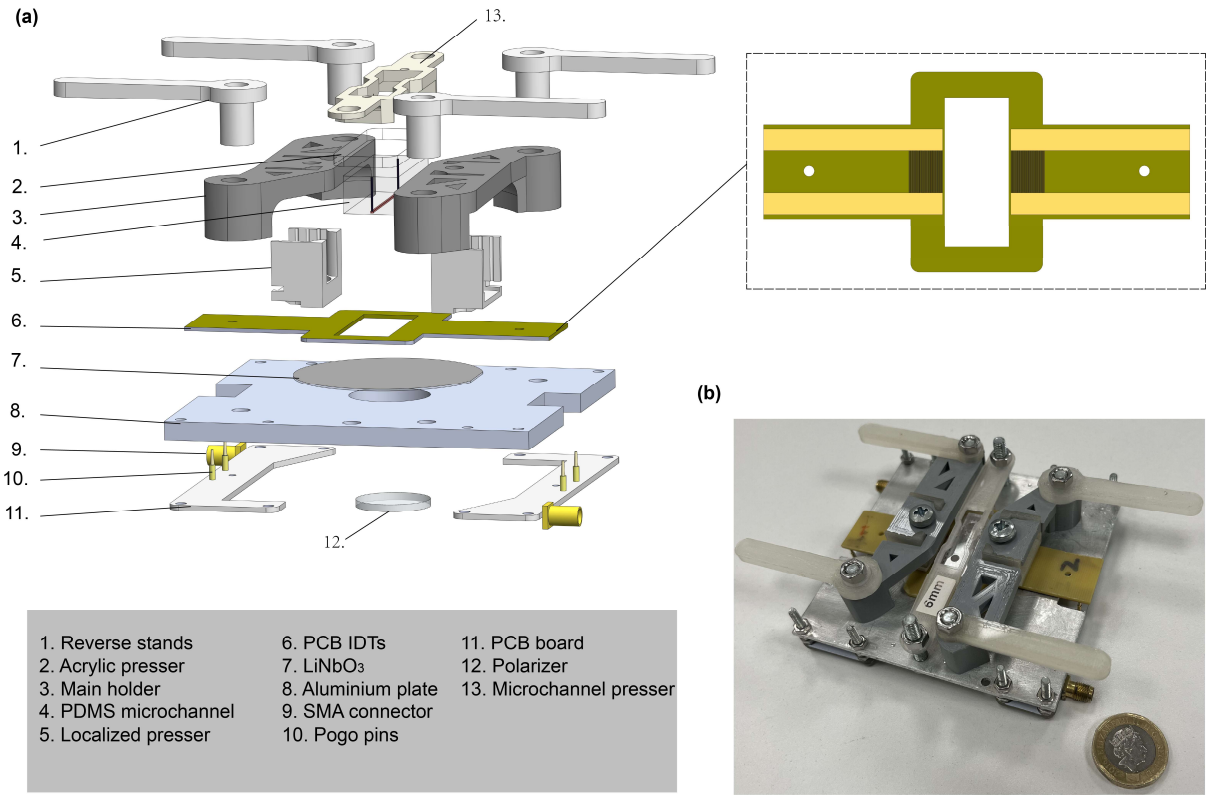

Figure 3.17. The components and assembly of the MARC device. (a) 3D exploded view of the MARC device. (b) Real image of the assembled MARC device.

Table 3.2. Detailed geometry parameters of the PCB IDT and PDMS microchannel.

PCB IDT	IDT finger width	IDT finger space	wavelength	aperture	IDT pairs
	38.7±3.1 μm (Average±SD)	61.1±3.0 μm (Average±SD)	199.6±4.8 μm (Average±SD)	10 mm	40
PDMS microchannel	width	height	length	PDMS thickness	
	200 μm	60 μm	15 mm	5 mm	

3.6.2 Cell Sample Preparation

Human hepatocytes cell lines, the Huh7 (JCRB cell bank) and IHH (JCRB cell bank),[192] human lung cell lines, the human bronchial epithelial Beas-2b (CRL-9609, ATCC) and human non-small cell lung cancer A549 (CCL-185, ATCC), as well as human breast cell line such as human mammary epithelial cell line MCF-10A (CRL-10317, ATCC) and human breast cancer MDA-MB-231(HTB-26, ATCC), were cultured in Dulbecco's modified Eagle's medium supplemented with 10% fetal bovine serum and 1% penicillin–streptomycin. The cells were passaged every 4 to 5 days upon reaching 65–80% confluency by trypsin incubation for 1–2 min, followed by phosphate-buffered saline (PBS) washing and resuspension. The cells were then fixed with 4% paraformaldehyde for 15 min and centrifuged at 1500 rpm for 5 min to isolate the cells from the supernatant. Finally, the cells were washed again to remove the remaining paraformaldehyde.

3.6.3 Nucleus Staining and Morphology Quantification

Cell nucleus staining procedure was performed by following these steps. 1) Nucleus staining: Fixed cells were suspended in 60× Mayer's hematoxylin (12603957, Fisher Scientific) in PBS to stain the nucleus for 2 min, followed by PBS washing by centrifuging at 1200 rpm for 3 min. 2) Differentiation: 2% acid alcohol was added for differentiation and immediately centrifuged the mixture at 1000 rpm for 1–2 min, and then removed the supernatant. 3) Antiblue treatment: The cell precipitate was immersed in 0.5% ammonia solution for 2 min, then centrifuged at 1000 rpm for 1–2 min, after which the supernatant was carefully removed. 4) Decolorization: 70% ethanol was added to the cell precipitate and immediately centrifuged the mixture at

1000 rpm for 1–2 min, followed by removing the supernatant. 5) Cell collection: PBS was added to resuspend the cell precipitate. This study analyzed five nucleus shape parameters of importance for cancer diagnosis, i.e., convex hull, perimeter, area, solidity, circularity, and nuclear-to-cytoplasmic ratio. Solidity, defined as the ratio of the nucleus to its convex hull, was served as an indicator to assess the concavity and lobulation of the nucleus.[193] Circularity, calculated as 4·p·nucleus area/nucleus perimeter,[165] quantifies how closely a cell nucleus resembles as a perfect circle.[194] The N/C ratio, representing the ratio of the nucleus area to the entire cytoplasmic area, provided insight into cell malignancy and atypia.[180]

3.6.4 System Setup

Fig. 3.1.a shows the schematic of the system setup. The cells were injected into the PDMS microchannel using a syringe pump (74905-54, Cole-Parmer). Before loading the cells, 1% (v/v) bovine serum albumin solution was coated to the microchannel to prevent cell adhesion, at a flow rate of 5 μL/min for 30 min. All experiment data were observed and recorded through an upright microscope (OBD 127, Kern) equipped with a 20× objective lens. RF signals were generated using a signal generator (123-6578, RS pro) and amplified by an RF power amplifier (LZY-22+, Mini circuit). The forward and reflected powers were monitored using two power meters connected to two couplers (ZFBDC20-62HP-S+, Mini-Circuits). L-C matching networks were designed for the PCB IDTs to minimize power reflection from the IDT. Both PCB-IDTs, prepared using PCB technique, resulted in a Rayleigh frequency around 19.61 MHz. The reflection coefficient, S_{11} or S_{22}, was used to characterize the frequency response of the IDTs. The matching network was used to optimize the signal transmission to the IDT and protected the output stage of the RF power amplifier. Fig. 3.18 shows that the S_{11} for both IDTs are greatly reduced to −32.3 and −32.1 dBm, respectively, which closely resemble those of IDTs manufactured using conventional photolithography techniques.

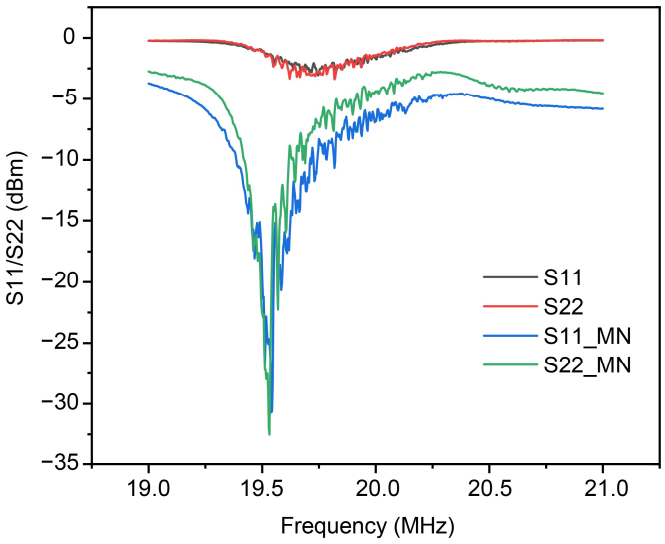

Figure 3.18. Electrical characterisation of the S_{11} and S_{22} of the MARC with and without matching networks.

3.6.5 Numerical Analysis

To investigate the acoustofluidic field within a PDMS microchannel on the $x-z$ plane, the finite element method (FEM) simulation was conducted using COMSOL Multiphysics (Version 6.0, COMSOL AB). The Piezoelectricity Multiphysics and Thermoviscous Acoustics Modules were employed for this study. The model geometry consisted of ten pairs of IDT fingers (50 μm × 5 μm) with a wavelength of 200 μm, located on a 300 μm thick $LiNbO_3$ wafer. The dimensions of the PDMS channel boundary were varied using the built-in parametric sweep function, with steps of 20 μm in height (40–100 μm) and steps of 50 μm in width (100–300 μm). The liquid domain and its properties were defined as water. Initially, a frequency domain solution was performed to obtain the mechanical displacements of the piezoelectric material and the resulting acoustic pressure induced in the liquid. These acoustic pressure values were subsequently employed in the stationary solver to solve for the acoustic pressure-induced liquid streamlines.

3.6.6 Analysis of Cell Rotation

Compared to many other studies involving customized algorithm for rotational analysis,[195, 196, 197, 198] the current study used Tracker (Version 6.0.8, Open Source Physics), a free video analysis and modelling tool, to perform the analysis of rotational angles and speed. In this study, videos and images were analyzed by the Tracker (OSP) and ImageJ (National Institutes of Health) software, respectively. To trace the

rotation angle, 8 Huh cells were randomly selected and tracked them through two complete rotation cycles in Tracker, recording the timestamp at each 45° interval. For determining the rotation speed, 15 randomly selected Huh7 cell rotation cycles were analyzed, each representing a full 360° rotation, from the two cell traces. Using Tracker software, the number of frames ($x_n - x_0$) was counted for a 360° rotation. The cell rotation speed ω can be calculated using the following equations,[195]

$$\omega = \frac{60(x_n - x_0)}{FPS} \tag{3.4}$$

where FPS represents the frame rate of the camera capturing the rotation. Additionally, the measurement of parameters such as nucleus area, nucleus convex hull area, nucleus perimeter, cytoplasm area, cell area, cell perimeter, and N/C ratio is typically accomplished through interactive image analysis and segmentation techniques made available in ImageJ. 1) Nucleus Area: the pixel area occupied was interactively identified and measured by the nucleus in the frame image, often after thresholding to separate the nucleus from the background. 2) Nucleus Convex Hull Area: the area of the smallest convex shape was outlined that can entirely enclose the nucleus. ImageJ calculated this by creating a convex hull around the segmented nucleus and measuring its area. 3) Nucleus Perimeter: This measured the total length of the boundary around the nucleus. ImageJ determined this by tracing the outline of the segmented nucleus. 4) Cytoplasm Area: The cytoplasm area was measured by subtracting the nucleus area from the total cell area after segmenting the cell and the nucleus separately. 5) Cell Area: This parameter is the total pixel area occupied by the entire cell, including both the nucleus and the cytoplasm. ImageJ calculates this by segmenting the cell from the background. 6) Cell Perimeter: Similar to the nucleus perimeter, this is the total length of the boundary around the entire cell outlined around the segmented cell. 7) N/C Ratio: The N/C ratio was computed by dividing the intensity measurement of the nuclear region of interest (ROI) by that of the cytoplasmic ROI (Fig. 3.12a).

3.6.7 Statistics Analysis

In this case, principal component analysis (PCA)[199] was conducted after z-score standardization of cell nucleus solidity, circularity, and N/C indices. The first coordination of PCA (PC1) accounted for the most of total variances was used as the reduced set of nucleus shape index. One-way ANOVA (normally distributed) or

Kruskal-Wallis tests (non-normally distributed) were performed to evaluate the statistical significance of differences. *, **, ***, and **** indicate $p < 0.05$, 0.01, 0.001, and 0.0001 between the conditions, respectively, and *NS* indicates statistically no significant difference between the conditions. All statistical results were plotted using Origin (OriginPro 2023, OriginLab).

Chapter 4: Manipulation at the Tissue Level for Transdermal Drug Delivery

In the previous chapter, we achieved cell rotation manipulation and successfully applied the MARC device in cytopathological screening. In this chapter, we aim to achieve tissue-level manipulation. Tissue is composed of multiple cells that form tight intercellular connections; therefore, it is difficult to manipulate tissues directly in the same way as single cells. However, acoustofluidic devices can generate perturbations on tissues, which can indirectly manipulate the cells within them to achieve so-called "tissue-level manipulation". Here in this chapter, we choose the skin as the target object. We build an Acoustic Droplets Activated Permeation (ADAP) device that jets droplets to impact the skin. Upon contact, these droplets create intense air entrapment that generates a downward compressive force and induces accelerated fluid streaming, disrupting the skin stratum corneum (SC) layer and enhancing transdermal drug delivery permeability. We use simulation and experiment to optimize the ADAP design for the desired droplet dispensing. By quantifying the perturbation effects, we further investigate three regions of interest from droplet falling to fluid perturbation, where we find a controllable relationship between input voltage and perturbation intensity. Furthermore, three drug molecules with different molecular weights (376 Da, 10 kDa, and 70 kDa) are used to validate ADAP's transdermal efficacy. Finally, using the hypoglycemic mouse model, we successfully demonstrate ADAP's capability for effective and ultrafast *in-vivo* glucose delivery, which is also shown to be non-invasive via HE tissue sections.

The corresponding manuscript in the chapter has been submitted:

- X. Zhang, Y. Li, P. Dumčius, et al. Acoustofluidics Powered Transdermal Drug Delivery for Ultrafast Non-Invasive Disease Therapy. (*Under Review*)

Author Contribution:

I (Xiaoyan Zhang) contributed to the conception and application framing, led the device design-for-experiment iteration, conducted the experimental work (device operation, tissue-level manipulation tests, and microscopy imaging), and performed data processing and quantitative analysis. I also drafted the original manuscript text and

coordinated revisions with co-authors. The numerical modelling/simulation presented in this chapter was performed by a co-author (Povilas Dumčius) and is included to support design interpretation and explain observed trends, rather than as my original modelling contribution.

4.1 Introduction

4.1.1 Background

As the body's largest organ, skin protects against germs, regulates body temperature and enables touch (tactile) sensations. The skin's main layers include the epidermis, dermis and hypodermis and is prone to many problems, including skin cancer, acne, wrinkles and rashes. Transdermal drug delivery (TDD) has recently made important contributions to medical therapy.[200] Compared to intravenous injection, oral administration, and parenteral injection, the TDD is an attractive alternative due to its minimally invasive, high-patient compliance, bypass nature of gastrointestinal and liver degradation.[201, 202] However, drug penetration through the skin remains a significant challenge due to the stratum corneum (SC), the skin's outermost barrier layer, composed of anucleated cells embedded in lipid bilayers.[203, 204] This SC layer is primarily responsible for low skin permeability and offers the limiting step in transdermal drug permeation.[205] Various strategies have been developed to overcome this limitation, including chemical enhancers,[206] iontophoresis,[207, 208] thermal,[209] microneedles,[210, 211, 212] and electroporation.[213, 214] These methods, however, often show issues or limitations such as irritation or toxicity to living cells, serious skin pain, physically invasive, and/or side effects to skin after treatment.

Acoustic-based methods have recently emerged as a promising solution, offering non-invasive, portable, active, programmable, wireless, and flexible delivery options with minimal side effects in drug delivery.[215] They generally include methods using ultrasonics or acoustic waves including, surface acoustic waves (SAWs), bulk acoustic waves, or Lamb waves.[216, 217, 218, 219] Ultrasonics or acoustic waves increase skin permeability through two main mechanisms. The first one is cavitation, in which bubbles are oscillated and collapsed at the skin surface to generate localized shock waves and liquid microjets which target and damage the SC layer. The second one is non-cavitation ultrasound/acoustic waves, which use pressure gradients and oscillations to disrupt lipid structures of the skin's SC layer.[200, 220] Previous studies using piezoelectric transducers have successfully demonstrated non-invasive anti-

inflammatory treatment,[221, 222] cosmeceutical delivery efficacy enhancement,[95, 96] topically pain-killing drug fast release;[97] and transcanal inner ear drug delivery without damaging the auditory responses.[223] Interdigitated transducer (IDT) based SAWs have also been developed for TDDs, including localised delivery of therapeutic agents in porcine buccal model's mucosa,[219] and wirelessly powered SAWs transport hyaluronate rhodamine to pig skin tissue.[216] Acoustic waves have also been recently integrated with microneedle technology generating acoustic streaming and enhancing deeper tissue delivery.[63, 224, 225] However, most these acoustic transdermal methods have not solved the key issues of long administration period, limited delivery efficiency, or impractical applications for rapid-response acute disease therapies. Meanwhile, although microneedle-integrated acoustic approaches can achieve effective TDD, they remain invasive and often cause skin discomfort. Furthermore, current acoustic techniques commonly lack the convenient flexibility to dynamically control both delivery efficiency and penetration depth.

Acute diseases develop rapidly with life-threatening symptoms and commonly require immediate pharmacological intervention. One of the prime examples is hypoglycemia, defined as a blood glucose level below 70 mg/dL, and it is a commonly serious complication for people with diabetes. In a global survey of over 27,000 insulin-treated patients, more than 80 % of those with type 1 diabetes and nearly 50 % of those with type II diabetes experienced at least one hypoglycemic episode each month; and severe hypoglycemia affected 14 % of type 1 and 9 % of type II participants.[226] In the UK alone, cost of managing hypoglycemia is estimated ~£468 million annually, including £295.9 million for severe cases and £172.1 million for non-severe ones.[227, 228] Severe hypoglycemia is commonly associated with heightened risks of macrovascular and microvascular complications and often leads to transient central nervous system dysfunction, requiring external assistance.[229] Currently, the standard treatments for severe hypoglycemia are intramuscular glucagon or intravenous glucose infusion.[230, 231] Intravenous glucose acts quickly, typically within 4–6 minutes, but requires administration by healthcare professionals. Glucagon autoinjectors are more suitable for home use, yet they have longer onset times (over 10 minutes), are costly, and often induce side effects such as nausea and vomiting for up to 20 % of patients.[231, 232, 233] These limitations underscore the urgent need for a non-invasive, effective and ultrafast drug delivery system which can be convenient for at-home

administration, not only for hypoglycemia but for acute disease management in general.

4.1.2 Design Rationale and Development Process

Informed by discussions with dermatology clinicians and drug-delivery specialists, this project was initiated to address two real-world needs in transdermal drug delivery. First, many mainstream delivery approaches remain invasive, which can cause substantial pain and lead to visible irritation/damage or other side effects after treatment.[216, 234] Second, conventional transdermal delivery is often limited by the skin barrier, restricting achievable dose and making it unsuitable for acute conditions with a short therapeutic administration window.[63, 229] These needs motivated the development of a fully non-invasive platform that can enhance transdermal transport while minimising discomfort and skin damage.

These clinical requirements translated into specific design targets: (i) non-invasive, skin-compatible actuation with minimal mechanical damage; (ii) measurable and controllable enhancement of delivery efficiency, with tunable delivery rate and penetration depth via operating parameters; (iii) repeatable performance across samples and runs; and (iv) practical integration with standard workflows (simple mounting and compatibility with common drugs). Acoustofluidic actuation was selected to meet these targets because acoustic fields can be applied externally and without penetrating the skin, while providing tunable energy input that can induce controlled mechanical effects near the skin interface to enhance transport. Guided by these targets, the ADAP architecture was established through iterative design–test cycles, refining the chamber/nozzle configuration and actuation conditions to achieve robust delivery enhancement under safety/comfort constraints; supporting numerical modelling informed field/flow distributions and guided design choices, while experimental validation defined the operating window and quantified performance.

In this proof-of-concept study, we therefore present an acoustic-droplet-activated permeation (ADAP) platform for rapid, non-invasive, and tunable transdermal delivery, validated using a hypoglycaemia mice model. ADAP couples a piezoelectric transducer with a central micro-nozzle to eject microscale droplets onto the skin; as droplets accumulate into a thin liquid film, trapped air forms a transient “air-bubble cloud” at the interface. Bubble oscillation generates localised mechanical stresses and

microstreaming that perturb the outermost stratum corneum (SC), enabling enhanced permeation and transport into tissue. By adjusting input voltage (and frequency where applicable), droplet density/impact and the resulting perturbation intensity can be tuned to regulate delivery rate and penetration depth. Ex vivo experiments with fluorescein sodium and FITC–dextran (10 and 70 kDa) show permeability enhancements of several orders of magnitude over passive diffusion, and in vivo studies demonstrate that a 5-minute ADAP treatment restores blood glucose levels in hypoglycaemic mice without detectable skin damage. With further development toward a user-friendly integrated device and rigorous clinical validation, ADAP has potential as a safe, fully non-invasive approach for rapid, at-home management of acute conditions.

4.2 Results and Discussion

4.2.1 Device Setup and Working Principle

Fig. 4.1a illustrates that the ADAP generates impinging droplets downward and creates air bubble cloud onto the surface of skin. As shown in the right insert of Fig. 4.1a, the ADAP device's key actuator is composed of a piezoelectric transducer (PZT) unit bonded to a metal plate featuring a central micro-hole nozzle, encased within a pair of acrylic encapsulations. The drug solution is loaded into the reservoir above the metal layer. In more details, when the PZT unit vibrates, the capillary waves are created in the metal layer and cause localized pressure fluctuations within the drug liquid (Fig. 4.1b.I). Due to the conical structure of the micro-hole, it works as a nozzle and enables liquid overcoming surface tension to pinch off, thus ejecting droplets downside. In the case of passive diffusion without acoustic waves (Fig. 4.1b.III), the delivery of drug molecules is commonly blocked by the dense SC barrier, which causes a poor skin permeability. In contrast, our ADAP method (Fig. 4.1b.II) ejects droplets onto the skin surface and these droplets accumulate into a thin liquid film. Subsequently when the successive liquid droplets strike onto the skin, many air bubbles are entrapped within the liquid, forming a transient "air bubble cloud". We speculate this air bubble cloud may behave like a single ultrasound-responsive giant microbubble that effectively enhances the TDD through two mechanical principles instead of cavitation jetting.[235, 236] Firstly, its rapid oscillations generate localised impact, translational, and shear forces which briefly disrupt the SC's lipid bilayers, opening transient pathways for the TDD of drug molecules. Secondly, the intense

droplet collisions drive an accelerated streaming flow within the liquid layer, effectively injecting the drug molecules deeper into the epidermis. By coupling a momentary increase in skin permeability with accelerated fluid transport, the ADAP approach can achieves the efficient and non-invasive TDD.

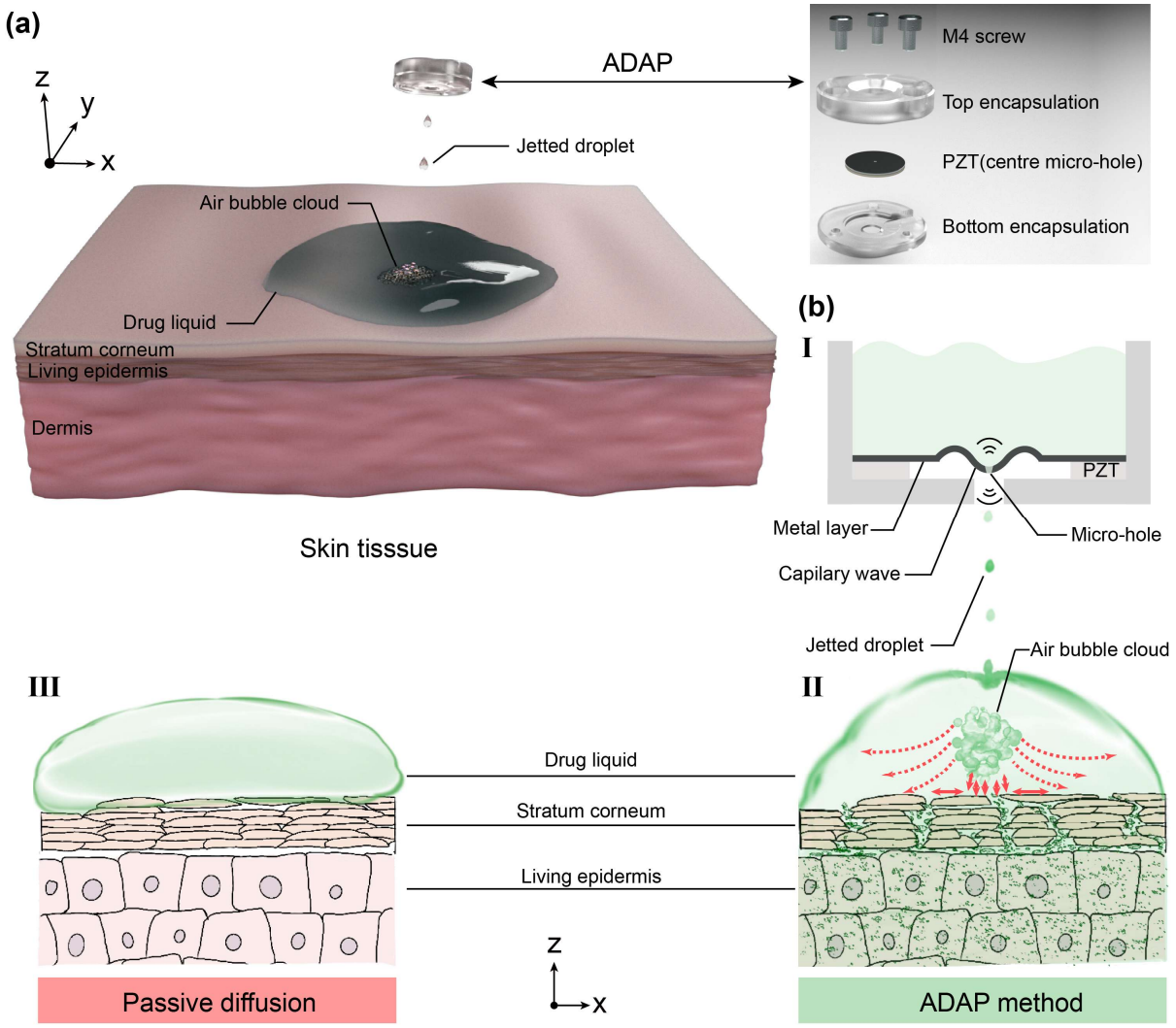

Figure 4.1. Working principle for ADAP enabled transdermal drug delivery. (a) Schematic illustration of the working mechanism and main actuator components of ADAP device. (b) ADAP method enabled transdermal delivery. I: PZT vibration causes capillary wave to jet droplets through the centre micro-hole, which will then II: entrap intensive air bubble cloud upon the stratum corneum surface. On the one hand, the continuous collision leads the bubble could oscillation may cause mechanical forces (red solid arrows) that cumulatively pull apart cell crevices onto the stratum corneum layer. On the other hand, it also induces fluid streaming (red dashed arrows) that may pump drug diffusion into the deeper tissue. The synergistic effect of the both effects

enables the fast and non-invasive transdermal delivery. III: Schematic of traditional passive diffusion method that has limited drug permeation.

4.2.2 Optimization for Droplet Generation

The impedance characteristics of the PZT unit were firstly characterized within the frequencies from 0 to 200 kHz, and the obtained results are shown in Fig. 4.2. The measured impedance plot reveals two resonant frequencies at around 21 kHz (f_{r_1}) and around 110 kHz (f_{r_2}) which show the lowest impedance values and can generate the largest vibration amplitude.

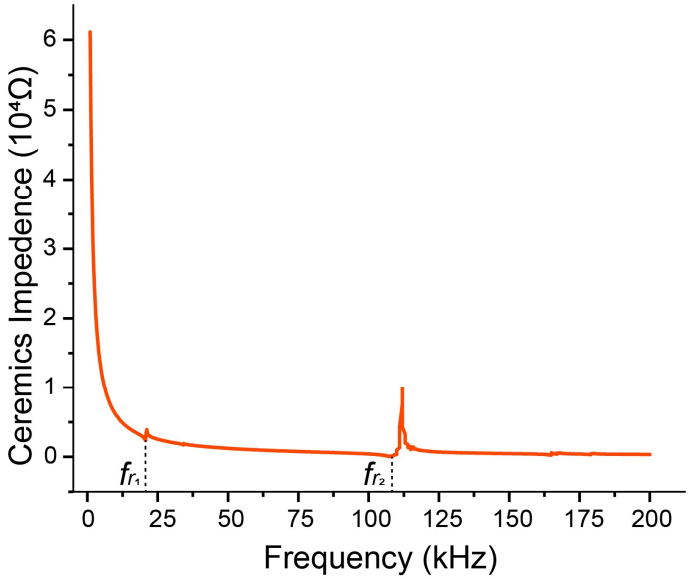

Figure 4.2. Acoustic impedance reading of the PZT unit range from 0~200 kHz.

The performance of PZT unit with a centre micro-hole structure to dispense liquid droplets is strongly dependent on the actuating frequency, the liquid type, and the micro-hole size. In this study, we used high-energy pulsed laser machining to obtain a 100 μm (diameter) micro-hole in the metal layer as the nozzle for droplet generation. To evaluate the performance of the system to eject droplets, a dimensionless surface tension parameter *S* is introduced:[237]

$$S = \frac{2\sigma}{\rho r^3 f^2} \tag{4.1}$$

Where σ, ρ, r, f are the surface tension and density of the liquid, micro-hole radius, and driven frequency. To enable droplet's jetting, the value of *S* should be on the order of 1 or greater (i.e., $S \geq 1$) for the breakup of the droplets from the liquid air interface.

Otherwise, the wavelength of the short ripples on the liquid surface would be too small for the drop to pinch off from the liquid.[237] In this study, we used DI-water as the liquid sample (density: 1 g/mL, and surface tension: 0.072 N/m) for calculations. Based on the *S* value plot shown in Fig. 4.3, in this condition with the micro-hole radius of 50 μm, the droplet could only be ejected at the frequency below around 33 kHz so the working resonant frequency for droplet generation should be at around f_{r_1}, i.e., 21 kHz.

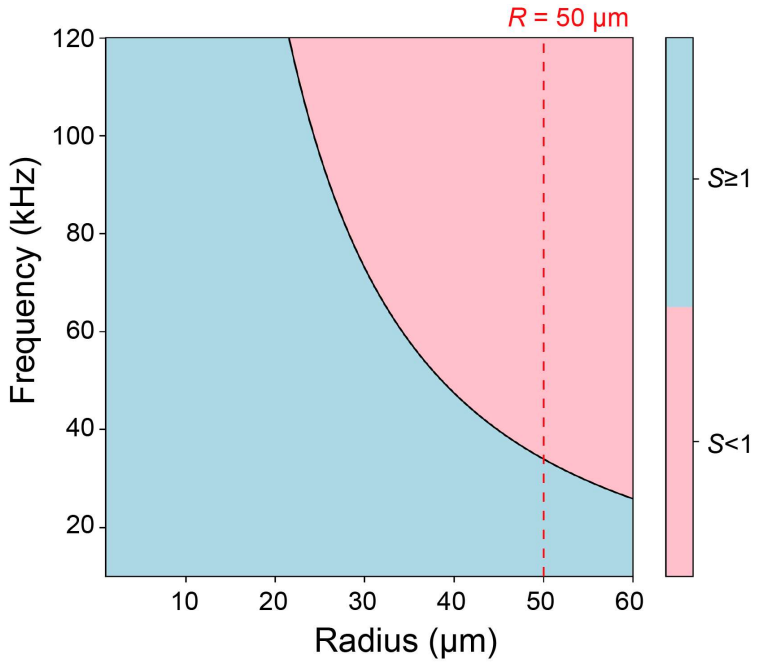

Figure 4.3. Pinch off theory plot between frequency and micro-hole radius. Only the combination of both parameter generates $S \geq 1$ can make sure the above liquid can be dispensed through the micro-hole.

To verify the theoretical results, we applied finite element method (FEM, COMSOL Multiphysics 6.0) to understand the influence of the frequency, and the geometric meshes are shown in Fig. 4.22. The vibration displacement and the fluid streamlines were simulated at the resonant frequencies of 21 kHz and 110 kHz, respectively (Fig. 4.4). At 21 kHz (Fig. 4.4a), there are three pressure nodes (PN) around the central area, and the fluid from both sides is driven towards the micro-hole area, which enables enough liquid volume to be accumulated for dispense downwards through the PZT. In contrast, at the 110 kHz (Fig. 4.4b), five PNs are formed around the centre area, and the fluid streaming generates the reverse flows from PN2 to PN1 and from PN4 to PN5. These opposite streaming movements observed inevitably weaken the flow of liquid towards the centre micro-hole and push away the fluid from the micro-

hole, leading to vibration of the liquid without ejecting the liquid downwards. This predication was also verified by the experimental results which showed that there were no droplets jetting phenomena around the frequency of f_{r_2}, but liquid jetting phenomena were found close to f_{r_1} at around 24 kHz.

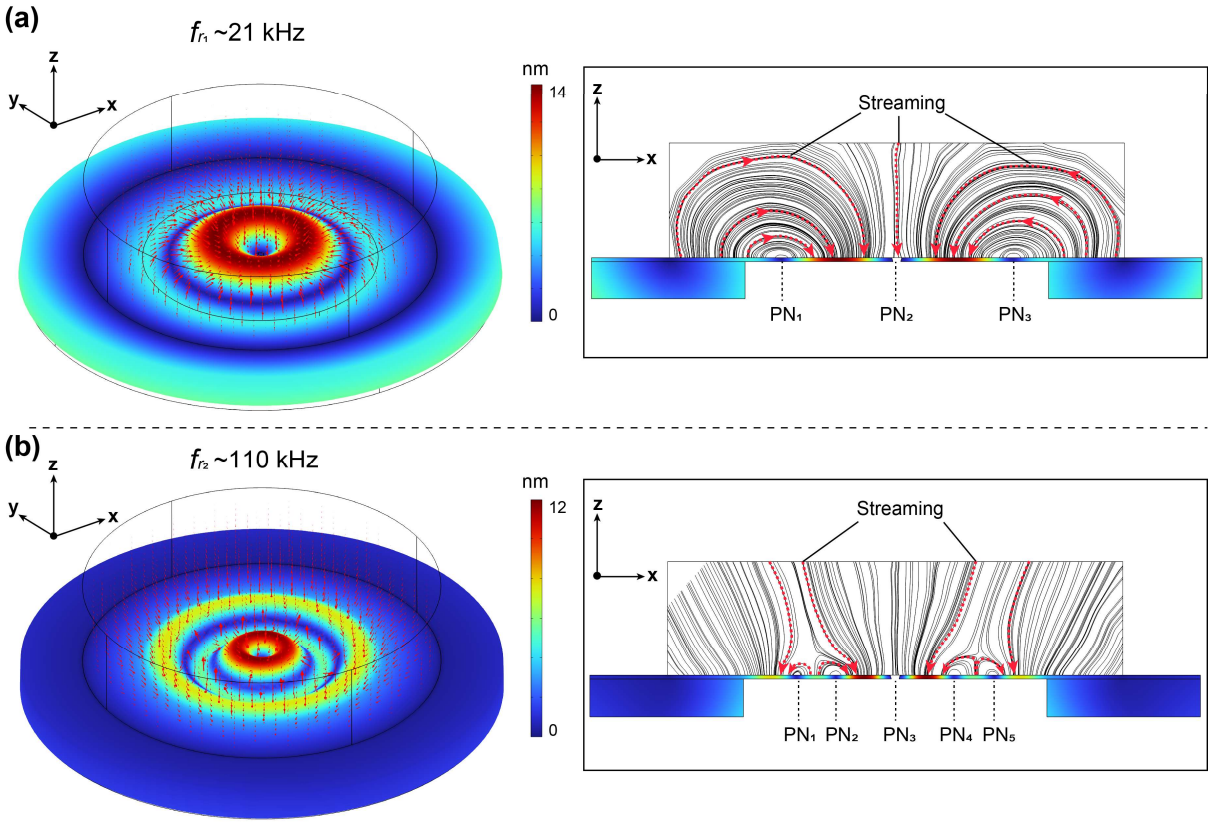

Figure 4.4. Numerical simulation of metal layer vibration and fluid streaming. (a) at f_{r_1}. (b) at f_{r_2}. The colour gradient represents the displacement magnitude, and the red dash arrows indicate the fluid streamlines.

4.2.3 Characterization of Falling Droplets and Induced Fluid Perturbation

To investigate the behaviour of impacting droplets and the induced fluid perturbation, we examined how the input voltage affects droplet dynamics across three regions of interest (ROIs): droplet jetting/falling (ROI I), impact-induced bubble-cloud formation (ROI II), and bulk streaming (ROI III), as shown in Fig. 4.5. The ADAP actuator was mounted above the container with a fixed nozzle-to-surface distance, and the droplet-driven bubble cloud formed at the interface region (ROI II), while streaming was quantified in the bulk liquid below (ROI III).

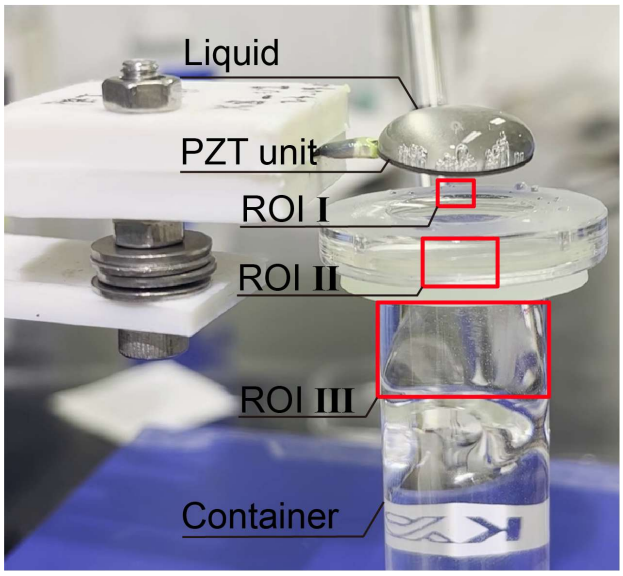

Figure 4.5. Experimental apparatus and definition of regions of interest (ROIs). The ADAP's actuator (PZT unit with micro-nozzle) is positioned above a transparent container filled with working liquid. ROI I is used to quantify droplet formation/falling, ROI II captures the droplet/film–interface region where bubbles are trapped, and ROI III is used to quantify acoustic streaming in the bulk liquid below (cross-sectional x–z imaging plane).

A high-speed camera system was built to capture droplet falling dynamics (Fig. 4.6) in the droplet jetting/falling stage (ROI I; Fig. 4.5), and representative frames are shown in Fig. 4.7a.

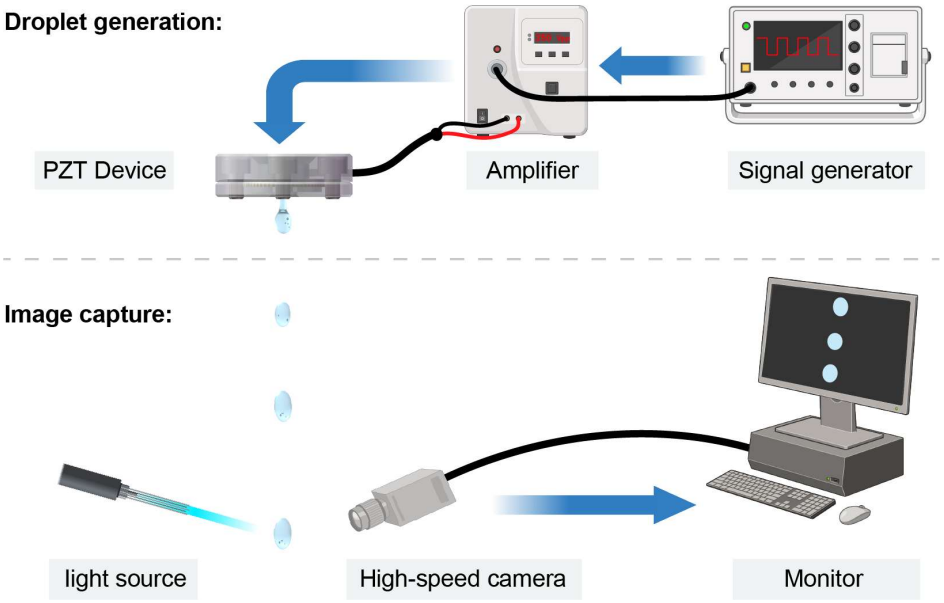

Figure 4.6. High-speed camera system for droplet falling dynamic capturing.

By increasing the input voltage, the droplet jetting velocity and droplet number were all significantly increased (Figs. 4.7c-d). As shown in Fig. 4.7b, quantitative analysis of droplet diameters revealed that at a voltage of 250 Vpp, the droplet size was significantly larger compared to those at the lower voltages (150 and 200 Vpp). Though no statistical difference was observed between 150 and 200 Vpp, the mean droplet size was slightly higher at 200 Vpp, indicating an incremental effect of voltage on droplet dimensions (Figs. 4.7b-d).

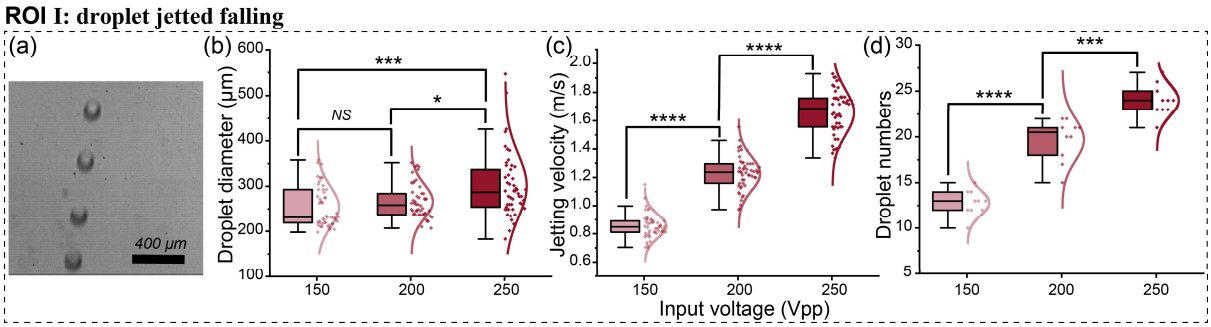

Figure 4.7. Quantification for droplet falling (ROI I). (a) Frame image capture of the falling droplets**.** (b)-(d) Quantification of the droplets' diameter, falling velocity, and numbers (20 frames) under various input voltages. (*n* = 50 in b and c, *n* = 10 in d) Scale bar: 400 μm in (a).

These experimental trends align well with the simulation results in Fig. 4.8, which show increased PZT vibration amplitude and stronger streaming intensity (red arrows) at higher input voltages.

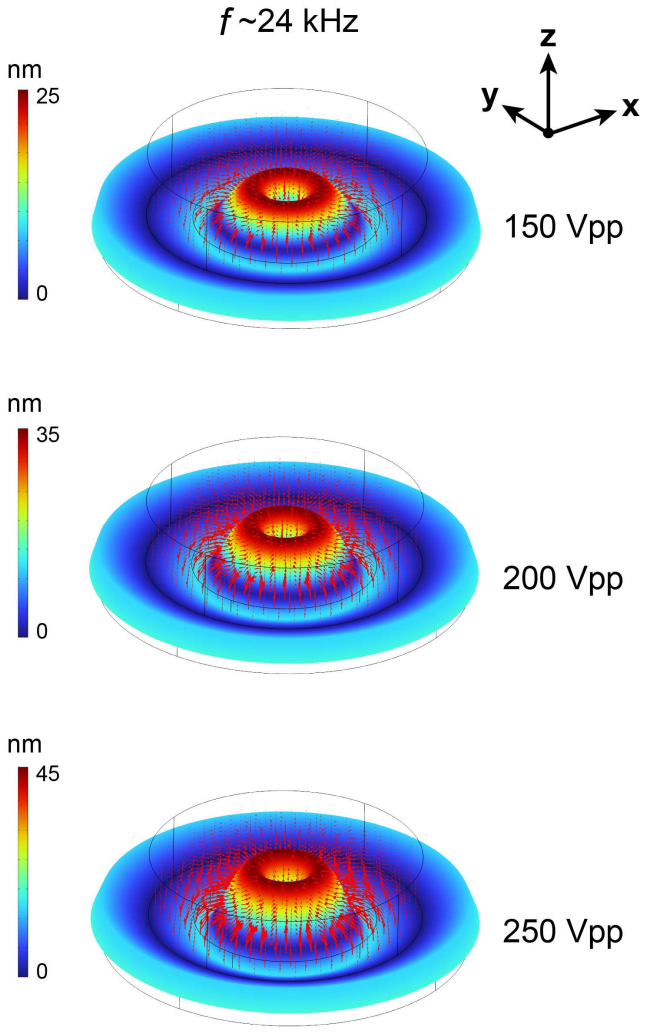

Figure 4.8. PZT vibration amplitude and above fluid streaming analysis at $f \sim 24$ kHz under various input voltages.

When a falling droplet impacts the underlying liquid layer, it first creates a concave surface indentation. As the droplet penetrates further, the concavity collapses and an air bubble can be entrained within the liquid (Fig. 4.9a). High-speed camera frames reveal clearly the transition from individual droplet into the entrapped bubbles (Fig. 4.9b).

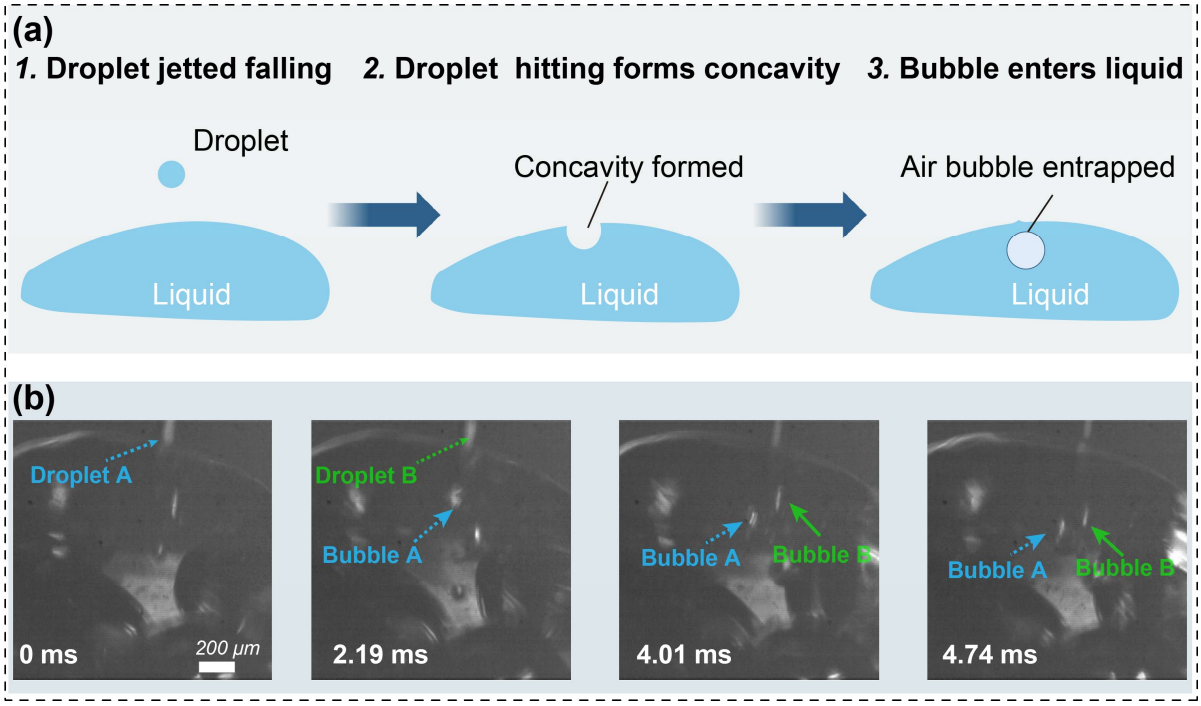

Figure 4.9. Droplets interact with the underlying liquid phase. (a) Schematic of the droplet hitting causes air bubble entrapment process. (b) Visualization of transitioning from droplets into air bubble formation in the liquid. Scale bar: 200 μm in (b).

When multiple droplets strike the liquid, they entrap more bubbles that can induce two primary liquid-dynamic effects. The first effect is dynamic air-bubble cloud formation (ROI II), in which multiple entrained bubbles are coalesced into a transient cloud. In Fig. 4.10a, the green outline marks the cloud's boundary and the inset shows how its average area is quantified. As the input voltage is increased, more droplets enter the liquid and the mean cloud size is increased significantly (Fig. 4.10b).

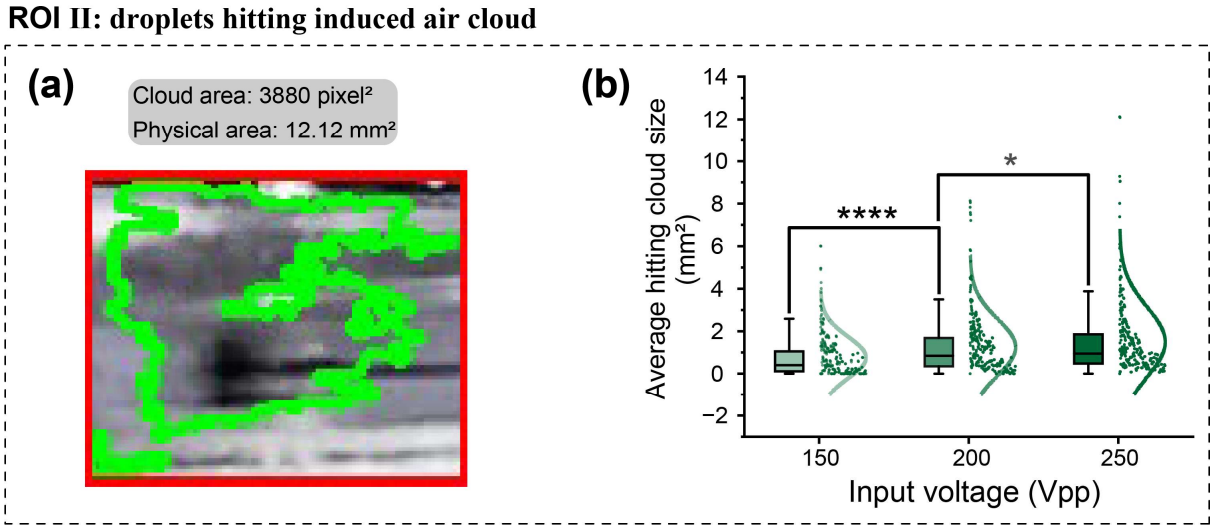

Figure 4.10. Quantification for air bubble cloud (ROI II). (a) Frame of air bubble cloud capture (green solid line). (b) The average hitting caused air cloud area at three input voltages.(*n* = 400).

The second effect is enhanced bulk streaming (ROI III), with droplet impacts increasing the streaming velocity. To quantify the streaming induced by droplet impacts, we used a transparent container filled with working liquid (seeded with tracer particles) and imaged the flow in a fixed cross-sectional plane ($x - z$) beneath the droplet–film interface (Fig. 4.5). Velocity-magnitude maps (Fig. 4.11a) were obtained using particle image velocimetry (PIV)/particle tracking on consecutive frames, and the mean streaming speed was calculated by spatially averaging the velocity magnitude over ROI III for each frame and then time-averaging over the analysed sequence (n = 200 frames per condition). Calibration: The pixel-to-distance conversion was calibrated using a stage micrometer imaged under the same optical settings, and the time base was set by the camera frame rate; together these define the absolute velocity scale (μm s^{-1}). The same calibration factors and processing settings were applied to all conditions to enable objective comparison across voltages. The same calibration factors and processing settings were applied to all conditions to enable objective comparison across voltages. We have analyzed the frame-by-frame velocity-magnitude maps (Fig. 4.11a) and calculated the average streaming speeds to reveal how the impact drives flow acceleration. As shown in Fig. 4.11b, the streaming velocity increases markedly with increasing input voltage.

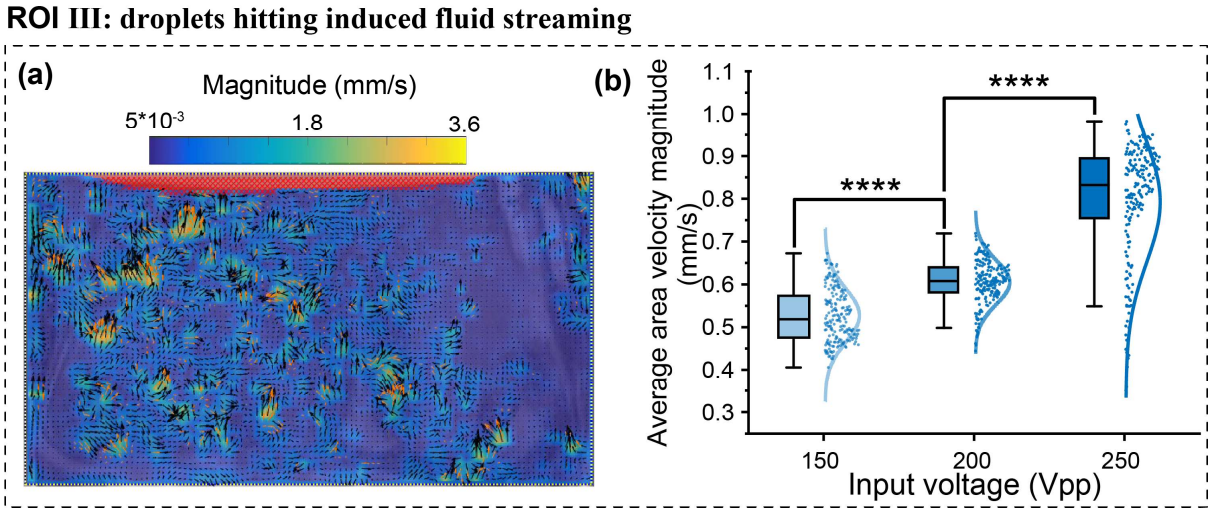

Figure 4.11. Quantification of flow streaming (ROI III). (a) Example velocity-magnitude map obtained from particle tracking/PIV. (b) Mean streaming speed (spatially averaged over ROI III and time-averaged over the analysed frames) at three input voltages. (n = 200 frames per condition). *NS*: no significance. *: $p < 0.05$, ***: $p < 0.001$, ****: $p < 0.0001$.

Taken together, these results show that increasing input voltage increases droplet generation rate and impact momentum, thereby strengthening bubble-cloud formation and bulk streaming. We hypothesise that the bubble cloud can impose localised mechanical perturbation at the skin surface, while the enhanced streaming promotes faster transport of drug molecules within the interfacial liquid layer, offering a practical means to regulate delivery rate and penetration depth.

4.2.4 Dynamic Control for *Ex-Vivo* Permeation Evaluation

We further evaluated the performance of the ADAP in enhancing transdermal permeability using *ex-vivo* mouse dorsum skin tissues. Fluorescently labelled molecules, including fluorescein sodium (NaF, 376 Da) and fluorescein isothiocyanate (FITC)-labelled dextran (10 kDa and 70 kDa), were used as the model drugs for demonstrations. After a 5-minute treatment, the skin tissues were washed twice with phosphate-buffered saline (PBS) solution to remove residual surface attached loose drug molecules, then the fluorescence signals were characterized from skin's horizontal and vertical directions (Fig. 4.12).

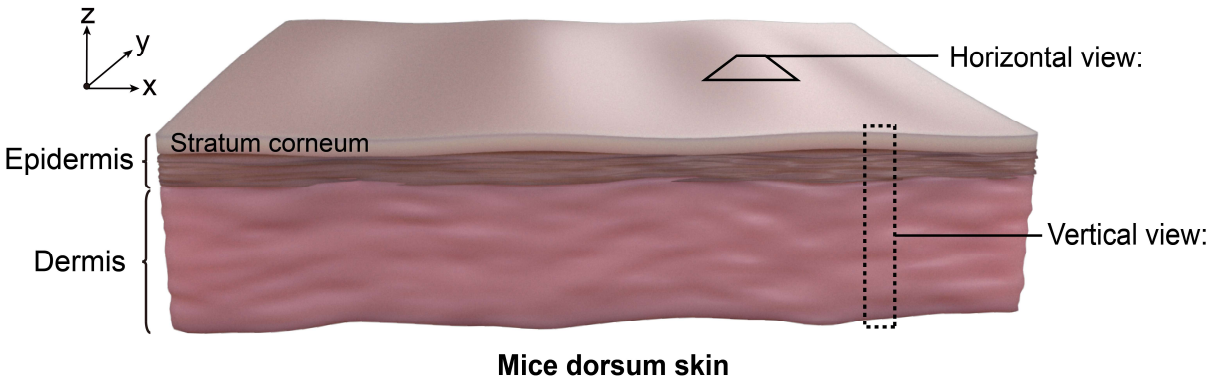

Figure 4.12. Schematic illustration of mice dorsum skin layers and two direction *ex-vivo* delivery quantifications.

Horizontal view analysis of the skin revealed that the NaF fluorescence intensity was significantly higher for the acoustic group if compared to that of the control group (i.e., passive diffusion), and the intensity of fluorescence was increased with the increase of input voltage (Fig. 4.13).

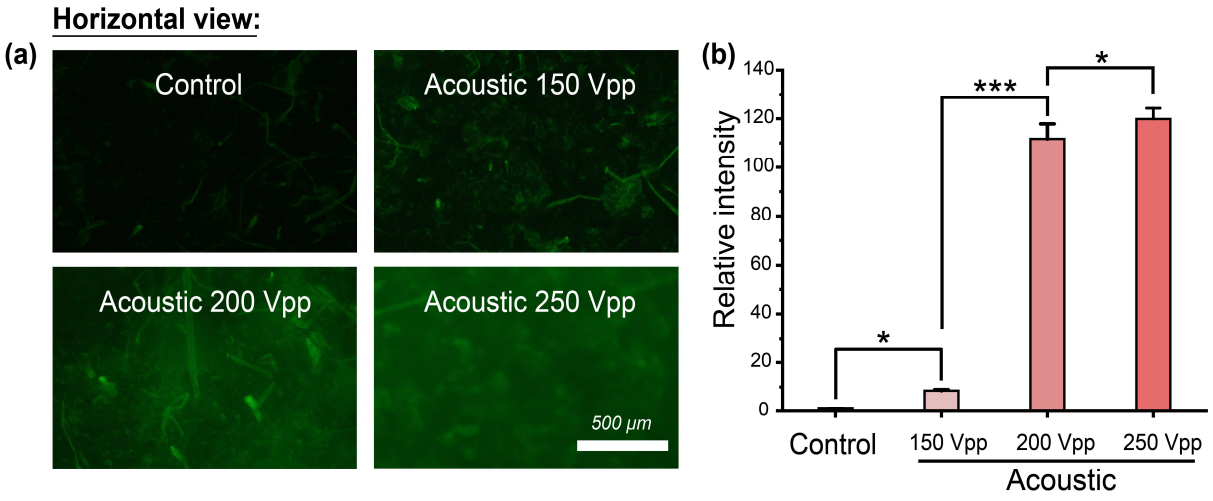

Figure 4.13. Horizontal view quantification. (a) Fluorescent microscopy images and (b) Relative fluorescence intensity under different input voltages. (n = 3). Scale bar 500 μm in (a).

Vertical cross-sectional imaging reveals that for the acoustic treatment group, there are significantly increased drug penetration depths through the SC layer into deeper skin layers. Whereas in the control group, fluorescence signals are mostly focused at the skin outermost layer (Fig. 4.14a). Quantitative analysis (Fig. 4.14b) reveals that the penetration depth in the acoustic group has reached up to around 600 μm after 5-minute ADAP treatment, if compared with those of <20 μm for the passive diffusion

control. Moreover, the relative intensity in Fig. 4.14c show that the acoustic group demonstrates an 81.7-fold fluorescent intensity enhancement than that of the control group. These results demonstrate the superior permeability enhancement achieved by ADAP, facilitating drug permeation to deeper layers of the skin and enabling access into systemic circulation for therapeutic purposes.[238]

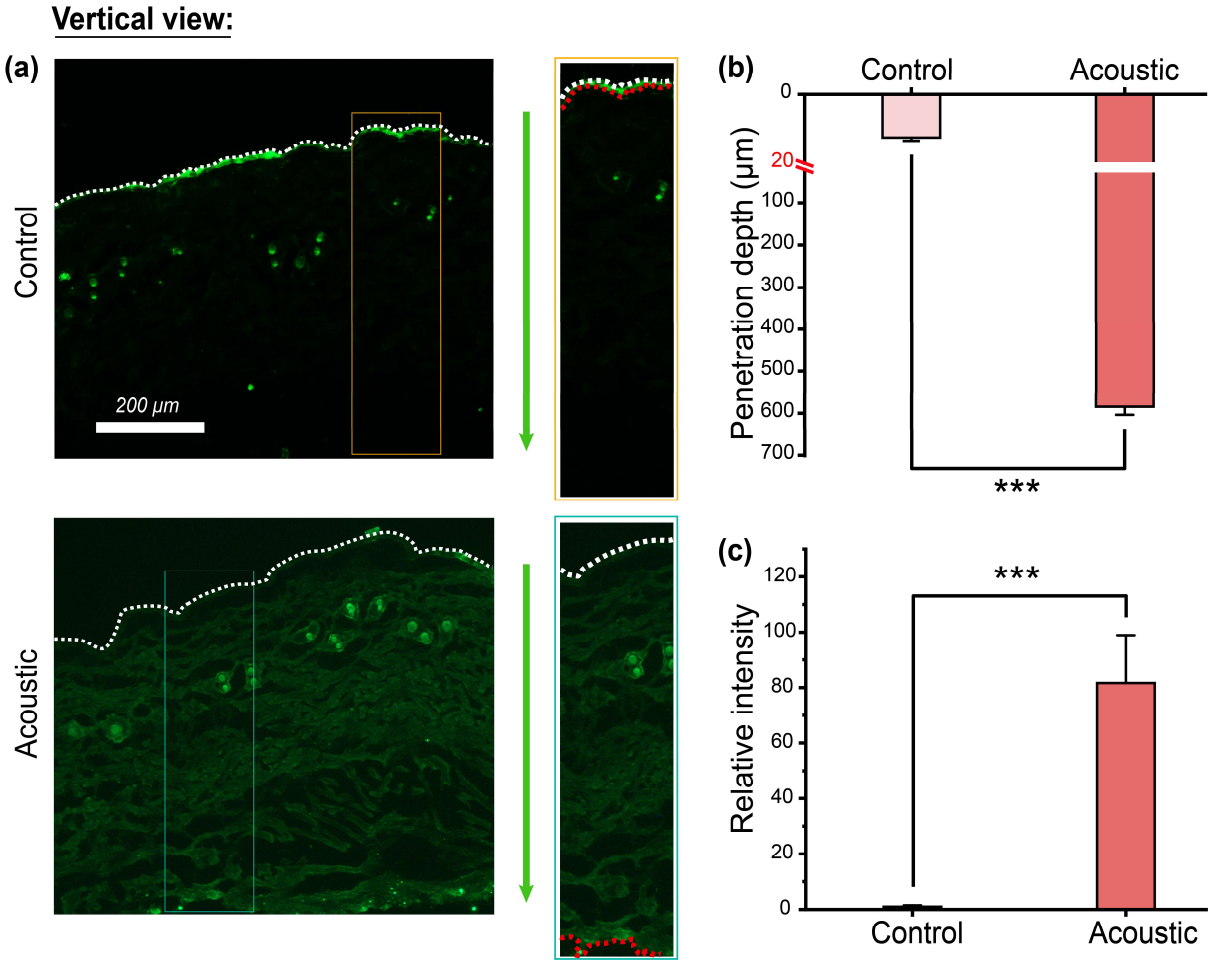

Figure 4.14. Vertical view quantification. (a) Fluorescence microscopy images showing the outermost layer of the epidermis (white dashed line) and the deepest fluorescent layer (red dashed line). (b) Penetration depth, and (c) Relative fluorescence intensity comparison between control and acoustic group. (n = 6) *: p < 0.05, ***: p < 0.001. Scale bar 200 μm in (a).

While for topical drug delivery in therapy skin disorders such as psoriasis, atopic dermatitis, actinic keratosis, and skin cancers,[239] the applied drugs aim to reach the target shallow tissue of skin to offer localized therapy.[240, 241] By adjusting the applied frequency from 23.6 kHz to 24 kHz, droplet's generation induces weaker perturbation that allows the drug delivery depths within the skin around 130 μm, as shown in Fig.

4.15. This result reveals that our device system can achieve on-demand drug penetration depth control to fulfil topical or systemic delivery.

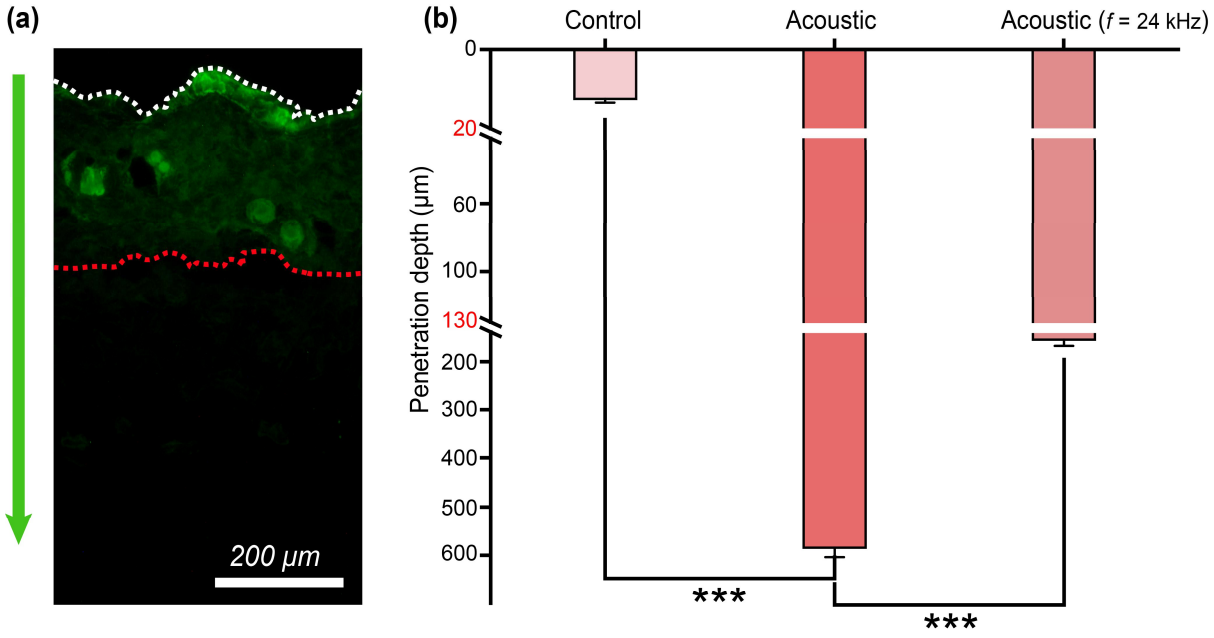

Figure 4.15. *Ex-vivo* permeation of fluorescein sodium under different frequency modes. (a) Fluorescent cross-section images of acoustic at different frequency f_2. (b) Penetration depth comparison between control and acoustic group with different frequencies. 20 and 130 μm represents the penetration of the stratum corneum and epidermis respectively. ***: $p < 0.001$. Scale bar: 200 μm.

The performance of ADAP device with two different drug molecules, i.e.,10 kDa and 70 kDa FITC-dextran, were further tested. Image analysis using the fluorescent microscopy reveals a significantly larger diffusion area and higher fluorescence intensity in the acoustic group if compared to those of the control groups (Fig. 4.16). The results of relative intensities indicate that acoustic treatment has achieved 60.7-folds and 31.2-folds improvement for 10 kDa and 70 kDa FITC-dextran, if compared with that of the control group, respectively (Fig. 4.17). Unlike most existing TDD methods, which facilitate penetration of small molecules but are unable/struggle with large-molecules, the ADAP method proved effective TDD for both 10 kDa and 70 kDa FITC-dextrans (highlighted by the red boxes in Fig. 4.16). Although the delivery efficiency for these large molecules remains lower than for small molecule like NaF (376 Da), these results suggest that further optimization of ADAP holds promising prospects for enabling efficient transdermal delivery of large-molecule therapeutics.

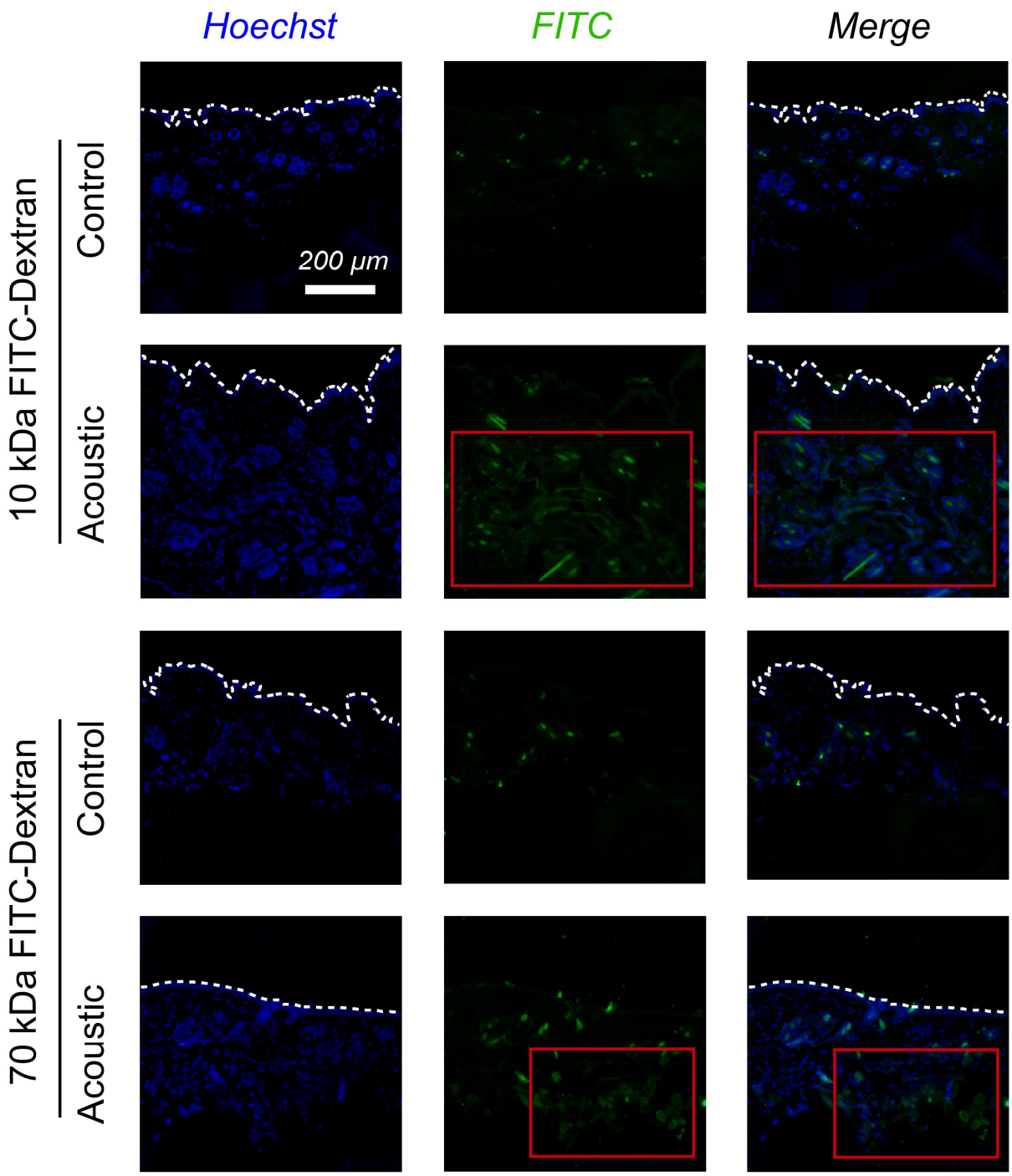

Figure 4.16. Fluorescent microscopy images of 10 kDa and 70 kD FITC-dextran between passive diffusion and acoustic group. Outermost layer of the epidermis (white dashed line), and fluorescence area (red line box) Scale bar: 200 μm.

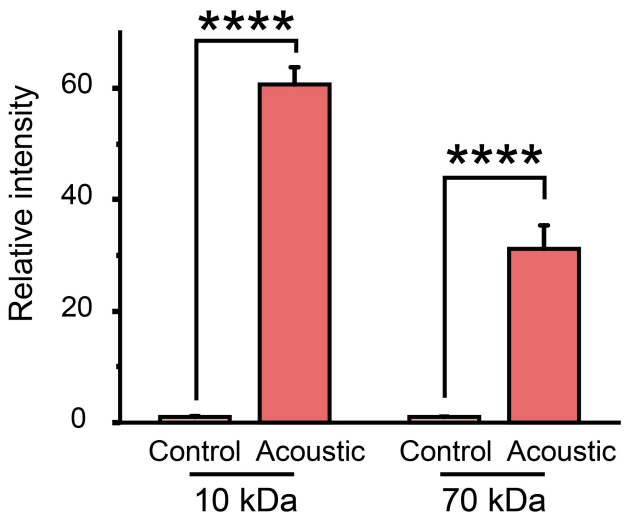

Figure 4.17. Relative fluorescence intensity comparison between control and acoustic group. (n = 3). ****: $p < 0.0001$.

In brief, all the above results collectively demonstrate that the ADAP significantly enhances TDDs compared to control-passive diffusion, offering rapid and controlled transdermal delivery capabilities for both small and macro drug molecules.

4.2.5 Transdermal Delivery of Glucose for Disease Treatment

To demonstrate efficacy of the ADAP for disease therapy, an *in-vivo* transdermal glucose delivery experiment was conducted using the hypoglycemia mice model, which was induced by fasting mice for overnight (around 16 hours) until their average blood glucose level was dropped below 70 mg/dL.[242] A 50% (*w/w*) glucose solution was then applied to the dorsum target skin, and the mice were treated for 5 minutes with either the ADAP method or with the passive diffusion control group. Blood glucose levels were measured before and after the treatment using a glucose meter (Fig. 4.18).

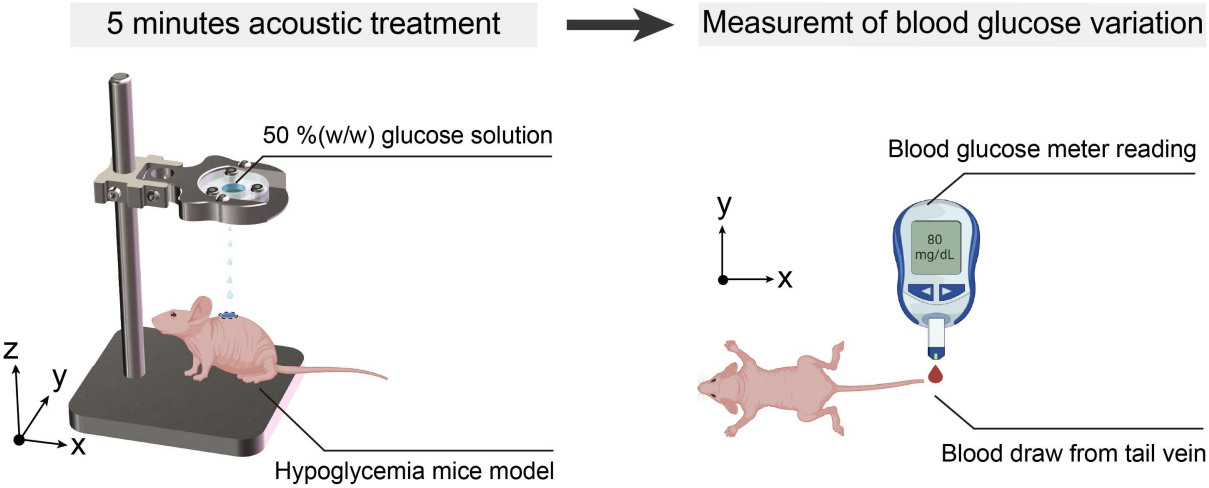

Figure 4.18. The flow chart describes the procedure for calculating and measuring blood glucose levels in mice.

As shown in Fig. 4.19, the results show that in the acoustic group, mice blood glucose levels are increased significantly after 5-minute treatment, recovering from the hypoglycemic levels to the normal ones. In contrast, the control group (with passive diffusion only) does not exhibit a similar recovery, with the glucose levels still remained in the hypoglycemic range.

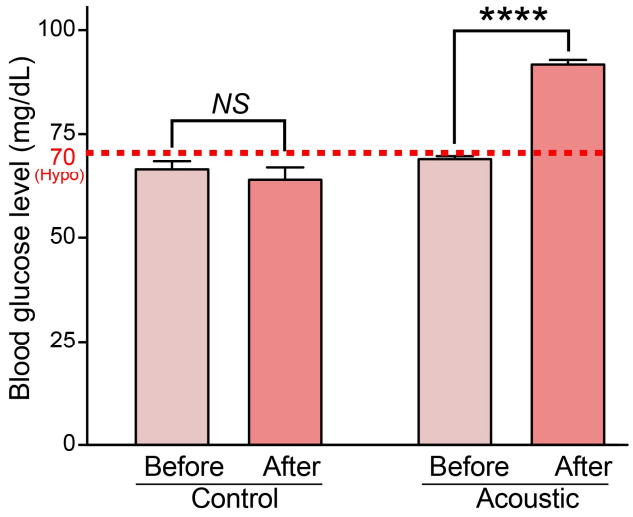

Figure 4.19. Blood glucose level variation between control and acoustic before and after 5 minutes treatment. (n = 3). Red dashed line represents the threshold of hypoglycemia. *NS*: no significance. ****: $p < 0.0001$.

We further obtained the blood glucose variations with the results listed in Table 4.1, which shows that the ADAP-treated mice experienced a 25.5 mg/dL greater rise in blood glucose level than the passive-diffusion control groups. Given that the margin

between normal glycemia and life-threatening hypoglycemia can be as narrow as 30 mg/dL,[243] this rapid correction highlights ADAP's promise for human hypoglycemia therapy. These findings demonstrate that the effective glucose administration can be achieved in just 5 minutes, thus underscoring the ADAP's major advantages for acute disease therapy. These results clearly demand the rapid and effective ADAP treatments, which the most current acoustic methods could not achieve.

Table 4.1. Glucose delivery dosage between control and acoustic group.

Number	Blood glucose level (mg/dL)		Average blood glucose variation (mg/dL)	Blood volume (ml)	Average delivery dosage (mg)
	Before	After			
Control No.1	68.8	60.2	-2.733	1.322	-0.036
Control No.2	65.4	64.8		1.292	
Control No.3	65.4	66.4		1.400	
Acoustic No.4	68.8	92.8	22.733	1.465	0.316
Acoustic No.5	69.8	91.8		1.314	
Acoustic No.6	68.4	90.6		1.387	

To assess the impact of ADAP on skin integrity, hematoxylin–eosin (H&E) staining was performed on skin sections from the control and ADAP-treated (acoustic) groups. As shown in Fig. 4.20, the acoustic group exhibits preserved tissue architecture comparable to the control, with a continuous epidermis and no visible epidermal detachment/clefting at the epidermis–dermis interface, nor obvious disruption of dermal structure at the imaging scale shown. These observations support that, under the tested operating conditions, ADAP does not produce detectable structural skin damage by routine H&E assessment, consistent with good biocompatibility. Taken together, these results indicate that ADAP is a rapid, non-invasive and effective approach for transdermal glucose delivery, with potential for patient-friendly management of acute hypoglycaemia.

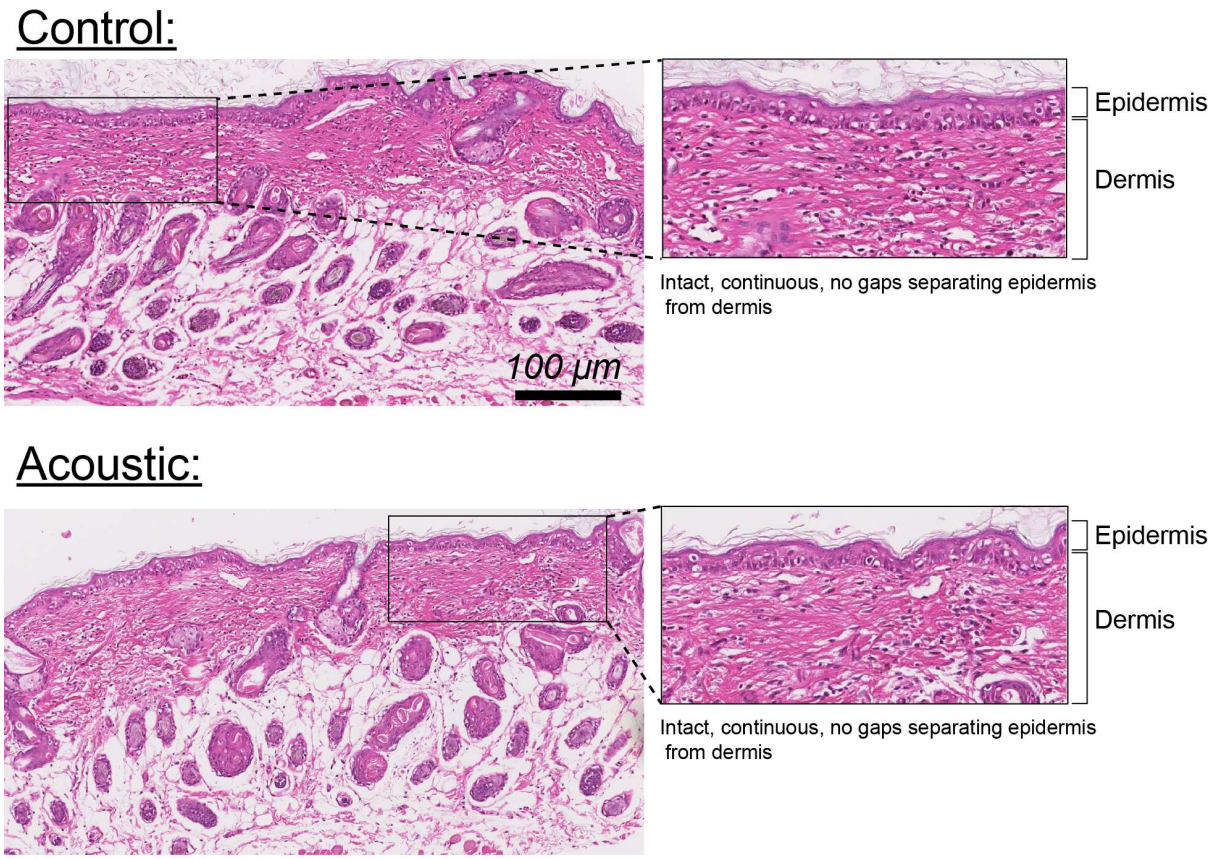

Figure 4.20. Representative H&E-stained skin sections for untreated control and ADAP-treated ("Acoustic") conditions. Insets show a magnified view of the epidermis–dermis interface from the boxed region. The conclusion of "no detectable skin damage" is based on preserved tissue architecture at the scale shown, specifically: (i) continuous surface/epidermal layer, and (ii) no visible epidermal detachment/clefting at the epidermis–dermis junction in the treated group compared with control. Scale bar: 100 μm.

4.2.6 The Vision for Using ADAP for at-Home Treatment

Based on the effective delivery, we propose to apply such the ADAP platform for home-based disease therapy, with a selected demonstration of severe hypoglycemia treatment (Fig. 4.21). For such conditions, patients are usually unconscious and are unable to eat or drink for improving their blood glucose levels, and urgently need professional first aid help (Fig. 4.21a). Herein our proposed ADAP system can non-invasively normalize their blood glucose level from severe hypoglycemia to healthy blood glucose level within several minutes (Figs. 4.21b-c). This will undoubtedly increase the timeliness of salvage and further reduce the use of healthcare resources.

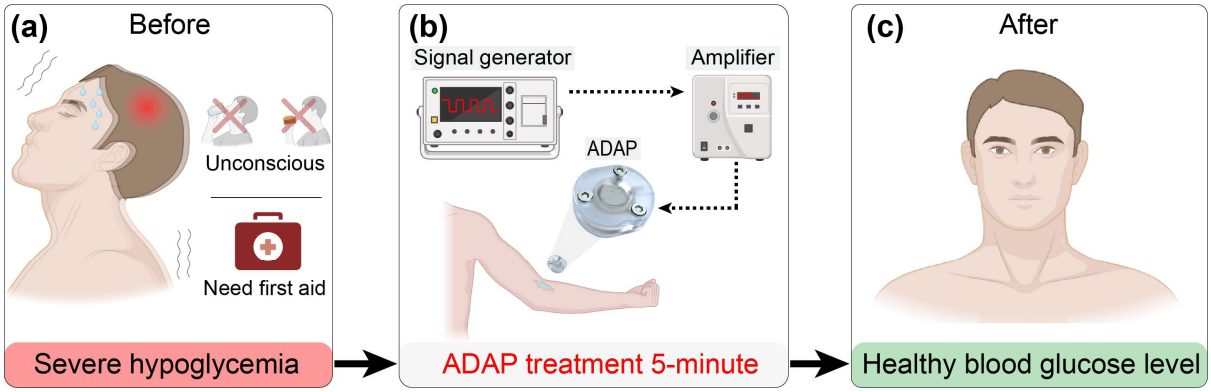

Figure 4.21. The vision for using ADAP or at-home treatment. (a) Typical symptoms for severe hypoglycemia patients. By using (b) system setup of ADAP, it can enable ultrafast transdermal delivery, which can restore blood glucose level to the (c) healthy condition.

4.3 Conclusion

In this study, we introduced a piezoelectric-transducer–driven ADAP device that transdermal delivers drugs rapidly, efficiently, and noninvasively. By tuning the input voltage, we modulated droplet-generation rate and ejection momentum thereby dynamically controlling the perturbation intensity at the skin surface. *Ex-vivo* validation with water-soluble molecules showed that the ADAP treatment achieved significant delivery enhancements over passive diffusion of ~81.7-fold for NaF, ~60.7-fold for 10 kDa FITC-dextran, and ~31.2-fold for 70 kDa FITC-dextran. Moreover, by adjusting the input voltage and actuation frequency, we were able to fine-tune TDD efficiency and penetration depth to meet diverse therapeutic needs. Finally, by performing *in-vivo* testing in hypoglycemia mice models, the ADAP treatment restored blood glucose to normal levels within 5 minutes, without notable damage to skin integrity. Together, these results demonstrate that ADAP is a versatile and tuneable platform for personalized acute-disease therapy. With further integration into a compact, all-in-one device and thorough clinical validation, the ADAP has its great potential to transform acute disease management by providing a safe, effective, and user-friendly solution for home using.

4.4 Mechanism Interpretation: Evidence vs Inference, and Alternative Explanations.

ADAP is proposed to enhance transdermal transport through interfacial droplet-impact dynamics: droplet generation and impact form an interfacial liquid film, impacts entrain air and create a transient bubble cloud at the skin surface, and subsequent oscillation of entrapped bubbles drives microstreaming and local mechanical stresses near the stratum corneum (SC), promoting deeper permeant penetration. In this chapter, droplet dynamics (ROI I), bubble-cloud formation (ROI II) and enhanced streaming (ROI III) were directly measured, and these changes coincide with increased penetration depth and fluorescence intensity for both NaF and FITC–dextran tracers. However, the precise microstructural changes within the SC layer responsible for the increased permeability (e.g., transient alteration of intercellular pathways or lipid organisation) are inferred from transport outcomes rather than directly resolved in this work.

A key alternative explanation for acoustic-enhanced delivery is inertial cavitation. Under the tested ADAP conditions, inertial cavitation is unlikely to be the dominant mechanism in the bulk liquid: no measurable bulk temperature rise was observed during treatment, and a pitting-foil test showed no detectable pits under acoustic actuation. These observations are inconsistent with sustained inertial cavitation-driven erosion as the primary cause of enhanced permeation. Two further possibilities are that enhancement arises mainly from droplet impact impulse or from surface mixing (“stirring”) that thins the external mass-transfer boundary layer; these may contribute, but the available data most consistently support a bubble-oscillation/microstreaming-driven interface perturbation. Table 4.2 summarises the alternative mechanisms considered and the experiments/observations that constrain them.

Table 4.2. Alternative mechanisms considered for ADAP-enhanced permeation and observations/experiments that constrain them.

Alternative mechanism	What would be expected if dominant	Experiments/observations in this chapter	What this indicates
Inertial cavitation–driven enhancement	Localised erosion/pitting; strong energy dissipation often accompanied by heating and mechanical damage	Pitting foil: no detectable pits under ADAP actuation; Temperature: no measurable bulk temperature rise during treatment	Unlikely to be the primary mechanism under the tested conditions
Droplet impact impulse alone (impacts mechanically "punch" drug through)	Enhancement depends only on droplet momentum/flux; bubble/streaming features not required	High-speed imaging shows droplet output increases with voltage; impacts consistently generate an interfacial bubble cloud	Impact is likely an enabler/trigger (film + bubble formation) rather than a standalone mechanism; not fully isolated here
Surface stirring thinning alone (mixing near surface increases uptake without barrier modulation)	Mainly increases surface uptake with limited deep penetration; effect largely convective	Cross-sectional imaging shows increased penetration depth, not only higher surface fluorescence	Suggests enhancement involves more than external mixing alone, consistent with interface-mediated perturbation (bubble oscillation/microstreaming)

4.5 Limitations and Practical Considerations

This chapter provides proof-of-concept evidence that ADAP can rapidly enhance ex-vivo permeation for small and macromolecular tracers and can increase blood glucose in a hypoglycaemic mouse model within a short treatment window, while showing no detectable structural skin damage by routine H&E at the imaging scale presented. Nevertheless, the mechanistic interpretation remains partially inferential: the specific stratum corneum microstructural changes responsible for the increased permeability were not directly resolved, and additional barrier/function assays (e.g., SC layer recovery, molecular inflammation markers, ultrastructure imaging) would strengthen biocompatibility and mechanism claims. The current evaluation is limited to the tested operating window, model drug conditions, and mouse skin; translation will require systematic dose–response optimisation, assessment across different skin types/thicknesses and longer-term safety, and comparison against established transdermal enhancement methods under matched dosing conditions.

4.6. Methods and Materials

4.6.1 PZT Processing and Electromechanical Characterization

The piezoelectric transducer lead zirconate titanate (PZT) unit used in ADAP device was fabricated by bonding a piezoelectric ceramic ring (600 μm thick) to a round steel disc (16 mm diameter, 50 μm thick). A micro-hole was created at the center of the steel disc using high-energy laser pulses, which burned through the metal layer in multiple cycles until perforation was achieved. To ensure smooth and clean edges, the processed metal was treated with acid washing followed by ultrasonic cleaning.[244] The resulting micro-hole exhibited a conical structure with top and bottom widths of 130 μm and 100 μm, respectively. Lead content and contamination considerations (PZT). The ADAP actuator uses a lead (Pb)–zirconate–titanate ceramic, which contains Pb and therefore warrants consideration of potential lead release/contamination. In this device, the PZT element is not in direct contact with the drug solution or skin: it is bonded to the steel disc and drives droplet ejection through the nozzle, so the treatment interface is defined by the droplets/liquid film rather than the ceramic itself. Accordingly, contamination would only be a concern if the PZT were exposed (e.g., cracking or delamination) and contacted the formulation. To mitigate this risk, the PZT was kept fully integrated within the actuator assembly, handled to avoid chipping, and inspected after use; any damaged units were discarded. For future translational

development, residual risk could be further reduced by adding an inert encapsulation/barrier layer over the PZT (or using lead-free piezo-electrics) and by performing leachate testing on post-actuation formulations to confirm negligible Pb release under operating conditions.

The electromechanical properties of the PZT unit were characterized to optimize its performance. An impedance analyzer (E4990A, Keysight Technologies) was employed to measure the electrical impedance spectrum of the PZT across a frequency range of 0 to 200 kHz. The data revealed a resonant frequency at which the impedance reached its minimum, indicative of optimal operational conditions for the device. The specifications of the PZT and the working parameters are provided in Table 4.3.

Table 4.3. Detailed working conditions of ADAP device.

<table>
<tr><td rowspan="2">Working conditions</td><td>Frequency</td><td>Wave mode</td><td>Input voltage</td><td>Treatment time</td><td>Drug loading volume</td><td>Distance (PZT to skin)</td></tr>
<tr><td>≈ 24 kHz</td><td>Square (constant)</td><td>150, 200, 250 Vpp</td><td>5 minutes</td><td>500 µL</td><td>8 mm</td></tr>
<tr><td rowspan="3">PZT unit</td><td colspan="2">Thickness</td><td colspan="2">Diameter</td><td colspan="2">Micro-hole in metal layer</td></tr>
<tr><td>Metal layer</td><td>Piezoelectric ceramic</td><td>Metal layer</td><td>Piezoelectric ceramic (hollow area)</td><td>Top</td><td>Bottom</td></tr>
<tr><td>50 µm</td><td>600 µm</td><td>16 mm</td><td>12 mm</td><td>130 µm</td><td>100 µm</td></tr>
</table>

4.6.2 Device Assembly and System Setup

The ADAP device was assembled by encapsulating the piezoelectric transducer (PZT) unit between two acrylic layers, secured with three M4 screws. A waterproof seal was

placed between the PZT and the top acrylic encapsulation to eliminate air gaps and prevent liquid leakage. The encapsulated unit was mounted onto a metal holder and attached to a vertical stand with adjustable height, allowing precise control of the PZT's position relative to the target surface (Fig. 4.22). The system setup involved connecting the PZT unit to a signal generator (123-6578, RS Pro), which produced the required RF signal. This signal was amplified using a high-voltage amplifier (HA-820A, Pintech), enabling precise control of the input voltage to the PZT. This configuration ensures efficient and reproducible generation of droplets while maintaining the structural integrity of the device during repeated use.

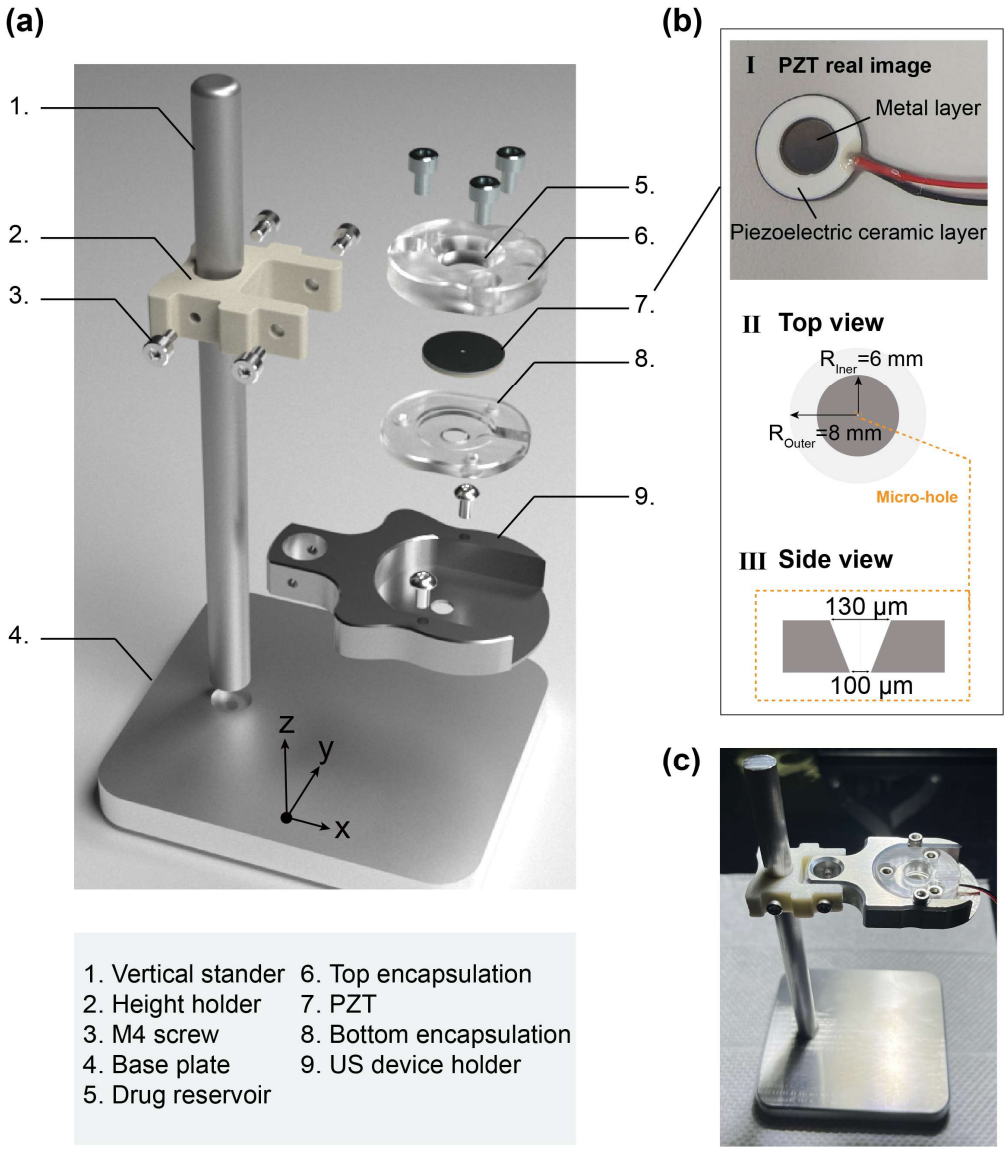

Figure 4.22. Acoustic droplets activated permeation (ADAP) device. (a) 3D exploded view of the device. (b) I: PZT real image and observation from II: top view. III: Schematic of the micro-hole from side view. (c) Real image of the ADAP device.

4.6.3 Finite Element Analysis (FEA)

To investigate the acoustofluidic field at the PZT metal surface and its above fluid, finite element analysis (FEA) was conducted using COMSOL Multiphysics 6.0. The Piezoelectricity Multiphysics and Thermoviscous Acoustics Modules were employed for this study. The model geometry consisted of Lead Zirconate Titanate (PZT-5H) plate bonded with a 50 μm thick aluminum metal layer with a cone hole in the centre (top: 130 μm, bottom: 100 μm). To simply the calculation, a liquid cylinder (radius 6 mm, height 3 mm) was place above the metal layer, where the liquid domain and its properties were defined as water. Initially, a frequency domain solution was performed to obtain the mechanical displacements of the metal layer and the acoustic pressure induced in the above liquid. These acoustic pressure values were subsequently employed in the stationary solver to solve for the acoustic pressure-induced liquid streamlines. The acoustofluidic model's geometrical meshes in this study are displayed in Fig. 4.23.

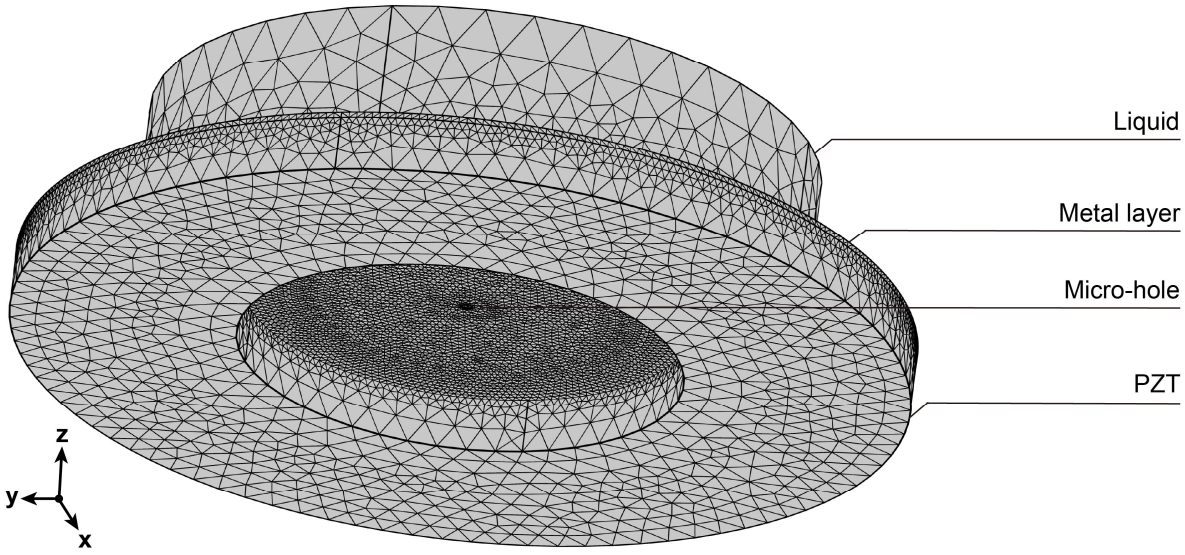

Figure 4.23. Geometric meshes in the COMSOL simulation.

4.6.4 High-Speed Imaging

The single PZT unit used in this study was held by a custom stand and filled with 500 μL DI water onto the PZT's top surface. A high-speed camera (SH6-109, SSZN) with an objective lens (4 times) was deposited focusing on a zone close to the PZT bottom surface and the underneath liquid top surface . A 150 W halogen fiber optic illumination source (MultiLED QX, Photo-Sonics International Ltd) was used to provide sufficient

illumination for high-frame-rate (27,400 fps) and low exposure time (16 μs) image capture. A millimetre scale was placed at the focal plane to calibrate the pixel size in the image for droplet size and velocity calculations. The experimental videos were recorded using a custom camera PCC software and exported to single frames for post-analysis by ImageJ (National Institutes of Health). The total pixel area under analysis was kept constant at length: 1500 μm, and width: 1500 μm. For droplet diameter quantification, the video frames were visually inspected to select in-focus droplets, and the droplet's horizontal width was measured as the droplet diameter. At each input voltage, 50 droplets were characterized. For droplet velocity characterization, single droplet was traced from entered and left the area (Fixed vertical length: 1500 μm). A trajectory was drawn and measured using the calibration scale between these points and the distance was divided by the number of frames and the duration of each frame (0.37 ms) to yield the velocity in m/s. And at each input voltage 50 droplets were measured. For the droplet numbers counting, droplets that fully passed the fixed length were manually counted during a sum stack of 20 frames, and at each input voltage 10 repeats quantification were averaged.

4.6.5 Analysis of Droplet Hitting Effects

To analyse the droplets hitting caused air entrapment cloud, ROI II was selected. A feature extraction script written in Python (Python 3.13 , Python Software Foundation) was used to capture air cloud's physical area in each frame and the average cloud size were quantified from 400 consecutive frames at each input voltage. The fluid micro-streaming were traced using MATLAB image velocimetry tool (PIVlab, MATLAB) in ROI III.[245, 246] The average area velocity magnitude were calculated based on 200 consecutive frames at each input voltage.

4.6.6 Animals

Female Bagg and Albino (BALB)/c nude mice (9~10 weeks) were purchased (BALB/c-nu, Sbefu Biotechnology Co., Ltd.) and raised under specific pathogen-free conditions. All the animal experiments were approved by the Ethics Committee of Shanghai Skin Disease Hospital (No. 2024-83) and performed in accordance with the Guidelines for Care and Use of Laboratory Animals of Tongji University.

4.6.7 *Ex-Vivo* Transdermal Permeation Evaluation

Ex-vivo transdermal permeation experiments were conducted using fresh mouse dorsum skin tissues to evaluate the effectiveness of the ADAP. Fluorescently labelled molecules, including fluorescein sodium (NaF, 376 Da, C.I. 45350, Sigma-Aldrich), and fluorescein isothiocyanate-labelled 10 kDa (FD10S, Sigma-Aldrich), and 70 kDa (90718, Sigma-Aldrich) FITC-dextran were used as model drugs. The concentrations of these molecules were 100 μg/mL for NaF and 1 mg/mL for both FITC-dextran variants. Skin tissues were excised from the BALB/c nude mice and divided into two groups, i.e., the acoustic treatment group and the control (passive diffusion) group. In the acoustic group, the ADAP was activated to apply droplets containing the fluorescent molecules onto the skin for 5 minutes. In the control group, fluorescent molecule solutions were applied passively to the skin without acoustic treatment. After treatment, the skin surfaces were thoroughly washed twice with the PBS to remove residual fluorescent molecules.

Treated skin tissues were embedded in an optimal cutting temperature (OCT) compound (KMA-0100-00A, Cellpath), frozen at -20°C, and sectioned into 10 μm slices using a cryostat (CM1950, Leica). The tissue sections were mounted on glass slides for fluorescence imaging. For samples treated with FITC-dextran, the sections were additionally stained with Hoechst nucleic acid stain (62249, Thermo Fisher Scientific) for 5 minutes to visualize nuclei, followed by washing with PBS twice. Fluorescent images of the tissue sections were captured using an inverted fluorescence phase contrast microscope (Axio Vert.A1, Zeiss). In this study, the fluorescent images were analysed using the ImageJ software (National Institutes of Health). The fluorescence intensity was measured for each image by measuring the averaged normalized fluorescence (with the control group's fluorescence intensity set as 1). The penetration depth of the NaF was measured in each tissue slice by measuring the averaged vertical distance between the outermost-layer of the epidermis (white dashed line) to the deepest fluorescence layer (red dashed line).

4.6.8 *In-Vivo* Glucose Delivery for Hypoglycemia Therapy

BALB/c nude hypoglycemia mice models were used to compare ADAP-enabled release and passive diffusion of glucose solution by measuring the mouse blood glucose level variation after 5 minutes of treatment. The hypoglycemia mice models were built via an overnight fasting of ~16 hours (i.e., no food only water feeding) until

mice had an average blood glucose level < 70 mg/dL.[242] By scaling the weights of each mouse, the mouse's total blood volume can be calculated using the equation:

$$\text{Total blood volume} = \text{Standard blood volume per gram} \times \text{Mice weight} \quad (4.2)$$

In this study, 77 μL/g was used as the standard blood volume per gram,[247, 248] and the corresponding mice's total blood volume was calculated, with the results listed in Table S2 (Supplementary Information). The 50% (w/w) glucose solution was used for the hypoglycemia therapy experiments. To measure the blood glucose level, 1 μL blood samples were drawn from the tail vein of mice using the glucose meter (CONTOUR®CARE, CONTOUR) before and after treatment. The glucose delivery dosage was calculated based on the following equation:

$$\text{Glucose delivery dosage} = \text{Mice glucose level variation} \times \text{Mice total blood volume} \quad (4.3)$$

where the mice glucose level variation was calculated by using mice's blood glucose level after treatment minus that before treatment. The delivery dosage data of each mice are listed in Table 4.4.

Table 4.4. Mice weight and corresponding total blood volume.

Standard of total blood volume of mice: 77 μL/g			
Category	Number	Weight (g)	Blood volume (mL)
Control	No.1	17.17	1.322
	No.2	16.78	1.292
	No.3	18.18	1.400
Acoustic	No.4	19.2	1.465
	No.5	17.07	1.314
	No.6	18.1	1.387

4.6.9 Biocompatibility Analysis

To evaluate the impact of acoustic influence on the skin integrity, tissue samples with acoustic treatment and passive diffusion (control) were excised and fixed in 4% paraformaldehyde (PFA) for 24 hours before histological processing. After fixing, skin samples were embedded with paraffin, processed by hematoxylin-eosin (HE) staining, and cut into cross-section slices with a thickness of 5 μm. Slides were then imaged using the slide scanner (Axioscan 7, ZEISS).

4.6.10 Statistical Analysis

One-way ANOVA with Tukey (normally distributed) or Kruskal-Wallis tests (non-normally distributed) were performed to evaluate the statistical significance of differences. *, **, ***, and **** indicate $p < 0.05$, 0.01, 0.001, and 0.0001 between the conditions, respectively, and *NS* indicates statistically no significant difference between the conditions. All statistical results were plotted using Origin (Origin 2024, OriginLab).

Chapter 5: Conclusion and Outlook

5.1 Summary

In this thesis, we have developed two acoustofluidic devices applied to manipulation at the cell and tissue levels for different biomedical applications. In chapter 3, we presented a SAW-based acoustofluidic device—MARC for cell rotation manipulation. Our cell-level targets are suspension cells, where traditional cytopathology detection through cell morphology quantifications is limited to 2D microscopy observation, that may cause missing diagnostic information. The MARC system enables in-situ cell rotation in a controllable, precise, and high-throughput manner for multi-view observations. Using MARC enhances cellular morphology analysis through comprehensive, multi-view/angle views and amplifies subtle cell differences, particularly in the nuclear-to-cytoplasmic ratio, across various cell types and between cancerous and normal tissue cells. We further propose prioritizing MARC-screened positive cases to streamline traditional cytopathology and reduce workload/resources spent on negative diagnoses—an advancement that enhances overall diagnostic efficiency and offers a transformative vision for cytopathological screening. After demonstrating successful cell-level manipulation, we moved to larger-scale manipulation to address biomedical questions at the tissue level. Our targets are skin tissues, where the SC layer has low permeability. Since tissues are composed of cells with intercellular connections, they cannot be manipulated like single cells. Therefore, in chapter 4, we developed a BAW-based acoustofluidic device—ADAP to indirectly manipulate (i.e., perturb) skin tissues. By dispensing microdroplets onto the skin surface, ADAP induces intensive perturbation that increases SC permeability. Adjusting input voltage and applied frequency allows precise control over perturbation intensity, achieving different transdermal delivery efficiencies and penetration depths for various therapeutic demands. Further tests with drug models of different molecular weights show that ADAP-enhanced permeability is significantly more effective than passive diffusion. Finally, *in-vivo* treatment of glucose in a hypoglycemic mouse model demonstrated ultrafast (5-minute) delivery for restoring blood glucose level in a completely non-invasive manner.

5.2 Future Work

In this thesis, SAW-based and BAW-based acoustofluidic devices have been built to achieve manipulation from the cell level to the tissue level for applications in cytopathological screening and non-invasive transdermal drug delivery. However, these technologies only open the door for certain applications; there are additional promising opportunities that can be pursued. In the following, we discuss potential work that can build on this thesis.

In Chapter 3, we developed MARC, which enables cells to pattern in two traces and rotate in-situ within the microchannel. This capability appears useful for boosting sperm motility, since sperm naturally swim forward via spiral motion. Using MARC, sperm cells will be forced to pattern in line and rotate, which may help them recover motility in line with their natural motion habits. In addition, cytomorphology parameter quantification in the current MARC system relies on ImageJ with manual selection, which is extremely labour-intensive for large cell populations. Therefore, in the future, the MARC device should be integrated with advanced AI imaging to achieve automatic morphology capture and quantification. In this way, we could introduce a flowing fluid to inject the sample liquid, enabling higher-throughput quantification and directly delivering a more accurate disease diagnosis report.

In Chapter 4, we built the ADAP device, which achieves effective and non-invasive transdermal drug delivery. Traditional transdermal delivery methods are either invasive or cause a temperature increase on the skin; therefore, they are not suitable for sensitive-skin users. By contrast, the ADAP method is not only non-invasive but also does not generate heat, making it promising for delivering beauty products or drugs to sensitive skin. Furthermore, since ADAP shows better delivery efficiency for small drugs than for large drugs, it can be further integrated with microneedles to form a versatile transdermal delivery platform—using ADAP alone for small molecules and combining ADAP with microneedles for large molecules.

Beyond these potential applications, we note two common issues in acoustofluidic devices: (1) The operating system consists of many individual components—typically a signal generator, an amplifier, the acoustic actuator, and a sample container—which is inconvenient for ease of use and hinders full commercialization. (2) There is a lack of standardized protocols to ensure consistent and reproducible performance across

laboratories, meaning that only experienced operators can run the systems and troubleshoot issues. In the future, we will aim to integrate the components into an all-in-one device and establish clear, simple protocols so that anyone can easily operate our acoustofluidic devices to aid their research.

Bibliography

1. Ding X*, et al.* On-chip manipulation of single microparticles, cells, and organisms using surface acoustic waves. *Proc Natl Acad Sci U S A* **109**, 11105-11109 (2012).

2. Liu Y*, et al.* Manipulation with sound and vibration: A review on the micromanipulation system based on sub-MHz acoustic waves. *Ultrasonics sonochemistry* **96**, 106441 (2023).

3. Essiambre R-J. Arthur ashkin: father of the optical tweezers. *Proceedings of the National Academy of Sciences* **118**, e2026827118 (2021).

4. Ashkin A. Acceleration and trapping of particles by radiation pressure. *Physical review letters* **24**, 156 (1970).

5. Berkowitz R. Father of optical trapping awarded a share of the Nobel Prize in Physics. *Physics Today* **71**, 14-17 (2018).

6. Grier DG. A revolution in optical manipulation. *Nature* **424**, 810-816 (2003).

7. Ganim Z*, et al.* Mechanically switching single-molecule fluorescence of GFP by unfolding and refolding. *Proceedings of the National Academy of Sciences* **114**, 11052-11056 (2017).

8. Patrick EM*, et al.* Observation of processive telomerase catalysis using high-resolution optical tweezers. *Nature Chemical Biology* **16**, 801-809 (2020).

9. Han YL*, et al.* Cell contraction induces long-ranged stress stiffening in the extracellular matrix. *Proceedings of the National Academy of Sciences* **115**, 4075-4080 (2018).

10. Wu Y*, et al.* Dynamics analysis and motion planning for automated cell transportation with optical tweezers. *IEEE/ASME Transactions on Mechatronics* **18**, 706-713 (2012).

11. Xie M*, et al.* Out-of-plane rotation control of biological cells with a robot-tweezers manipulation system for orientation-based cell surgery. *Ieee Transactions on Biomedical Engineering* **66**, 199-207 (2018).

12. Suresh S*, et al.* Connections between single-cell biomechanics and human disease states: gastrointestinal cancer and malaria. *Acta Biomaterialia* **1**, 15-30 (2005).

13. Pohl HA. The motion and precipitation of suspensoids in divergent electric fields. *Journal of applied Physics* **22**, 869-871 (1951).

14. Voldman J. Electrical forces for microscale cell manipulation. *Annu Rev Biomed Eng* **8**, 425-454 (2006).

15. Fan D*, et al.* Subcellular-resolution delivery of a cytokine through precisely manipulated nanowires. *Nature nanotechnology* **5**, 545-551 (2010).

16. Nadappuram BP*, et al.* Nanoscale tweezers for single-cell biopsies. *Nature nanotechnology* **14**, 80-88 (2019).

17. Cheung K*, et al.* Impedance spectroscopy flow cytometry: On-chip label-free cell differentiation. *Cytometry Part A* **65**, 124-132 (2005).

18. Wu C*, et al.* A planar dielectrophoresis-based chip for high-throughput cell pairing. *Lab on a Chip* **17**, 4008-4014 (2017).

19. Huang L*, et al.* 3D cell electrorotation and imaging for measuring multiple cellular biophysical properties. *Lab on a Chip* **18**, 2359-2368 (2018).

20. Vahey MD*, et al.* An equilibrium method for continuous-flow cell sorting using dielectrophoresis. *Analytical Chemistry* **80**, 3135-3143 (2008).

21. Kang Y*, et al.* DC-Dielectrophoretic separation of biological cells by size. *Biomedical Microdevices* **10**, 243-249 (2008).

22. Kirschbaum M*, et al.* Highly controlled electrofusion of individually selected cells in dielectrophoretic field cages. *Lab on a Chip* **12**, 443-450 (2012).

23. Crick FH*, et al.* The physical properties of cytoplasm: A study by means of the magnetic particle method Part I. Experimental. *Experimental Cell Research* **1**, 37-80 (1950).

24. De Vlaminck I*, et al.* Recent advances in magnetic tweezers. *Annual review of biophysics* **41**, 453-472 (2012).

25. Neuman KC*, et al.* Single-molecule force spectroscopy: optical tweezers, magnetic tweezers and atomic force microscopy. *Nature Methods* **5**, 491-505 (2008).

26. Liu JF*, et al.* Use of magnetic fields and nanoparticles to trigger drug release and improve tumor targeting. *Wiley Interdisciplinary Reviews: Nanomedicine and Nanobiotechnology* **11**, e1571 (2019).

27. Wang X*, et al.* Magnetic measurement and stimulation of cellular and intracellular structures. *ACS Nano* **14**, 3805-3821 (2020).

28. Strick TR*, et al.* Single-molecule analysis of DNA uncoiling by a type II topoisomerase. *Nature* **404**, 901-904 (2000).

29. Mosconi F*, et al.* Measurement of the torque on a single stretched and twisted DNA using magnetic tweezers. *Physical review letters* **102**, 078301 (2009).

30. Tapia-Rojo R*, et al.* Single-molecule magnetic tweezers to probe the equilibrium dynamics of individual proteins at physiologically relevant forces and timescales. *Nature Protocols* **19**, 1779-1806 (2024).

31. Quintana-Cataño CA*, et al.* Magnetic tweezers to capture the fast-folding λ6-85 in slow motion. *Communications Physics* **8**, 13 (2025).

32. Vieira G*, et al.* Magnetic wire traps and programmable manipulation of biological cells. *Physical review letters* **103**, 128101 (2009).

33. Bonakdar N*, et al.* Mechanical plasticity of cells. *Nature Materials* **15**, 1090-1094 (2016).

34. Wong DW*, et al.* Interplay of cell death signaling pathways mediated by alternating magnetic field gradient. *Cell death discovery* **4**, 49 (2018).

35. Coulter WH. Means for counting particles suspended in a fluid.). Google Patents (1953).

36. Bonner W*, et al.* Fluorescence activated cell sorting. *Review of Scientific Instruments* **43**, 404-409 (1972).

37. Huber D*, et al.* Hydrodynamics in cell studies. *Chemical Reviews* **118**, 2042-2079 (2018).

38. Liu C*, et al.* Sheathless focusing and separation of diverse nanoparticles in viscoelastic solutions with minimized shear thinning. *Analytical Chemistry* **88**, 12547-12553 (2016).

39. Choi S*, et al.* Hydrophoretic sorting of micrometer and submicrometer particles using anisotropic microfluidic obstacles. *Analytical Chemistry* **81**, 50-55 (2009).

40. Huang LR*, et al.* Continuous particle separation through deterministic lateral displacement. *Science* **304**, 987-990 (2004).

41. Anene-Nzelu CG*, et al.* Scalable alignment of three-dimensional cellular constructs in a microfluidic chip. *Lab on a Chip* **13**, 4124-4133 (2013).

42. Sim WY*, et al.* A pneumatic micro cell chip for the differentiation of human mesenchymal stem cells under mechanical stimulation. *Lab on a Chip* **7**, 1775-1782 (2007).

43. Geislinger T*, et al.* Separation of blood cells using hydrodynamic lift. *Applied physics letters* **100**, (2012).

44. Tanyeri M*, et al.* Hydrodynamic trap for single particles and cells. *Applied physics letters* **96**, (2010).

45. Skelley AM*, et al.* Microfluidic control of cell pairing and fusion. *Nature Methods* **6**, 147-152 (2009).

46. Gossett DR*, et al.* Hydrodynamic stretching of single cells for large population mechanical phenotyping. *Proceedings of the National Academy of Sciences* **109**, 7630-7635 (2012).

47. Shelby JP*, et al.* A microfluidic model for single-cell capillary obstruction by Plasmodium falciparum-infected erythrocytes. *Proceedings of the National Academy of Sciences* **100**, 14618-14622 (2003).

48. Wu J. Acoustical tweezers. *The Journal of the Acoustical Society of America* **89**, 2140-2143 (1991).

49. Guo F*, et al.* Three-dimensional manipulation of single cells using surface acoustic waves. *Proc Natl Acad Sci U S A* **113**, 1522-1527 (2016).

50. Sitters G*, et al.* Acoustic force spectroscopy. *Nature Methods* **12**, 47-50 (2015).

51. Nele V*, et al.* Ultrasound-triggered enzymatic gelation. *Advanced Materials* **32**, 1905914 (2020).

52. Li D*, et al.* Scalable acoustic virtual stirrer for enhanced interfacial enzymatic nucleic acid reactions. *Science Advances* **11**, eadt6955 (2025).

53. Chen Y*, et al.* Exosome detection via the ultrafast-isolation system: EXODUS. *Nature Methods* **18**, 212-218 (2021).

54. Dumčius P*, et al.* Dual-Wave Acoustofluidic Centrifuge for Ultrafast Concentration of Nanoparticles and Extracellular Vesicles. *Small* **19**, 2300390 (2023).

55. Ning S*, et al.* A microfluidic chip with a serpentine channel enabling high-throughput cell separation using surface acoustic waves. *Lab Chip* **21**, 4608-4617 (2021).

56. Wu F*, et al.* An Enhanced Tilted-Angle Acoustofluidic Chip for Cancer Cell Manipulation. *IEEE Electron Device Letters* **42**, 577-580 (2021).

57. Sun C*, et al.* Acoustically Accelerated Neural Differentiation of Human Embryonic Stem Cells. *Acta Biomaterialia* **151**, 333-345 (2022).

58. Farooq U*, et al.* Cell lysis induced by nanowire collision based on acoustic streaming using surface acoustic waves. *Sensors and Actuators B: Chemical* **345**, 130335 (2021).

59. Wang Z*, et al.* Cell lysis via acoustically oscillating sharp edges. *Lab Chip* **19**, 4021-4032 (2019).

60. Vidler C*, et al.* Dynamic interface printing. *Nature* **634**, 1096-1102 (2024).

61. Armstrong JPK*, et al.* Engineering Anisotropic Muscle Tissue using Acoustic Cell Patterning. *Advanced Materials* **30**, 1802649 (2018).

62. Shi M*, et al.* Acoustic holographic assembly of cell-dense tissue constructs. *Biofabrication* **17**, 035009 (2025).

63. Xu J*, et al.* Acoustic metamaterials-driven transdermal drug delivery for rapid and on-demand management of acute disease. *Nature Communications* **14**, 869 (2023).

64. Wang K*, et al.* Open source board based acoustofluidic transwells for reversible disruption of the blood–brain barrier for therapeutic delivery. *Biomaterials Research* **27**, 69 (2023).

65. Athanassiadis AG*, et al.* Ultrasound-responsive systems as components for smart materials. *Chemical Reviews* **122**, 5165-5208 (2021).

66. Maresca D*, et al.* Biomolecular ultrasound and sonogenetics. *Annual review of chemical and biomolecular engineering* **9**, 229-252 (2018).

67. Wu MC. Optoelectronic tweezers. *Nature Photonics* **5**, 322-324 (2011).

68. Borchers S*, et al.* Direct electrical stimulation of human cortex—the gold standard for mapping brain functions? *Nature Reviews Neuroscience* **13**, 63-70 (2012).

69. Melde K*, et al.* Ultrasound-assisted tissue engineering. *Nature Reviews Bioengineering* **2**, 486-500 (2024).

70. Jin Y*, et al.* Magnetic control of axon navigation in reprogrammed neurons. *Nano Letters* **19**, 6517-6523 (2019).

71. Yun S*, et al.* Design of magnetically labeled cells (Mag-Cells) for in vivo control of stem cell migration and differentiation. *Nano Letters* **18**, 838-845 (2018).

72. Kappes M*, et al.* Superparamagnetic iron oxide nanoparticles for targeted cell seeding: magnetic patterning and magnetic 3D cell culture. *Advanced Functional Materials* **32**, 2203672 (2022).

73. Ozcelik A*, et al.* Acoustic tweezers for the life sciences. *Nat Methods* **15**, 1021-1028 (2018).

74. Ding X*, et al.* Tunable patterning of microparticles and cells using standing surface acoustic waves. *Lab on a Chip* **12**, 2491-2497 (2012).

75. Dholakia K*, et al.* Comparing acoustic and optical forces for biomedical research. *Nature Reviews Physics* **2**, 480-491 (2020).

76. Collins DJ*, et al.* Two-dimensional single-cell patterning with one cell per well driven by surface acoustic waves. *Nature Communications* **6**, 8686 (2015).

77. Shi J*, et al.* Acoustic tweezers: patterning cells and microparticles using standing surface acoustic waves (SSAW). *Lab on a Chip* **9**, 2890-2895 (2009).

78. Xu M*, et al.* Programmable Acoustic Holography using Medium-Sound-Speed Modulation. *Advanced Science* **10**, 2301489 (2023).

79. Xu M*, et al.* Sound-Speed Modifying Acoustic Metasurfaces for Acoustic Holography. *Advanced Materials* **35**, 2208002 (2023).

80. Tung K-W*, et al.* Deep, sub-wavelength acoustic patterning of complex and non-periodic shapes on soft membranes supported by air cavities. *Lab on a Chip* **19**, 3714-3725 (2019).

81. Melde K*, et al.* Acoustic Fabrication via the Assembly and Fusion of Particles. *Advanced Materials* **30**, 1704507 (2018).

82. Ma Z*, et al.* Acoustic Holographic Cell Patterning in a Biocompatible Hydrogel. *Advanced Materials* **32**, 1904181 (2020).

83. Melde K*, et al.* Holograms for acoustics. *Nature* **537**, 518-522 (2016).

84. Tang T*, et al.* Rotation of Biological Cells: Fundamentals and Applications. *Engineering* **4**, 1600205 (2021).

85. Läubli NF*, et al.* 3D Manipulation and Imaging of Plant Cells using Acoustically Activated Microbubbles. *Small Methods* **3**, 1800527 (2019).

86. Ahmed D*, et al.* Rotational manipulation of single cells and organisms using acoustic waves. *Nature Communications* **7**, 11085 (2016).

87. Zhu J*, et al.* High-throughput acoustofluidic microchannels for single cell rotation. *Journal of Micromechanics and Microengineering* **31**, 124004 (2021).

88. Läubli NF*, et al.* Embedded Microbubbles for Acoustic Manipulation of Single Cells and Microfluidic Applications. *Analytical Chemistry* **93**, 9760-9770 (2021).

89. Ozcelik A*, et al.* Acoustofluidic Rotational Manipulation of Cells and Organisms Using Oscillating Solid Structures. *Small* **12**, 5120-5125 (2016).

90. Feng L*, et al.* On-chip rotational manipulation of microbeads and oocytes using acoustic microstreaming generated by oscillating asymmetrical microstructures. *Biomicrofluidics* **13**, 064103 (2019).

91. Kvåle Løvmo M*, et al.* Ultrasound-induced reorientation for multi-angle optical coherence tomography. *Nature Communications* **15**, 2391 (2024).

92. Schwarz T*, et al.* Rotation of non-spherical micro-particles by amplitude modulation of superimposed orthogonal ultrasonic modes. *The Journal of the Acoustical Society of America* **133**, 1260-1268 (2013).

93. Chen C*, et al.* Acoustofluidic rotational tweezing enables high-speed contactless morphological phenotyping of zebrafish larvae. *Natue Communications* **12**, 1118 (2021).

94. Zhang J*, et al.* Surface acoustic waves enable rotational manipulation of Caenorhabditis elegans. *Lab on a Chip* **19**, 984-992 (2019).

95. Yu C-C*, et al.* A Conformable Ultrasound Patch for Cavitation-Enhanced Transdermal Cosmeceutical Delivery. *Advanced Materials* **n/a**, 2300066 (2023).

96. Li S*, et al.* Stretchable Electronic Facial Masks for Sonophoresis. *ACS Nano* **16**, 5961-5974 (2022).

97. Soto F*, et al.* Noninvasive Transdermal Delivery System of Lidocaine Using an Acoustic Droplet-Vaporization Based Wearable Patch. *Small* **14**, 1803266 (2018).

98. Chen Z*, et al.* A piezoelectric-driven microneedle platform for skin disease therapy. *The Innovation* **5**, 100621 (2024).

99. Rezai AR*, et al.* Ultrasound Blood–Brain Barrier Opening and Aducanumab in Alzheimer's Disease. *New England Journal of Medicine* **390**, 55-62 (2024).

100. Sonabend AM*, et al.* Repeated blood–brain barrier opening with an implantable ultrasound device for delivery of albumin-bound paclitaxel in patients with recurrent glioblastoma: a phase 1 trial. *The Lancet Oncology* **24**, 509-522 (2023).

101. Zhang X*, et al.* Surface Acoustic Wave-Enhanced Multi-View Acoustofluidic Rotation Cytometry (MARC) for Pre-Cytopathological Screening. *Advanced Science* **11**, 2403574 (2024).

102. Answer: Chinese Brass Water-Spouting Bowl. *Isis* **72**, 86-88 (1981).

103. Rufo J*, et al.* Acoustofluidics for biomedical applications. *Nature Reviews Methods Primers* **2**, 30 (2022).

104. Beranek L*, et al. Acoustics: sound fields, transducers and vibration*. Academic Press (2019).

105. Long M. 2 - Fundamentals of Acoustics. In: *Architectural Acoustics (Second Edition)* (ed Long M). Academic Press (2014).

106. Zhang G. *Bulk and surface acoustic waves: fundamentals, devices, and applications*. Jenny Stanford Publishing (2022).

107. Rayleigh L. On waves propagated along the plane surface of an elastic solid. *Proceedings of the London mathematical Society* **1**, 4-11 (1885).

108. Luo J*, et al.* Shear-horizontal surface acoustic wave characteristics of a (110) ZnO/SiO2/Si multilayer structure. *Journal of Alloys and Compounds* **693**, 558-564 (2017).

109. Fu YQ*, et al.* Advances in piezoelectric thin films for acoustic biosensors, acoustofluidics and lab-on-chip applications. *Progress in Materials Science* **89**, 31-91 (2017).

110. Josse F*, et al.* Guided shear horizontal surface acoustic wave sensors for chemical and biochemical detection in liquids. *Analytical Chemistry* **73**, 5937-5944 (2001).

111. Fu Y-Q*, et al.* Engineering inclined orientations of piezoelectric films for integrated acoustofluidics and lab-on-a-chip operated in liquid environments. *Lab on a Chip* **21**, 254-271 (2021).

112. Worden K. Rayleigh and Lamb Waves-Basic Principles. *Strain* **37**, 167-172 (2001).

113. Katzir S. The discovery of the piezoelectric effect. In: *The beginnings of piezoelectricity: a study in mundane physics*). Springer (2006).

114. Yang J*, et al. An introduction to the theory of piezoelectricity*. Springer (2005).

115. Bairagi S*, et al.* Mechanical energy harvesting and self-powered electronic applications of textile-based piezoelectric nanogenerators: A systematic review. *Nano Energy* **111**, 108414 (2023).

116. Friend J*, et al.* Microscale acoustofluidics: Microfluidics driven via acoustics and ultrasonics. *Reviews of Modern Physics* **83**, 647-704 (2011).

117. Bruus H. Acoustofluidics 1: Governing equations in microfluidics. *Lab on a Chip* **11**, 3742-3751 (2011).

118. Bruus H. Acoustofluidics 2: Perturbation theory and ultrasound resonance modes. *Lab on a Chip* **12**, 20-28 (2012).

119. Muller PB*, et al.* A numerical study of microparticle acoustophoresis driven by acoustic radiation forces and streaming-induced drag forces. *Lab on a Chip* **12**, 4617-4627 (2012).

120. Fan Y*, et al.* Recent advances in acoustofluidic separation technology in biology. *Microsystems & Nanoengineering* **8**, 94 (2022).

121. Silva GT*, et al.* Acoustic interaction forces between small particles in an ideal fluid. *Phys Rev E Stat Nonlin Soft Matter Phys* **90**, 063007 (2014).

122. King LV. On the acoustic radiation pressure on spheres. *Proceedings of the Royal Society of London Series A-Mathematical and Physical Sciences* **147**, 212-240 (1934).

123. Yosioka K*, et al.* Acoustic radiation pressure on a compressible sphere. *Acta Acustica united with Acustica* **5**, 167-173 (1955).

124. Lighthill J. Acoustic streaming. *Journal of sound and vibration* **61**, 391-418 (1978).

125. Riley N. Steady streaming. *Annual Review of Fluid Mechanics* **33**, 43-65 (2001).

126. Stokes GG. On the effect of the internal friction of fluids on the motion of pendulums. (1851).

127. Glynne-Jones P*, et al.* Acoustofluidics 23: acoustic manipulation combined with other force fields. *Lab on a Chip* **13**, 1003-1010 (2013).

128. Wiklund M*, et al.* Acoustofluidics 14: Applications of acoustic streaming in microfluidic devices. *Lab on a Chip* **12**, 2438-2451 (2012).

129. Sadhal S. Acoustofluidics 13: Analysis of acoustic streaming by perturbation methods. *Lab on a Chip* **12**, 2292-2300 (2012).

130. Wu J. Acoustic streaming and its applications. *Fluids* **3**, 108 (2018).

131. Wang H*, et al.* Modelling hybrid acoustofluidic devices for enhancing Nano- and Micro-Particle manipulation in microfluidics. *Applied Acoustics* **205**, 109258 (2023).

132. Moiseyenko RP*, et al.* Whole-system ultrasound resonances as the basis for acoustophoresis in all-polymer microfluidic devices. *Physical Review Applied* **11**, 014014 (2019).

133. Wu M*, et al.* Circulating Tumor Cell Phenotyping via High-Throughput Acoustic Separation. *Small* **14**, 1801131 (2018).

134. Li Y*, et al.* Dependence of acoustophoretic aggregation on the impedance of microchannel's walls. *Computer Methods and Programs in Biomedicine* **260**, 108530 (2025).

135. Kolesnik K*, et al.* Optimizing coupling layer and superstrate thickness in attachable acoustofluidic devices. *Ultrasonics* **137**, 107202 (2024).

136. Xu G*, et al.* Acoustic characterization of polydimethylsiloxane for microscale acoustofluidics. *Physical Review Applied* **13**, 054069 (2020).

137. Yin Q*, et al.* Acoustically Activated Nozzle for Microdroplet Generation and Dispensing. *Physical Review Applied* **20**, 024067 (2023).

138. He Z*, et al.* A portable droplet generation system for ultra-wide dynamic range digital PCR based on a vibrating sharp-tip capillary. *Biosensors and Bioelectronics* **191**, 113458 (2021).

139. Tsuyama Y*, et al.* A 50 μm acoustic resonator microchannel enables focusing 100 nm polystyrene beads and sub-micron bioparticles. *Sensors and Actuators B: Chemical* **376**, 132918 (2023).

140. Zhang W*, et al.* Versatile acoustic manipulation of micro-objects using mode-switchable oscillating bubbles: transportation, trapping, rotation, and revolution. *Lab on a Chip* **21**, 4760-4771 (2021).

141. Melde K*, et al.* Holograms for acoustics. *Nature* **537**, 518-522 (2016).

142. Melde K*, et al.* Compact holographic sound fields enable rapid one-step assembly of matter in 3D. *Science Advances* **9**, eadf6182 (2023).

143. Marzo A*, et al.* Holographic acoustic tweezers. *Proc Natl Acad Sci U S A* **116**, 84-89 (2019).

144. Marzo A*, et al.* Holographic acoustic elements for manipulation of levitated objects. *Nature Communications* **6**, 8661 (2015).

145. Wixforth A*, et al.* Acoustic manipulation of small droplets. *Analytical and Bioanalytical Chemistry* **379**, 982-991 (2004).

146. Ding X*, et al.* Surface acoustic wave microfluidics. *Lab on a Chip* **13**, 3626-3649 (2013).

147. Nawaz AA*, et al.* Image-based cell sorting using focused travelling surface acoustic waves. *Lab on a Chip* **23**, 372-387 (2023).

148. Li P*, et al.* Sheathless Acoustic Fluorescence Activated Cell Sorting (aFACS) with High Cell Viability. *Anal Chem* **91**, 15425-15435 (2019).

149. Marqus S*, et al.* High frequency acoustic nebulization for pulmonary delivery of antibiotic alternatives against Staphylococcus aureus. *European Journal of Pharmaceutics and Biopharmaceutics* **151**, 181-188 (2020).

150. Rezk AR*, et al.* HYbriD Resonant Acoustics (HYDRA). *Adv Mater* **28**, 1970-1975 (2016).

151. Zhang N*, et al.* Manipulation and Mixing of 200 Femtoliter Droplets in Nanofluidic Channels Using MHz-Order Surface Acoustic Waves. *Adv Sci (Weinh)* **8**, 2100408 (2021).

152. Wang Y*, et al.* Flexible/bendable acoustofluidics based on thin-film surface acoustic waves on thin aluminum sheets. *Acs Applied Materials & Interfaces* **13**, 16978-16986 (2021).

153. Tian Z*, et al.* Generating multifunctional acoustic tweezers in Petri dishes for contactless, precise manipulation of bioparticles. *Science Advances* **6**, eabb0494 (2020).

154. Baudoin M*, et al.* Folding a focalized acoustical vortex on a flat holographic transducer: Miniaturized selective acoustical tweezers. *Science Advances* **5**, eaav1967 (2019).

155. Baudoin M*, et al.* Spatially selective manipulation of cells with single-beam acoustical tweezers. *Nature Communications* **11**, 4244 (2020).

156. Tian Z*, et al.* Wave number–spiral acoustic tweezers for dynamic and reconfigurable manipulation of particles and cells. *Science Advances* **5**, eaau6062 (2019).

157. Collins DJ*, et al.* Highly focused high-frequency travelling surface acoustic waves (SAW) for rapid single-particle sorting. *Lab Chip* **16**, 471-479 (2016).

158. Middelkoop TC*, et al.* CYK-1/Formin activation in cortical RhoA signaling centers promotes organismal left–right symmetry breaking. *Proceedings of the National Academy of Sciences* **118**, e2021814118 (2021).

159. Ascione F*, et al.* Collective rotational motion of freely expanding T84 epithelial cell colonies. *Journal of the Royal Society Interface* **20**, 20220719 (2023).

160. Wang H*, et al.* Rotational motion during three-dimensional morphogenesis of mammary epithelial acini relates to laminin matrix assembly. *Proceedings of the National Academy of Sciences* **110**, 163-168 (2013).

161. Tan AP*, et al.* Continuous-flow cytomorphological staining and analysis. *Lab on a Chip* **14**, 522-531 (2014).

162. Gai J*, et al.* High-Frequency Ultrasound Boosts Bull and Human Sperm Motility. *Adv Sci (Weinh)* **9**, e2104362 (2022).

163. Devendran C*, et al.* The importance of travelling wave components in standing surface acoustic wave (SSAW) systems. *Lab on a Chip* **16**, 3756-3766 (2016).

164. Koss LG*, et al. Koss' diagnostic cytology and its histopathologic bases*. Lippincott Williams & Wilkins (2006).

165. Baldwin P*, et al.* Translational approaches to improving cervical screening. *Nature Reviews Cancer* **3**, 217-226 (2003).

166. Nguyen GK. *Essentials of fluid cytology*. Library and Archives Canada (2010).

167. Traynor D*, et al.* Raman spectral cytopathology for cancer diagnostic applications. *Nature Protocols* **16**, 3716-3735 (2021).

168. Kitchener HC*, et al.* HPV testing in routine cervical screening: cross sectional data from the ARTISTIC trial. *British Journal of Cancer* **95**, 56-61 (2006).

169. Machalek DA*, et al.* Routine cervical screening by primary HPV testing: early findings in the renewed National Cervical Screening Program. *Medical Journal of Australia* **211**, 113-119 (2019).

170. Mikhaylov R*, et al.* Development and characterisation of acoustofluidic devices using detachable electrodes made from PCB. *Lab on a Chip* **20**, 1807-1814 (2020).

171. Sun C*, et al.* Flexible Printed Circuit Board as Novel Electrodes for Acoustofluidic Devices. *IEEE Transactions on Electron Devices* **68**, 393-398 (2021).

172. Mikhaylov R*, et al.* A reconfigurable and portable acoustofluidic system based on flexible printed circuit board for the manipulation of microspheres. *Journal of Micromechanics and Microengineering* **31**, 074003 (2021).

173. Volk A*, et al.* Growth control of sessile microbubbles in PDMS devices. *Lab on a Chip* **15**, 4607-4613 (2015).

174. Hatton IA*, et al.* The human cell count and size distribution. *Proceedings of the National Academy of Sciences* **120**, e2303077120 (2023).

175. Jiang X*, et al.* Mapping hepatocyte size in vivo using temporal diffusion spectroscopy MRI. *Magnetic Resonance in Medicine* **84**, 2671-2683 (2020).

176. Waugh RE*, et al.* Rheologic Properties of Senescent Erythrocytes: Loss of Surface Area and Volume With Red Blood Cell Age. *Blood* **79**, 1351-1358 (1992).

177. Tong C*, et al.* Spatial and temporal modulation of cell instructive cues in a filamentous supramolecular biomaterial. *Acs Applied Materials & Interfaces* **14**, 17042-17054 (2022).

178. Hanna MG*, et al.* Comparison of glass slides and various digital-slide modalities for cytopathology screening and interpretation. *Cancer Cytopathology* **125**, 701-709 (2017).

179. Mach AJ*, et al.* Microfluidic sample preparation for diagnostic cytopathology. *Lab on a Chip* **13**, 1011-1026 (2013).

180. Vaickus LJ*, et al.* Young investigator challenge: the accuracy of the nuclear-to-cytoplasmic ratio estimation among trained morphologists. *Cancer Cytopathology* **123**, 524-530 (2015).

181. Berg KCG*, et al.* Multi-omics of 34 colorectal cancer cell lines - a resource for biomedical studies. *Molecular Cancer* **16**, 116 (2017).

182. Barascu A*, et al.* Oxidative stress induces an ATM-independent senescence pathway through p38 MAPK-mediated lamin B1 accumulation. *The EMBO Journal* **31**, 1080-1094 (2012).

183. Maitra D*, et al.* Ambient light promotes selective subcellular proteotoxicity after endogenous and exogenous porphyrinogenic stress. *Journal of Biological Chemistry* **290**, 23711-23724 (2015).

184. Zhang Y*, et al.* Nuclear Nestin deficiency drives tumor senescence via lamin A/C-dependent nuclear deformation. *Nature Communications* **9**, 3613 (2018).

185. Meng S*, et al.* Circulating Tumor Cells in Patients with Breast Cancer Dormancy. *Clinical Cancer Research* **10**, 8152-8162 (2004).

186. Hao SJ*, et al.* Size-based separation methods of circulating tumor cells. *Advanced Drug Delivery Reviews* **125**, 3-20 (2018).

187. Su Lim C*, et al.* Measurement of the Nucleus Area and Nucleus/Cytoplasm and Mitochondria/Nucleus Ratios in Human Colon Tissues by Dual-Colour Two-Photon Microscopy Imaging. *Scientific Reports* **5**, 18521 (2015).

188. Carter M*, et al.* Chapter 13 - Cell Culture Techniques. In: *Guide to Research Techniques in Neuroscience (Third Edition)* (eds Matt Carter, Shieh JC). Academic Press (2022).

189. Heidrich I*, et al.* Liquid biopsies: Potential and challenges. *International Journal of Cancer* **148**, 528-545 (2021).

190. Pantel K*, et al.* Circulating tumour cells in cancer patients: challenges and perspectives. *Trends in Molecular Medicine* **16**, 398-406 (2010).

191. Stringer M*, et al.* Methodologies, technologies, and strategies for acoustic streaming-based acoustofluidics. *Applied Physics Reviews* **10**, 011315 (2023).

192. Schippers I*, et al.* Immortalized human hepatocytes as a tool for the study of hepatocytic (de-) differentiation. *Cell Biology and Toxicology* **13**, 375-386 (1997).

193. Janssen AFJ*, et al.* Current Methods and Pipelines for Image-Based Quantitation of Nuclear Shape and Nuclear Envelope Abnormalities. *Cells* **11**, 347 (2022).

194. Schöchlin M*, et al.* A nuclear circularity-based classifier for diagnostic distinction of desmoplastic from spindle cell melanoma in digitized histological images. *Journal of Pathology Informatics* **5**, 40 (2014).

195. Yang X*, et al.* Accurate Extraction of the Self-Rotational Speed for Cells in an Electrokinetics Force Field by an Image Matching Algorithm. *Micromachines* **8**, 282 (2017).

196. Qihua Y*, et al.* Cell Electrorotation Motion Parameters Detection Based on Image Processing. In: *2009 WRI World Congress on Computer Science and Information Engineering*) (2009).

197. Zhao Y*, et al.* Determination of the Three-Dimensional Rate of Cancer Cell Rotation in an Optically-Induced Electrokinetics Chip Using an Optical Flow Algorithm. *Micromachines* **9**, 118 (2018).

198. Li H*, et al.* Image Processing Technique for Characteristic Test of Cell Based on Electrorotation Chip. In: *2008 2nd International Conference on Bioinformatics and Biomedical Engineering*) (2008).

199. Ringnér M. What is principal component analysis? *Nature Biotechnology* **26**, 303-304 (2008).

200. Prausnitz MR*, et al.* Transdermal drug delivery. *Nature Biotechnology* **26**, 1261-1268 (2008).

201. Brown MB*, et al.* Dermal and Transdermal Drug Delivery Systems: Current and Future Prospects. *Drug Delivery* **13**, 175-187 (2006).

202. Prausnitz MR*, et al.* Current status and future potential of transdermal drug delivery. *Nature Reviews Drug Discovery* **3**, 115-124 (2004).

203. Liu Y*, et al.* Lab-on-skin: a review of flexible and stretchable electronics for wearable health monitoring. *ACS Nano* **11**, 9614-9635 (2017).

204. Scheuplein RJ*, et al.* Permeability of the skin. *Physiological reviews* **51**, 702-747 (1971).

205. Bouwstra J*, et al.* Thermodynamic and structural aspects of the skin barrier. *Journal of Controlled Release* **15**, 209-219 (1991).

206. Karande P*, et al.* Design principles of chemical penetration enhancers for transdermal drug delivery. *Proceedings of the National Academy of Sciences* **102**, 4688-4693 (2005).

207. Kalia YN*, et al.* Iontophoretic drug delivery. *Advanced Drug Delivery Reviews* **56**, 619-658 (2004).

208. Wanasathop A*, et al.* Iontophoretic drug delivery in the oral cavity. *Pharmaceutics* **10**, 121 (2018).

209. Szunerits S*, et al.* Heat: a highly efficient skin enhancer for transdermal drug delivery. *Frontiers in Bioengineering and Biotechnology* **6**, 15 (2018).

210. Prausnitz MR. Microneedles for transdermal drug delivery. *Advanced Drug Delivery Reviews* **56**, 581-587 (2004).

211. Chang H*, et al.* Cryomicroneedles for transdermal cell delivery. *Nature Biomedical Engineering* **5**, 1008-1018 (2021).

212. Yu J*, et al.* Glucose-responsive insulin patch for the regulation of blood glucose in mice and minipigs. *Nature Biomedical Engineering* **4**, 499-506 (2020).

213. Denet A-R*, et al.* Skin electroporation for transdermal and topical delivery. *Advanced Drug Delivery Reviews* **56**, 659-674 (2004).

214. Ita K. Perspectives on transdermal electroporation. *Pharmaceutics* **8**, 9 (2016).

215. Seah BC-Q*, et al.* Recent advances in ultrasound-based transdermal drug delivery. *International journal of nanomedicine*, 7749-7763 (2018).

216. Zhang J*, et al.* Wearable transdermal drug delivery system controlled by wirelessly powered acoustic waves. *Journal of Controlled Release* **381**, 113619 (2025).

217. Zhang J*, et al.* Flexible surface acoustic wave technology for enhancing transdermal drug delivery. *Drug Delivery and Translational Research* **15**, 1363-1375 (2025).

218. Ma Z*, et al.* Controlled tough bioadhesion mediated by ultrasound. *Science* **377**, 751-755 (2022).

219. Ramesan S*, et al.* High frequency acoustic permeabilisation of drugs through tissue for localised mucosal delivery. *Lab on a Chip* **18**, 3272-3284 (2018).

220. Polat BE*, et al.* Ultrasound-mediated transdermal drug delivery: Mechanisms, scope, and emerging trends. *Journal of Controlled Release* **152**, 330-348 (2011).

221. France MM*, et al.* Ultra-rapid drug delivery in the oral cavity using ultrasound. *Journal of Controlled Release* **304**, 1-6 (2019).

222. Zhang X*, et al.* Microbubble-Enhanced Transdermal Drug Delivery Sonoelectric Patch. *Acs Applied Materials & Interfaces*, (2024).

223. Liao A-H*, et al.* Ultrasound-induced microbubble cavitation via a transcanal or transcranial approach facilitates inner ear drug delivery. *Jci Insight* **5**, (2020).

224. Wu Q*, et al.* On-demand transdermal drug delivery platform based on wearable acoustic microneedle array. *Chemical Engineering Journal* **477**, 147124 (2023).

225. Chen Z*, et al.* 3D-Printed Integrated Ultrasonic Microneedle Array for Rapid Transdermal Drug Delivery. *Molecular Pharmaceutics* **19**, 3314-3322 (2022).

226. Khunti K*, et al.* Rates and predictors of hypoglycaemia in 27 585 people from 24 countries with insulin-treated type 1 and type 2 diabetes: the global HAT study. *Diabetes, obesity and metabolism* **18**, 907-915 (2016).

227. Botan V*, et al.* The effects of a leaflet-based intervention,'Hypos can strike twice', on recurrent hypoglycaemic attendances by ambulance services: A non-randomised stepped wedge study. *Diabetic Medicine* **38**, e14612 (2021).

228. Parekh W*, et al.* Approach to assessing the economic impact of insulin-related hypoglycaemia using the novel Local Impact of Hypoglycaemia Tool. *Diabetic Medicine* **32**, 1156-1166 (2015).

229. Zoungas S*, et al.* Severe hypoglycemia and risks of vascular events and death. *New England Journal of Medicine* **363**, 1410-1418 (2010).

230. Heinemann L*, et al.* Real-time continuous glucose monitoring in adults with type 1 diabetes and impaired hypoglycaemia awareness or severe hypoglycaemia treated with multiple daily insulin injections (HypoDE): a multicentre, randomised controlled trial. *The Lancet* **391**, 1367-1377 (2018).

231. Mathew P*, et al.* Hypoglycemia. (2018).

232. Sherman JJ*, et al.* Glucagon therapy: a comparison of current and novel treatments. *Diabetes Spectrum* **33**, 347-351 (2020).

233. Diabetes N*, et al.* The hospital management of hypoglycaemia in adults with diabetes mellitus. *Available at www diabetologists-abcd org uk/JBDS/JBDS_IP_Hypo_Adults pdf (accessed March 2015)*, (2010).

234. Chen J*, et al.* Microneedle-mediated drug delivery for cutaneous diseases. *Frontiers in Bioengineering and Biotechnology* **10**, 1032041 (2022).

235. Shakya G*, et al.* Ultrasound-responsive microbubbles and nanodroplets: A pathway to targeted drug delivery. *Advanced Drug Delivery Reviews* **206**, 115178 (2024).

236. Cattaneo M*, et al.* Cyclic jetting enables microbubble-mediated drug delivery. *Nature Physics*, (2025).

237. Perçin G*, et al.* Piezoelectric droplet ejector for ink-jet printing of fluids and solid particles. *Review of Scientific Instruments* **74**, 1120-1127 (2003).

238. Phatale V*, et al.* Overcoming skin barriers through advanced transdermal drug delivery approaches. *Journal of Controlled Release* **351**, 361-380 (2022).

239. Roberts MS*, et al.* Topical drug delivery: History, percutaneous absorption, and product development. *Advanced Drug Delivery Reviews* **177**, 113929 (2021).

240. Chaturvedi S*, et al.* An insight of techniques for the assessment of permeation flux across the skin for optimization of topical and transdermal drug delivery systems. *Journal of Drug Delivery Science and Technology* **62**, 102355 (2021).

241. Kathe K*, et al.* Film forming systems for topical and transdermal drug delivery. *Asian journal of pharmaceutical sciences* **12**, 487-497 (2017).

242. Volpatti LR*, et al.* Glucose-Responsive Nanoparticles for Rapid and Extended Self-Regulated Insulin Delivery. *ACS Nano* **14**, 488-497 (2020).

243. Stanley S*, et al.* Central Mechanisms of Glucose Sensing and Counterregulation in Defense of Hypoglycemia. *Endocrine Reviews* **40**, 768-788 (2019).

244. Wu Z*, et al.* Investigation of piezoelectric printing devices for oil-free and on-demand picolitre monodisperse droplet generation. *Scientific Reports* **14**, 17104 (2024).

245. Thielicke W*, et al.* Particle Image Velocimetry for MATLAB: Accuracy and enhanced algorithms in PIVlab. (2021).

246. Adrian RJ. Particle-imaging techniques for experimental fluid mechanics. *Annual Review of Fluid Mechanics* **23**, 261-304 (1991).

247. Mitruka BM*, et al. Clinical biochemical and hematological reference values in normal experimental animals* (1977).

248. Harkness JE*, et al. Harkness and Wagner's biology and medicine of rabbits and rodents*. John Wiley & Sons (2013).